UCID-20622-92-1

Chemistry & Materials Science Progress Report

Weapons-Supporting Research and Laboratory Directed Research & Development

First Half, FY 1992

July 1992

Lawrence Livermore National Laboratory

Contents

UCID--20622-92-1

DE92 019905

Weapons-Supporting Research

Foreword

The research reported here in summary form was conducted during the first half of FY 92 under the auspices of Weapons-Supporting Research (WSR) and Laboratory Directed Research and Development (LDRD).

WSR is the principal source of discretionary funds to support fundamental research in the Chemistry & Materials Science (C&MS) Department. WSR provides the scientific and technological base required in the longer term for the success of the Weapons Program.

Administratively, work funded by WSR is organized into three categories: (a) block-funded programs ("thrust areas"), each of which typically involves several senior scientists in a coordinated, focused approach to a scientific or technological problem, (b) research groups consisting of two or three scientists, and (c) a few smaller projects led by individual investigators.

LDRD-funded work broadens the exploratory research base of C&MS and consists of several categories of discretionary research activities. Of these, Exploratory Research and Development (ERD)—formerly Departmental IR&D—and Innovative Program Supporting Research (SR) are included in this report. In FY 92, ERD funds have underwritten several single-investigator projects and relatively large programs.

The results reported here are for work in progress; as such, they may be preliminary, fragmentary, or incomplete. Interested readers should consult one of the authors of a report before quoting it or otherwise referring to it.

Readers may notice a minor change in the title of this volume. Heretofore, the fact that this was a *Progress Report* was not evident in the title, although we always referred to it as such in conversation. The new title corrects that problem, but we are continuing the numbering system used under the old *Research Report* so that a report for a particular fiscal year can easily be found.

T. T. Sugihara

Weapons-Supporting Research

Thrust Areas

Fundamentals of the Physics and Processing of Metals

W. H. Gourdin, ***Thrust Area Leader***

Overview

The V-Ga project is focused on producing grain sizes large enough (>0.2 μm) to permit unique chemical and diffraction analysis. Efforts are under way to achieve this goal with a high-temperature (1000°C) substrate table. Nevertheless, observation of diffraction rings unique to the predicted X-phase (A_5B_3) have been observed and simulated for fine-grained (<0.1-μm) specimens. On the Ni_3Al project, the results of initial experiments and the efforts of Patricia Johnson, who joined the effort in February, have led to a focus on the effects of relative grain-boundary orientation on the cohesive strength and the extent and effects of boron segregation. If successful, measurements of relative boundary strength will be important in clarifying the role boron plays in ductilizing $L1_2$ intermetallics. Also as a part of this effort, Nick Kioussis has laid necessary theoretical groundwork with his calculations of the electronic structure of "undoped" Ni_3Al and is moving quickly on to calculations of substitutional and interstitial boron. Gonis and Singh have demonstrated the applicability of their charge-transfer code to alloys of Al-Li, showing that the modifications are critical to a realistic description of this unusual material. This capability to properly handle charge transfer is unique. Sluiter's initial work suggests that certain periodicities and growth habits of artificial superlattices are metastable in the Ti-V system. In the concluding stage of his project, Elmer has found ultrafine particles in a Cu-5%Nb alloy, suggesting a wider applicability of his liquid-phase nucleation (LPN) theory.

Correlation of Electronic Structure with Processing of Advanced Substitutional Alloys

Principal Investigator: A. F. Jankowski
Co-investigator: P. E. A. Turchi

Overview

Our objective in this study is to examine the origin of alloy phase stability with emphasis on the occurrence of structural transformations in substitutional systems that exhibit complex crystalline structures. To accomplish this and to validate our current understanding, we seek to compare the results of state-of-the-art calculations with well-focused experiments on the Ti-Pd and Ga-V systems.

Experiment (A. F. Jankowski)

The synthesis and characterization of Ga-V alloys are in progress to experimentally verify the existence of an (V_3Ga) A15 structural variant: a predicted (V_5Ga_3) X-phase.[1] Films, several micrometers thick were deposited onto room temperature mica substrates from arc-melted buttons of $Ga_{0.30}V_{0.70}$, $Ga_{0.20}V_{0.80}$, and $Ga_{0.35}V_{0.65}$ that were hot-pressed into sputter targets. Emphasis was placed on studying the $Ga_{0.30}V_{0.70}$ films. X-ray diffraction analysis of the $Ga_{0.30}V_{0.70}$ superconducting target was indexed to the V_3Ga phase with a minor V_6Ga_5 impurity. The $Ga_{0.30}V_{0.70}$ films can be indexed to the A15 phase with possible minor contributions from V_6Ga_5 and vanadium. STEM characterization of the $Ga_{0.30}V_{0.70}$ films revealed a bimodal composition. The nominal 22 at.% and 30 at.% Ga compositions correspond well to the two-phase superconducting transition found using resistance measurements at 12 and 7 K. Films from the other targets show signs of phase segregation outside the A15 phase field. The $Ga_{0.30}V_{0.70}$ films were annealed under high vacuum (10^{-7} Torr) at 610°C for 60 h and then for an additional 385 h in order to increase the submicron grain size of the deposits for single-grain electron diffraction analysis along unique zone axes. Oddly, little success resulted in producing a uniform grain structure larger than 0.1 μm, although diffusion calculations indicated grain sizes larger than 0.5 μm should have resulted. The anneal treatments produced only the confirmed presence of the A15, V_6Ga_5, and V_2Ga_5 phases. Large grains of the Ga-rich V_2Ga_5 phase (from the 60-h anneal) did enable single-grain diffraction patterns to be obtained. The electron diffraction patterns showed the tightly spaced rings characteristic of the fine-grained intermetallics, and a faint ring has been observed at the 0.48-nm lattice spacing predicted for (001) reflections from the X-phase (Fig. 1). X-ray diffraction scans also contain this peak, but unfortunately it also corresponds to the reflection from the mica substrate. Additional samples were deposited at 350°C, the current limit of the substrate platen heater, to enhance grain growth. No noticeable difference from the room-temperature substrate deposits is found, either with x rays or TEM. A high-temperature heater has been ordered to enable $Ga_{0.30}V_{0.70}$ deposits at 700–800°C onto NaCl, MgO and/or $SrTiO_3$ substrates. In addition, the bulk sputter target material will be examined with TEM.

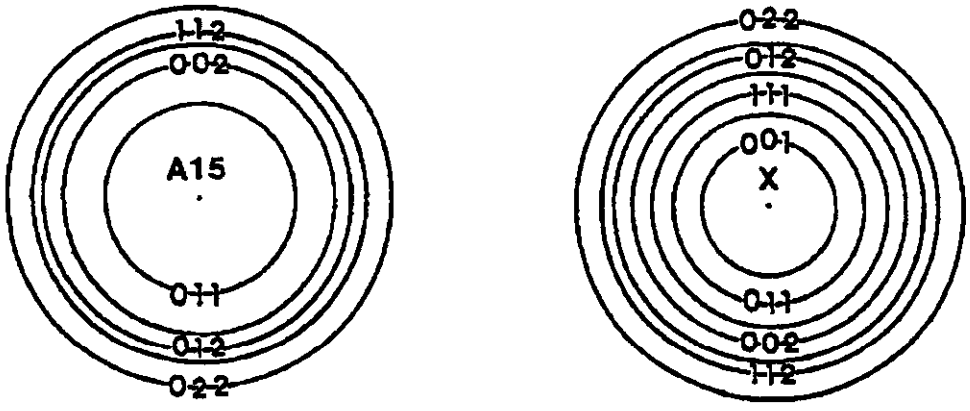

Figure 1. Tightly spaced rings characteristic of the fine-grained intermetallics.

The Ni-Ti binary system contains many complex crystal structures. A previously unreported face-centered-cubic (fcc) phase of titanium has been discovered in Ni/Ti multilayer structures.[2] The fcc Ti phase is formed without stabilization by significant concentrations (i.e., 30-70 at.%) of H, O, or N gas impurities. Additional Ni/Ti samples were prepared with layer pair spacings ranging from 3 to 30 nm in order to examine the dimensional stability of this fcc Ti phase using x-ray diffraction and high-resolution electron microscopy (HREM). Fast Fourier transforms (FFTs) of the high-resolution micrographs confirmed the fcc symmetry in the Ti layers. Overgrowth fcc Ti layers as thick as 1 μm thick have been grown on Ni single crystals. Electron structure calculations are anticipated to compare the energetics of the fcc phase to the well-established α-Ti (hcp) and β-Ti (bcc) phases.

Theory (P. E. A. Turchi)

On the theory side, additional first-principles electronic structure calculations based on Multiple Scattering Theory and the Local Density Approximation, (KKR-CPA-GPM) have been performed for bcc-based Ti-Pd alloys as a function of composition. Such calculations were used to predict the local chemical order which characterizes this alloy, particularly in the bcc-solid solution at high temperature above the domain of existence of an A15-based alloy stable at low temperature around 25 at.% Pd.

We report in Table 1 the as-computed effective pair interactions (EPIs) V_S (where s is the shell index pertaining to the bcc lattice) expressed in mRy/atom, which build up the ordering energy of the Ti-Pd alloy at each concentration. Note that the first neighbor EPI V_1 is definitely controlling the ordering tendencies that occur in this alloy and is strongly concentration dependent. With the convention of sign, a positive EPI favors AB pair formation, whereas a negative EPI favors phase separation. With these EPIs, at each stoichiometry, we predict the following ordered states: DO3 (of Fe_3-Al-type) for Ti_3Pd and $TiPd_3$, C11b (of $MoSi_2$-type) for Ti_2Pd and $TiPd_2$, and B2 for TiPd. These ground states constitute the most probable ordered configuration that may be observed in a metastable state, if not in a stable state, provided one can process bcc-based Ti-Pd alloys. Note also that the additional energy of mixing (ΔE_{mix}, expressed in mRy/atom, also reported in Table 1) that characterizes the totally random configuration of the alloy also favors alloy formation ($\Delta E_{mix} < 0$) in the entire range of composition.

By combining the information on the mixing and ordering energies, we obtained the final phase diagram at 0 K, which indicates a barely stable DO3 at Ti_3Pd and $TiPd_3$, a C11b at Ti_2Pd and $TiPd_2$, and a strongly stable Be at TiPd. Finally, it is worth mentioning that, from our calculations, Ti_3Pd_5 should exhibit an ordered configuration similar to the one predicted and observed for Al_3Ni_5. Since this ordered phase may play an important role in the martensitic transformation that takes place around 62 at.% Ni in Ni-Al, our theoretical findings suggest that Ti-Pd around 62 at.% Pd would be an interesting alloy to investigate from a phase-transformation point of view.

Table 1. As-computed effective pair interactions.

C_{Pd}	ΔE_{mix}	V_1	V_2	V_3	V_4	V_5	V_6	V_7
0.25	–12.94	9.36	–3.59	1.94	1.58	0.01	0.69	–0.08
0.33	–14.80	7.10	–3.53	1.36	1.76	–0.67	0.58	–0.03
0.50	–16.21	4.81	–2.42	0.49	1.67	–1.53	0.76	–0.05
0.75	–10.61	10.95	–2.48	–0.23	1.56	–0.85	0.87	0.23

Additional work is required to fully compare the two alloy systems Ti-Pd and V-Ga, which display similar features in their equilibrium phase diagrams. In particular, the possible role played by the ordering tendencies in the high-temperature bcc phase in the structural transformation to an A15-based alloy upon cooling is worth addressing.

References

1. P. E. A. Turchi and A. Finel, "Ordering Phenomena in the A15-Based Alloys," *Phys. Rev. B* (accepted for publication) (UCRL-JC-109390).
2. A. F. Jankowski and M. A. Wall, "The Stabilization of Face-Centered-Cubic Titanium," in *Structure and Properties of Interfaces in Materials, MRS Symp. Proc.* **238**, W.A.T. Clark, U. Dahmen, and C. L. Briant, Eds. (Materials Research Society, Pittsburgh, PA, 1992), pp. 297–302.

Presentations

A. F. Jankowski and M. A. Wall, "The stabilization of face-centered-cubic titanium," presented at the MRS Fall Meeting, Boston, MA, December 2–6, 1991.

Publications

A. F. Jankowski and M. A. Wall, "The Stabilization of Face-Centered-Cubic Titanium," in *Structure and Properties of Interfaces in Materials, MRS Symp. Proc.* **238**, W.A.T. Clark, U. Dahmen, and C. L. Briant, Eds. (Materials Research Society, Pittsburgh, PA, 1992), pp. 297–302.

A. F. Jankowski, "A15 Structure Formation in Ti-Pd," *J. Alloys Compounds* **182**, 35 (1992).

Solute Segregation Behavior in Ni_3Al-Based Ordered Alloys

Principal Investigators: W. H. Gourdin and P. E. Johnson
Co-investigators: N. Kioussis* and A. Gonis

Objective

The objective of this project is to provide a fundamental understanding of the effects of ternary solutes on intergranular cohesion and ductility in $L1_2$ ordered intermetallic alloys.

Discussion

In the first months of the year, we concentrated on trying to observe and measure the extent of boron segregation to grain boundaries in Ni_3Al. Specimens were heat-treated to maximize boron segregation, and these proved to be so ductile that they could not be broken in the Auger spectrometer even at 77 K. We constructed a small fracturing device that allowed us to fracture hydrogen-charged specimens at slow rates in an argon glove box, but specimens that were brittle immediately after charging did not fail intergranularly as we expected when fractured later. We attribute this to the loss of hydrogen during transfer from the charging solution to the box, even though copper coatings were applied to minimize this. Limited Auger measurements of mixed-mode fracture surfaces nevertheless indicated boron segregation near ductile failures, but these appeared to change with time, making confirmation difficult. This observation also suggests that boron may redistribute during Auger observations, seriously affecting the validity of the measurements. Concurrently, we explored the possibility of using imaging secondary ion mass spectrometry (SIMS). Although SIMS is extremely sensitive to boron, its lateral resolution (0.1 μm) is inadequate to detect boron segregation when the boundaries are viewed edge-on. However, depth resolution is considerably better (0.01 μm) and we intend to explore the possibility of using SIMS to measure the boron content as we sputter through the plane of an embedded boundary.

We believe that the difficulties and uncertainties in measuring the intergranular boron content are caused, at least in part, by the sensitivity of the boron segregation to the local boundary structure. Similarly, the susceptibility of undoped Ni_3Al to intergranular fracture is clearly the result of local disruption of atomic bonding, and we expect that the grain-boundary cohesive strengths will be extremely sensitive to the grain-boundary structure. To address these issues, we have planned a series of experiments to measure directly the distribution of fracture stresses in polycrystalline Ni_3Al as a function of grain-boundary symmetry. We have built a digitally controlled benchtop load frame, which is now being calibrated, to accomplish this. Friction grips, which can accommodate specimen cross sections up to 3 mm^2, allow the mounting of fragile specimens while ensuring proper alignment. The first set of experiments will be done on small bars of $Ni_{76}Al_{24}$ recrystallized to produce very large grains in a "bamboo"

* California State University at Northridge.

configuration so that failures will occur at single boundaries across the entire specimen section. Bicrystals will be used to study a limited number of specific geometries. Specimens are being sent outside for an analysis of the grain-boundary misorientations using electron back-scattered diffraction patterns (EBDP). Experiments with and without doping will highlight the effect of boron on intergranular cohesion as a function of the boundary symmetry.

Theoretical studies using the linear muffin-tin orbital method have begun, and we have completed calculations of the electronic structure, density of states (DOS), and electron distribution in "undoped" Ni_3Al. The DOS we calculated using a tetrahedral mesh of 165 k-points is smaller at the Fermi energy (82 states/Ry-cell) than that measured experimentally (150–175 states/Ry-cell), but is comparable to other calculated values in the literature. We find that charge is transferred from Al to Ni, and contour plots demonstrate that the electron density is relatively high between Al and Ni and between Ni and Ni. Hence bonding between these species is relatively strong, whereas that between aluminum atoms, as indicated by low electron density, is weak. Calculations to explore the changes induced by both substitutional and interstitial boron as well as antisite defects are in progress.

Stability of Artificial Intermetallic Superlattices

Principal Investigator: M. Sluiter
Co-investigators: P. E. A. Turchi and A. F. Jankowski

Objective

The objective of this study is to understand the underlying factors that determine the stability of artificial superlattices by combining first-principles calculations with well-focused experiments on two prototypical systems, Ni-Ti and Pd-Rh.

Discussion

Tight binding codes were written to deal with layered superstructures on fcc and bcc lattices. In particular, fcc ordered structures such as L10 and Z2 and Z3 were implemented. [Z2(3) corresponds to an L10 with doubled (tripled) layer thickness in the 001 direction.] With electronic parameters representative of transition metal alloys, it was shown that the variation of the band energy with respect to layer thickness was well described by an expansion derived with the GPM formalism. Therefore, at least for transition metal alloys, one can describe the chemical ordering effects in artificial superlattices by a simple expression that relies on an enumeration of like and unlike bonds.

One fcc phase-separating alloy system (Pd-Rh) was examined using the KKR-CPA-GPM. The ordering energy was evaluated for a number of superlattice geometries. It was found that the ordering energy was monotonic with respect to the repeat period on all growth planes examined. This means that it is unlikely that chemical order can cause

a metastable configuration. As such, the Pd-Rh system is not the most interesting system for further study.

A more interesting system is Ti-V, also of phase separating nature, but this alloy has been predicted to have a metastable superlattice on the 111 planes with a layer thickness of two atomic planes. Such a feature can give rise to interesting kinetic phenomena. In particular, when a homogeneous alloy is created by annealing at high temperature and followed by a rapid quench, the metastable superlattice is likely to appear as the amount of diffusion required for forming the superlattice is much less than that required for long-range phase separation. This prediction is currently being examined by means of a Monte Carlo simulation.

In Ni-Ti, the first-principles KKR-CPA-GPM description correctly identified the ordering tendencies and the ordered states. Unfortunately, the code has failed to give correct energies of mixing. The origin of this problem is suspected to be in the large difference in the charge densities in the interstitial regions associated with Ni and with Ti. Our computer code averages the two interstitial charges. A preliminary estimation of the error in the total energy introduced by this approximation has been shown to be significant for this particular alloy. (The effect of this approximation has also been found in Al-Li alloys by A. Gonis.) A more detailed analysis is under way.

Currently, we are trying to obtain a description of the repulsive part of the total energy of transition metal alloys. The potentials used as input for accurate molecular dynamics simulations require attractive and repulsive components. The attractive component is furnished by the band energy, whereas the repulsive term comes from a Born-Mayer type of expression. However, the parameters for this expression must be obtained by a fit to the known elastic constants of a particular alloy or metal. Therefore, at present, codes are being developed to evaluate the band energy and the repulsive energy for lattices with reduced symmetry.

Presentations

M. Sluiter and P. E. A. Turchi, "Influence of Chemical Order on The Stability of Metallic Superlattices," 1992 Meeting of the American Physical Society, Indianapolis, IN, March 16–20, 1992.

P.E.A. Turchi and M. Sluiter, "Stability of Metallic Superlattices," Optical Society of America, Jackson Hole, WY, March 2–5, 1992.

Publications

P. E. A. Turchi and M. Sluiter, "Stability of Metallic Superlattices," *Physics of X-Ray Multilayer Structures Technical Digest 1992* (Optical Society of America, Washington, DC, 1992), Vol. 7, pp. 128–131 (UCRL-JC-108838).

M. Sluiter and P. E. A. Turchi, "The Role of Chemical Interactions in the Stability of Artificial Metallic Superlattices," *MRS Symp. Proc.* **238**, W. A. T. Clark, C. L. Briant, U. Dahmen, Eds. (Materials Research Society, Pittsburgh, PA, 1991), pp. 623–628 (UCRL-JC-107696).

First-Principles Study of the Thermodynamic and Mechanical Properties of Al-Li Alloys

Principal Investigators: A. Gonis and P. Singh

Objective

Our objective is to develop an adequate computational treatment of charge transfer in a muffin-tin approximation and apply the resulting code to clarify the underlying reasons for the unusual thermodynamic and mechanical properties of Al-Li alloys.

During the first half of this fiscal year, we implemented our codes for treating effective charge-transfer effects in substitutionally disordered alloys within a single-site mean-field treatment of disorder. The codes were first applied to Cu-Zn alloys in which these effects are not very important and were found to give results essentially identical to those obtained with previous computational technology. Thus, we obtained equilibrium lattice constants and energies of mixing that are in very good agreement with previous results. We then applied the codes to the study of Al-Li alloys in which charge transfer effects are known to be substantial. To illustrate the effect of taking proper account of the charge in disordered alloys, we compare and contrast the equilibrium lattice constant and the energies of mixing for Al-Li alloys based on an fcc lattice across the concentration range obtained within the old and new methods.

Figure 2 shows the variation of the equilibrium lattice constant as a function of concentration in fcc-based Al-Li alloys calculated using the old codes. In contrast to experimental findings, the lattice constant first rises to a value higher than that calculated for fcc-Li before reaching the value for Li. (Note that pure Li has the bcc structure; the fcc structure is studied to facilitate comparison with alloys up to about 40% that can exist in the fcc phase.) For such fcc alloys, experiment indicates that the lattice constant *contracts* before expanding to the value for Li.

These results are to be contrasted with those obtained using the new codes (see Fig. 3). Now, the alloy exhibits a contraction upon small additions of Li to Al, in qualitative agreement with experiment, although the value is somewhat larger than that observed experimentally. This effect is to be expected, as experiments are usually done at finite temperature, whereas our calculations implicitly assume $T = 0$ K.

Figure 4 shows the energy of mixing of fcc- and bcc-based alloys as a function of concentration. A positive energy of mixing (defined as the difference between the total energy of the alloy and the average of the two pure materials) indicates a trend toward phase separation. This is in contrast to the known tendency of dilute alloys to precipitate an ordered $L1_2$ phase at low temperatures. When charge-transfer effects are taken into account, the energy of mixing becomes negative (see Fig. 5), which is consistent with the presence of ordered phases in these alloys.

Using the new codes, we are currently studying the electronic properties of clusters embedded in Al-Li alloys. We seek to determine effective cluster interactions that will allow us to predict the transition temperature of the $L1_2$ phase and possibly allow the construction of a phase diagram for these alloys.

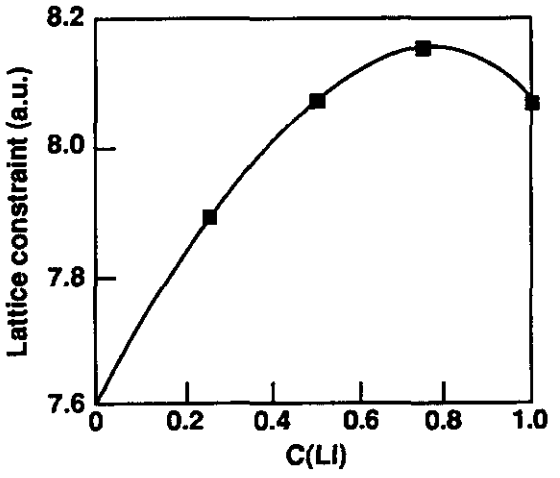

Figure 2

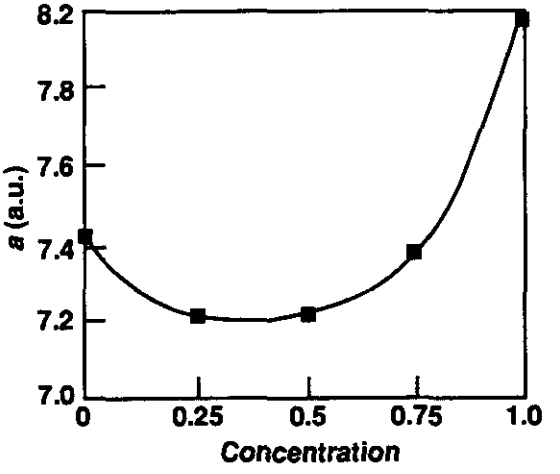

Figure 3

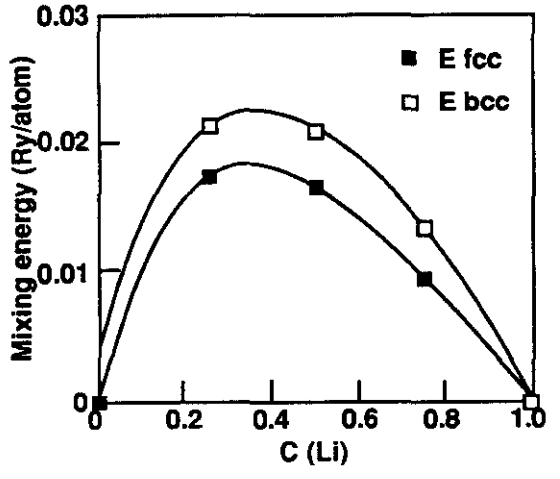

Figure 4

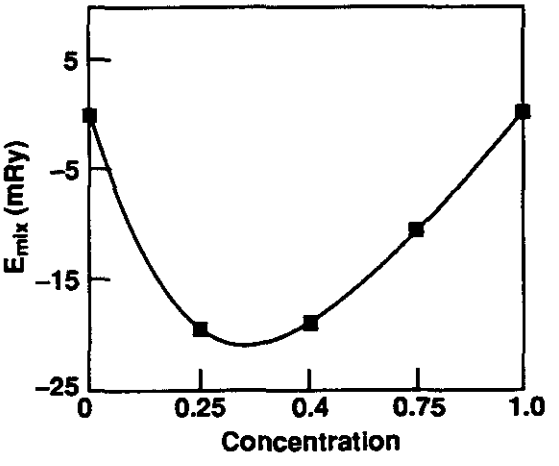

Figure 5

Presentations

A. Gonis, P. P. Singh, P. E. A. Turchi, M. Sluiter, D. D. Johnson, F. J. Pinski, and G. M. Stocks, "KKR-CPA Study of AL-Li Alloys in the Atomic Sphere Approximation (ASA)," 1992 Meeting of the American Physical Society, Indianapolis, IN.

P. P. Singh, A. Gonis, P. E. A. Turchi, and M. Sluiter, "KKR-CPA-GPM Study of Alloy Phase Stability in the Atomic Sphere Approximation," 1992 Meeting of the American Physical Society, Indianapolis, IN.

Rapid-Solidification Research: Microstructural Evolution and Processing Techniques

Principal Investigator: J. W. Elmer
Co-investigators: L. E. Tanner and M. Aziz*

Objective

Our objective in the final phase of this study is to demonstrate that the liquid-phase nucleation (LPN) model developed to explain the formation of arrays of ultrafine particles during rapid solidification of Al-Be alloys also adequately describes rapidly solidified microstructures in other alloy systems with similar thermodynamic characteristics.

Discussion

During the first half of this fiscal year, additional TEM characterization of the Al-Be ultrafine particle microstructure was performed in an attempt to provide additional confirmation of our experimental results. This alloy system is difficult to characterize due to the low volume fraction and small size of the low-scattering Be particles, and it continues to be a characterization challenge. A paper that presents our theory on ultrafine particle formation by LPN was submitted to *Acta Met* in December, 1991.

It proved difficult to make a homogeneous substrate of Ti-Nd, so several other alloys were selected for study. Cu-Nb (5, 10, 15, and 20 at.% Nb), Cu-O (1.7 and 3.4 at.% O), and Fe-17.2 at.% C were acquired from Ames National Laboratory late last year. Arc-splat quenching has been performed on these alloys at U.C. Berkeley as a screening procedure for ultrafine particle formation. Presently, only the Cu-Nb alloys have been examined by TEM, and the results show that *ultrafine particles were produced in the 5 at.% Nb alloy*. The higher Nb-content alloys showed a more conventional liquid spinodal microstructure. Based on the positive results from the Cu-5% Nb alloy, a new series of Cu-Nb alloys is being prepared by AMES at 1.0, 2.5, and 5.0% Nb. These alloys will be investigated using controlled electron beam resolidification to study the rapid solidification conditions required to produce ultrafine particles in these alloys.

Electron beam melts were performed on the Fe-C alloy at travel speeds up to 0.127 m/s. So far, no ultrafine particles have been observed, but additional TEM characterization needs to be performed at higher travel speeds. These results are being hampered by cracking in the melt trail, and other rapid solidification techniques such as arc-splat quenching may be required on the Fe-C alloy in the future. Progress on the Ag-Be alloys has been postponed in order to concentrate our time on the Cu-based alloys.

* Harvard University, Cambridge, MA.

Presentations

J. W. Elmer, "Non-Equilibrium Microstructures Produced During Electron-Beam and Laser-Beam Surface Modification of Metallic Alloys," TMS Metal Science of Joining Symposium, Cincinnati, OH, October, 1991.

Publications

J. W. Elmer, "Non-Equilibrium Microstructures Produced During Electron-Beam and Laser-Beam Surface Modification of Metallic Alloys," in *TMS Metal Science of Joining Symp. Proc.* (The Metallurgical Society, Warrendale, PA, 1991), pp. 123–134.

Interfaces, Adhesion, and Bonding

W. E. King, *Thrust Area Leader*

Overview

Internal interfaces, such as grain boundaries or bimaterial interfaces, play a critical role in the performance of materials systems. In next-generation materials, such as composites and multilayers, the desired properties of the materials originate at the interfaces engineered into the structure. Reliable, predictable performance of materials whose properties are interface-controlled is vital to the technological competitiveness of the United States. To address the issues associated with interface science, the Interface, Adhesion, and Bonding Thrust Area is treating the three key elements of *synthesis and processing, theory simulation and modeling,* and *characterization.* In this report, we describe our recent experimental results on the atomic structure of the (710)/[001] symmetric tilt boundary in niobium, our efforts to quantify high-resolution electron microscopy, and our electronic-structure calculations of metal grain boundaries.

Structure of the Σ5(710)/[001] Symmetric Tilt Grain Boundary in Niobium

G. Campbell, W. King, M. Rühle, W. Wien, and S. Foiles

Introduction

High-resolution transmission electron microscopy (HREM) has been used to evaluate theoretical predictions of the atomic structure of a (710)/[001] symmetric tilt grain boundary in niobium. The boundary was fabricated by diffusion-bonding single crystals in ultrahigh vacuum.[1,2] HREM was performed on the interface along the [001] direction common to both crystals. Models of the grain-boundary structure were predicted using interatomic potentials, which were derived using the embedded-atom method (EAM)[3] and the model-generalized pseudopotential theory (MGPT).[4] The predicted structures have been compared to high-resolution images using image simulation.

Results

The high-resolution images under four different focus conditions of a section of the boundary in Fig. 1 show the strong contrast of the {110} fringes in the bulk crystals. Exactly the same area of the specimen is imaged in each micrograph. This area of the boundary contains three structural repeat units.

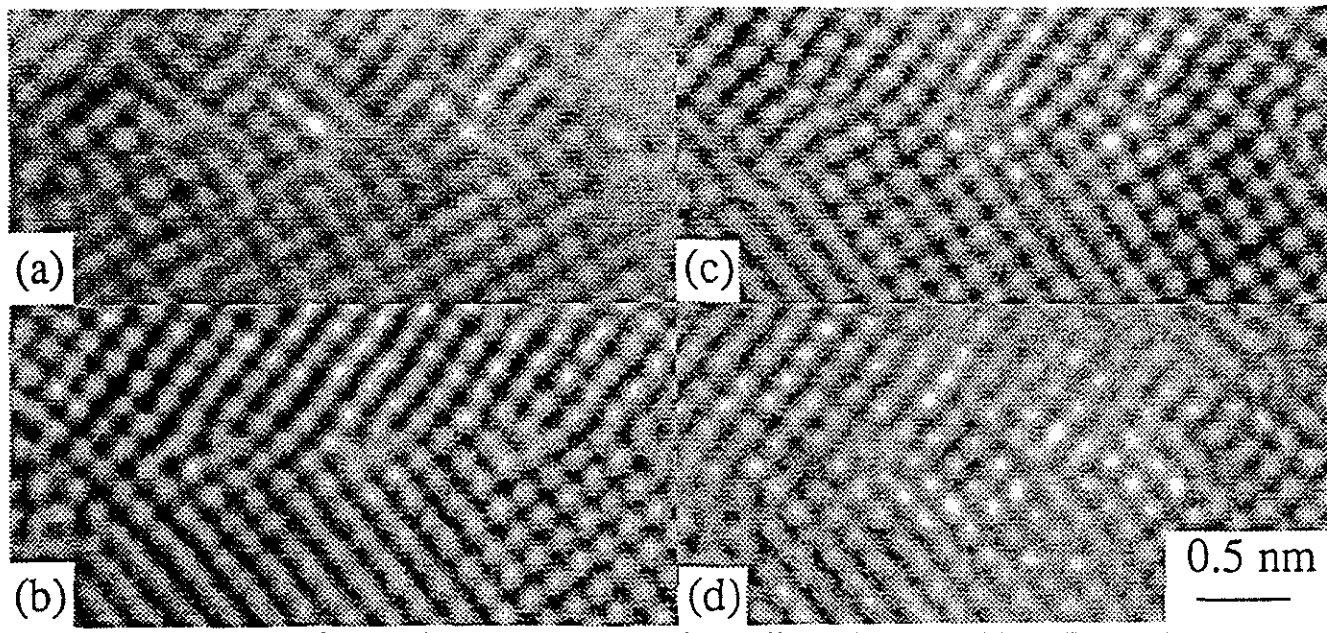

Figure 1. A section of the (710) twin imaged under four different focus conditions. Exactly the same area is shown in each image. This region was very close to the hole, so it is known to be very thin, certainly less than an extinction length (ξ_{110} = 6.2 nm).

The EAM simulations predict 13 stable structures for the (710) twin in niobium. The structures differ primarily in the relative translations of the adjacent crystals. For reference to the microscopy, these translational states could be separated into two components: one along [001], which is parallel to the tilt axis, and one along [$\bar{1}$70], which is perpendicular to the tilt axis but lies in the grain boundary plane. When the model structures are used as input for the image simulations, the magnitude of the latter translational state provides significant differences in the images. Crystal shifts parallel to the electron beam have little or no effect on the image, depending on whether this shift affects the lateral position of atoms in the interface. Nevertheless, of the predicted structures, nine can be discarded because the experimental images show near mirror symmetry about the grain boundary. The four remaining EAM models, designated as s1, s2, s3, and s4, have either a small shift or no shift in [$\bar{1}$70] or have an indiscernible shift in [001] and are listed in Table 1 along with their calculated interfacial energies and the magnitudes of their shifts between the crystals.

Table 1. Interfacial energies and relative translational states of adjacent crystals.

Structure	Interatomic potential	Calculated inter-facial energy (J/m^2)	Translational state of crystals (nm)
s1	EAM	0.96	0.044 in [001]
s2	EAM	0.97	0.02 in [$\bar{1}$70] and 0.035 in [001]
s3	EAM	0.98	0.033 in [001]
s4	EAM	0.98	symmetric
m1	MGPT	1.24	symmetric

When the structures obtained by the EAM calculations were used as the starting configurations for energy minimizations using an interatomic potential derived by the MGPT, all of the starting structures relaxed to the same symmetric structure, also listed in Table 1 as m1. This structure is qualitatively the same as model s4, and these will therefore be considered equivalent models.

The simulated images using the model structures are shown in Fig. 2. Figure 2(a), using model s1, is indistinguishable from Fig. 2(d), using model s4 or m1, because model s1 possesses only a shift of the crystals parallel to the electron beam and leaves the lateral positions of the atoms in the boundary unchanged. Figures 2(b) and 2(c) have slight contrast changes, as pointed out by the arrows, due to the slight shift in $[\bar{1}70]$ for s3 and the fact that the shift in [001] for s2 creates a lateral displacement of atoms in the boundary, which can be imaged as an elongated spot [arrow in Fig. 2(d)].

Discussion

Of the 13 structures predicted by the EAM calculations, 9 can be ruled out on the basis of comparison to the experimental images. The primary factor is the magnitude of the observable shift between the adjacent crystals. The grain boundary appears from the micrographs to be nearly mirror symmetric. The four remaining models differ only by their shifts parallel to the electron beam and in small shifts normal to the beam. It is seen from Fig. 2 that these differences do not lead to large, visible differences in the simulated images. Using standard semiquantitative image-matching methods, it is not possible to choose a best fit between experiment and theory. Quantitative methods of comparison are being developed as part of this research effort and should lead to the ability to discriminate among several grain-boundary models.

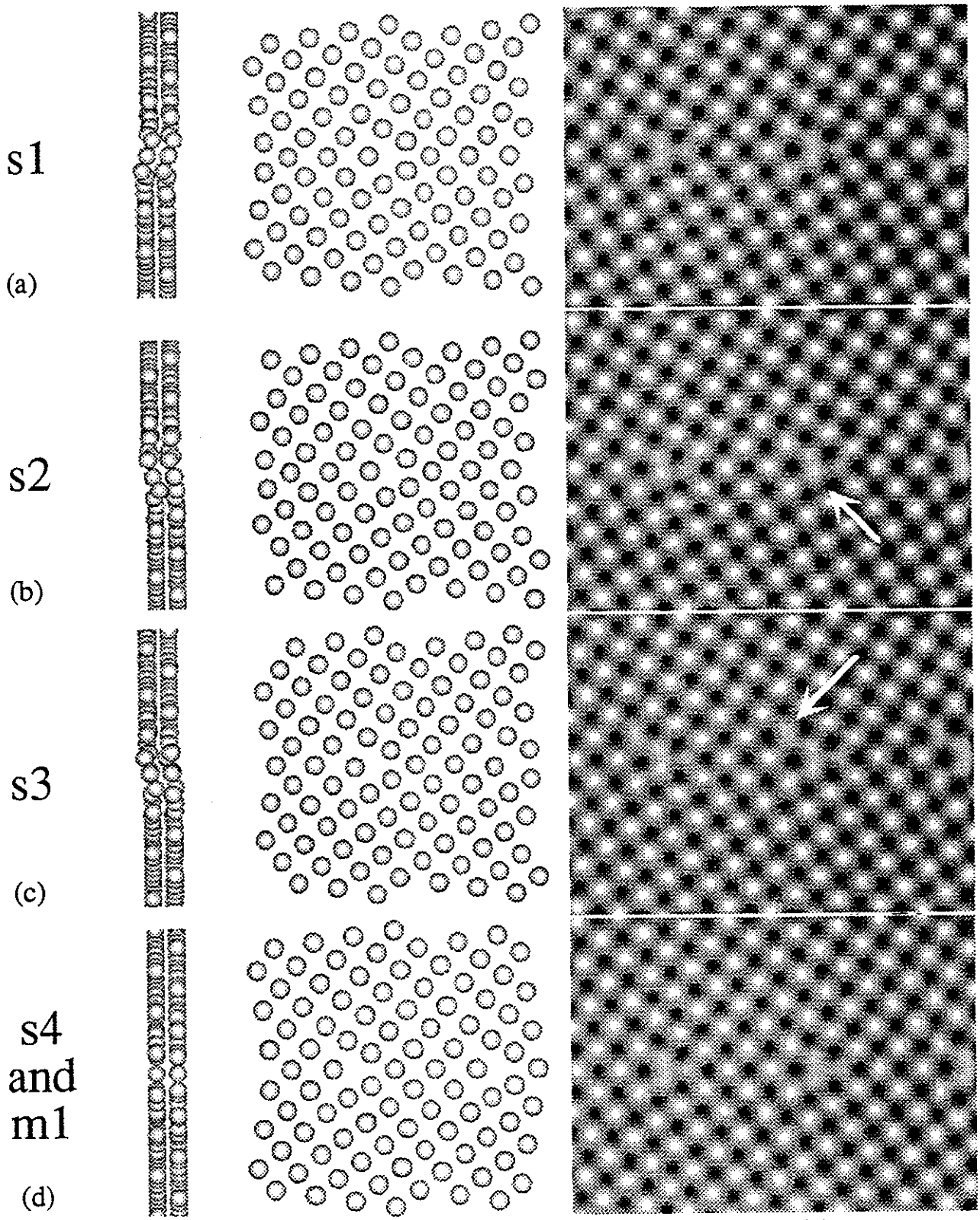

Figure 2. The simulated images using the model structures are shown. The model structures are shown as seen along [170] and [001]. The focus condition in the simulated images is near Scherzer because the contrast is the most sensitive to changes in the model structure. The arrows indicate visible features in the simulated images that arise from differences in the atomic models. Any one of these simulated images matches the experimental images in a qualitative sense.

Determination of Thickness and Defocus by Quantitative Comparison of Experimental and Simulated High-Resolution Images

W. King and G. Campbell

Introduction

In the past, extensive use has been made of high-resolution image-simulation techniques to obtain qualitative and semiquantitative validation of model atomic structures by comparing simulated with experimental images.[5,6,7] In this work, we pursue the quantitative comparison of experimental and simulated images with the intent of deducing the critical imaging parameters of thickness and defocus. Specifically, we present a refinement of the thickness and defocus for a defocus series of high-resolution images using a computational method that is commonly employed in structure refinement by x-ray diffraction and in the analysis of gamma-ray and x-ray spectra, namely unconstrained, nonlinear, least-squares optimization. Defocus results are compared with analysis of the image contrast from amorphous material present in each image. Results indicate that refined values for defocus are consistent with those values determined using more-conventional methods. The refinement method is more sensitive to defocus than is the conventional method. In addition, the refinement method is sensitive to beam/specimen tilt, which can also be extracted from the analysis. Reasonable fits—including thickness, defocus, and beam/specimen tilt—are obtained for defoci near zero defocus, whereas the quality of the fit decreases with increasing defocus.

Figure 1 shows the images used for analysis. A 64- × 64-pixel (0.3303 × 0.3303 nm^2) "average image" and a corresponding "standard-deviation image" were calculated for each defocus value based on approximately 40 unit cells from one side of the interface. Average and standard-deviation images were transformed to electron exposure images. The magnitude of the standard-deviation image is not constant over the entire image. This is due to electron shot noise and fluctuations in the image that are often observed in HREM images. Such fluctuations may be ascribed to phenomena such as surface contamination layers, strain in the structure, inelastic scattering, or thickness variations.

The nonlinear least-squares fitting method was applied to determine the optimum thickness, defocus, and beam/specimen tilt corresponding to each experimental image.[8,9] Images were simulated using the EMS image-simulation code.[10] Input parameters for the image simulation were independently determined when possible to minimize the number of free parameters in the fit.

Figure 3 shows an experimental image (left), the corresponding best-fit simulated image (center), and the normalized residuals (right) for the defocus value, nominally zero. Beneath the images and the normalized residuals are gray scales that denote the range of relative exposure values for each image and the range of the normalized residuals.

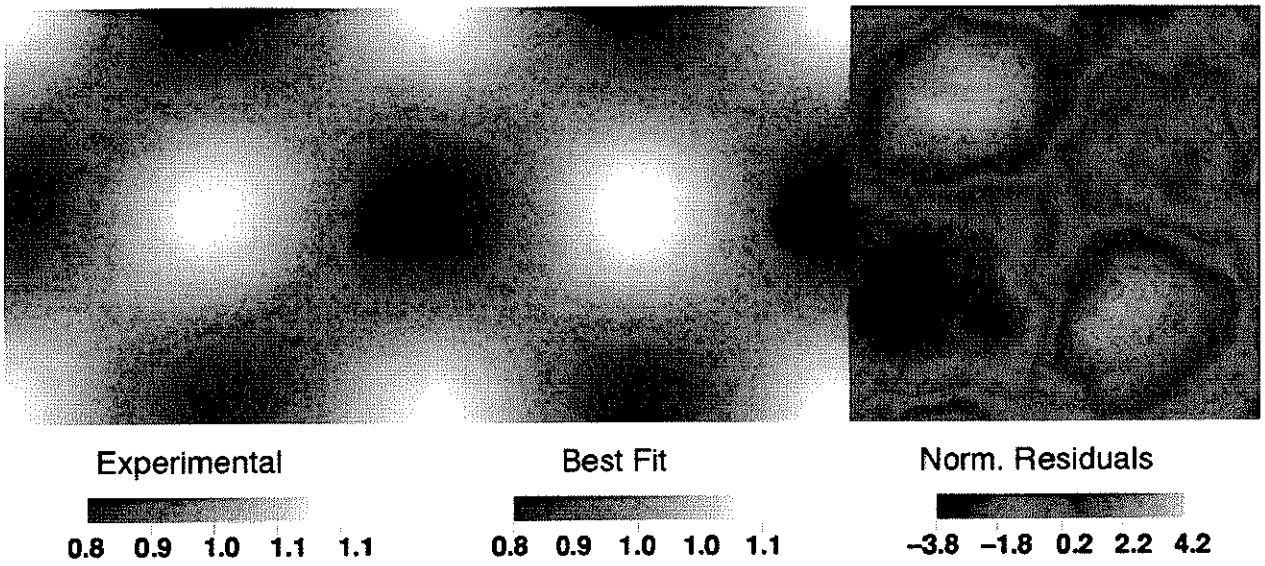

Figure 3. Experimental image (left), best-fit simulated image (center), and normalized residuals (right).

The simulated images were compared with the experimental images using the χ^2 goodness-of-fit test. The χ^2 statistic was defined as

$$\chi^2 = \frac{1}{k-s}\sum_{i=1}^{k}\left(\frac{f_i^{obs} - f_i^{calc}}{W_i}\right)^2$$

where f_i^{obs} and f_i^{calc} correspond to the observed and simulated image intensities, k is the number of observations, and s is the number of independently adjustable parameters. While the χ^2 statistic is not explicitly used in the fitting procedure, it is useful for comparing one fit to another.

The results of the nonlinear least-squares optimization are summarized in Table 2. In this table, values for defocus deduced from careful analysis of the contrast of the amorphous phase present at the edge of the sample are shown along with a value of χ^2 calculated based on this defocus value. Also shown are the corresponding best-fit defocus and χ^2 values. In each case, good agreement is obtained between the amorphous-phase contrast method and the nonlinear least-squares method.

Table 2. Comparison of defocus determined from amorphous-phase analysis and defocus determined from fitting procedure using χ^2.

Micrograph	Defocus determined from amorphous-phase analysis	χ^2	Defocus determined from fitting procedure	χ^2
1	0	3.95	0.79	2.35
2	-40	13.0	-43.3	10.6
3	-70	38.1	-66.7	28.8
4	-105	113.0	-98.9	19.6

While the amorphous-phase contrast method gives reasonable values for defocus, it does not determine thickness. The best-fit defocus and thickness values for the four defocus values investigated are plotted in Fig. 4. The optimization found that the sample in this case was extremely thin, about one or two unit cells thick.

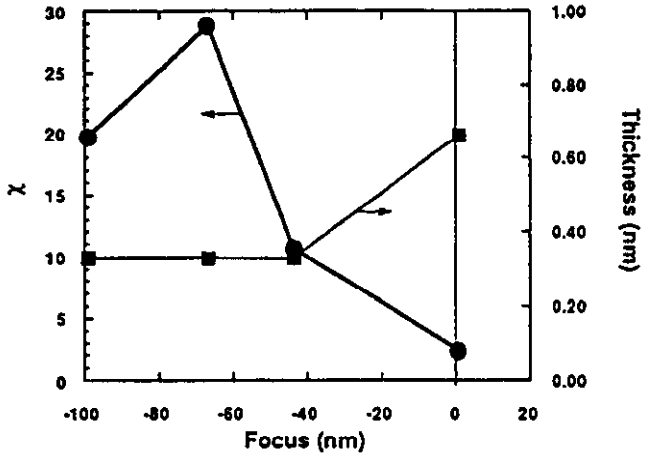

Figure 4. Goodness-of-fit and best-fit thicknesses as functions of focus.

Conclusions

Using nonlinear least-squares optimization, we have determined thickness, defocus, and beam/specimen tilt for four different defoci from a single area of a niobium bicrystal. The fitting procedure is quite sensitive to both thickness and defocus. While important to obtaining a good fit, the fitting procedure is significantly less sensitive to beam/specimen tilt.

Our results demonstrate that nonlinear least-squares methods can be applied to uniquely determine thickness and defocus from experimental high-resolution electron micrographs. The nonlinear least-squares method is far superior to "counting clicks" and better and more efficient than analyzing amorphous-phase contrast for determining defocus. Nonlinear least-squares methods can be applied to simultaneously determine thickness, defocus, and beam/specimen tilt.

Electronic-Structure Calculations at Metal Grain Boundaries

E. Sowa and A. Gonis

Introduction

We now have two computer codes that use the Real-Space Multiple-Scattering Theory (RSMST) method to calculate the electronic structure of systems with extended defects. Results from the first code, which works entirely in real space without using artificial boundary conditions, have been reported here before. Efforts to make this code charge self-consistent have begun, but in recent months we have concentrated on using the second code because it is already charge self-consistent. This second code uses periodic boundary conditions in the plane of the interface and the RSMST algorithm in the direction perpendicular to the interface. Its applicability is therefore restricted to those interfaces which are two-dimensionally periodic, but many systems of interest to our group fall into that category. This code is based on the Layer Korringa-Kohn-Rostoker (LKKR) code of MacLaren, but with the LKKR's layer-doubling algorithm replaced by the RSMST's removal-invariance algorithm. For fcc materials, layer-doubling works well for low-Miller-index planes, but when planes are more closely spaced than (210), the algorithm no longer converges. Removal invariance is more forgiving, allowing us to consider the high-Miller-index grain boundaries of interest to our group.

The LKKR-RSMST code has been shown to work well with (100) and (111) planes, but its ability to handle high-Miller-index planes in practice must be confirmed. We are testing this by using (310) planes to build a bulk Cu crystal and comparing the results to a carefully converged calculation based on (111) planes. We found that the obvious choice for the repeating unit in the removal-invariance algorithm, namely a single-atom (310) layer, is not a good one: the removal invariance did not converge. To understand why, we note that there is a trade-off between angular-momentum and real-space quantities in the convergence properties of the removal-invariance algorithm. The single-atom (310) layer does not contain any nearest neighbors, and the vector between atoms on adjacent layers is closer to being parallel to the interface than perpendicular. If the calculation were carried out to infinite angular momentum, this would make no difference, but in practice the angular-momentum expansion must be truncated.

We redid the calculation with a three-layer compound iterating unit and a fixed bulk potential. This has the following advantages: (1) the removal-invariance algorithm does converge in areas where the simpler iterating unit caused it to fail, and (2) the iterating unit does contain nearest neighbors, the scattering between which is treated exactly before the removal-invariance algorithm is applied. The bulk density of states thereby obtained is essentially identical to that calculated based on (111) planes (see Fig. 5). When charge self-consistency is introduced, the resulting total energy is 10 mRy higher. The present calculations indicate that we will be able to proceed with the Cu $\Sigma 5(310)$ tilt grain boundary charge-self-consistent total-energy calculation as the next step.

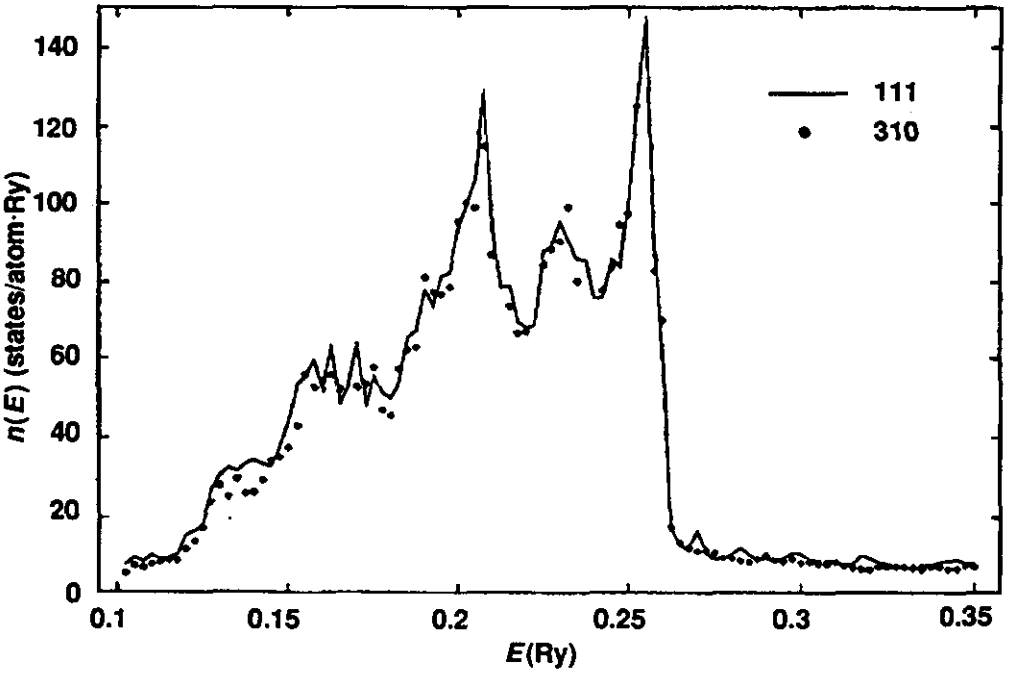

Figure 5. Electronic density of states for bulk copper calculated using (111) planes (solid line) and (310) planes (symbols).

References

1. H. F. Fischmeister, W. Mader, B. Gibbesch and G. Elssner, "Preparation, properties, and Structure of Metal/Oxide Interfaces," in *Interfacial Structure, Properties, and Design*, M. H. Yoo, W. A. T. Clark, and C. L. Briant, Eds. (Materials Research Society, Pittsburgh, PA, 1988), pp. 529–540.
2. Wayne E. King, G. H. Campbell, A. Coombs, M. J. Mills and M. Rühle, "HREM Investigation of the Structure of the Σ5(310)/[001] Symmetric Tilt Grain Boundary in Nb," in *Defects in Materials*, P. D. Bristowe, J. E. Epperson, J. E. Griffith, and Z. Liliental-Weber, Eds. (Materials Research Society, Pittsburgh, PA, 1991), pp. 39–46.
3. S. M. Foiles, Murry S. Daw and Robert B. Phillips, "Tilt Boundaries in bcc Metals: Comparison of Results Using Different Interatomic Interactions," in *Defects in Materials*, P. D. Bristowe, J. E. Epperson, J. E. Griffith, and Z. Liliental-Weber, Eds., *MRS Symp. Proc.* **209**, 65–70 (1991).
4. J. A. Moriarty, *Phys. Rev. B* **42**, 1609 (1990).
5. M. J. Mills and M. S. Daw, "The Study of Defects in Metals Using HRTEM and Atomistic Calculations," in *High-Resolution Electron Microscopy of Defects*, R. Sinclair, D. J. Smith, and U. Dahmen, Eds., *MRS Symp. Proc.* **209**, 15 (1990).
6. K. L. Merkle and D. J. Smith, "Atomic Structure of Symmetric Tilt Grain Boundaries in NiO," *Phys. Rev. Lett.* **59**, 2887 (1987).
7. D. J. Smith, "Progress Towards Quantitative HREM," presented at Frontiers of Electron Microscopy in Materials Science, Oakland, CA, 1992.

8. Jorge J. Moré, Burton S. Garbow, and Kenneth E. Hillstrom, *User Guide for MINPACK-1*, Argonne National Laboratory, Argonne, IL, ANL-80-74 (1980).
9. J. J. Moré, "The Levenberg-Marquardt Algorithm: Implementation and Theory, Numerical Analysis," in *Lecture Notes in Mathematics*, G. A. Watson, Ed. (Springer-Verlag, 1977), pp. 630.
10. P. Stadelmann, "EMS—A Software Package for Electron Diffraction Analysis and HREM Image Simulation in Materials Science," *Ultramicroscopy* **21**, 131–146 (1987).

Publications and Presentations

Refereed Papers

1. Erik C. Sowa, J. M. MacLaren, X.-G. Zhang, and A. Gonis, "Self-Consistent Electronic-Structure Calculations for Interface Geometries," *Proc. Mater. Res. Soc.* **253**, 405 (1992).
2. Erik C. Sowa, A. Gonis and X.-G. Zhang, "The Real-Space Multiple-Scattering Theory and the Electronic Structure of Grain Boundaries," *Proc. Mater. Res. Soc.* **229**, 129 (1991).
3. G. H. Campbell, W. E. King, S. M. Foiles, P. Gumbsch and M. Rühle, "Combined Experimental and Theoretical Determination of the Atomic Structure of the (310) Twin in Nb," *Proc. Mater. Res. Soc.* **238**, 163 (1992).
4. G. L Nutt and Wayne E. King, "Use of Shock Waves to Measure Adhesion at Interfaces," in *Intermreallic Matrix Composites*, D. B. Miracle, J. A. Graves, and D. L. Anton, Eds. (Materials Research Society, Pittsburgh, PA, 1992).

Presentations

1. E. C. Sowa, J. M. MacLaren, X.-G. Zhang, and A. Gonis, "Self-Consistent Electronic-Structure Calculations for Interface Geometries," Materials Research Society Meeting, December 1991, Boston, MA.
2. E. C. Sowa, A. Gonis, J. M. MacLaren, and X.-G. Zhang, "Self-Consistent Electronic-Structure Calculations for Grain Boundaries," American Physical Society Meeting, March 1992, Indianapolis, IN.
3. G. H. Campbell, W. E. King, S. M. Foiles, and M. Rühle, "High-Resolution Electron Microscopy Investigation of the (710) Twin in Nb," Frontiers of Electron Microscopy in Materials Science, Oakland, CA, 1992.
4. W. E. King and G. H. Campbell, "Quantitative Determination of Thickness and Defocus Using Nonlinear Least Squares Optimization," Frontiers of Electron Microscopy in Materials Science, Oakland, CA, 1992.
5. G. H. Campbell, W. E. King, S. M. Foiles, P. Gumbsch, and M. Rühle, "Combined Experimental and Theoretical Determination of the Atomic Structure of the (310) Twin in Nb," Materials Research Society Program Book with Abstracts (December 2–5, 1991, Boston).
6. G. L Nutt and W. E. King, "Use of Shock Waves to Measure Adhesion at Interfaces," in *Intermetallic Matrix Composites*, Materials Research Society Program Book with Abstracts (April 27–May 1, 1992, San Francisco, CA), p. 351.

7. E. C. Sowa and A. Gonis, "The Real-Space Multiple-Scattering Theory: A First Principles Method for the Computation of the Electronic Structure of Defects," NATO/ASI "Equilibrium Structure and Properties of Surfaces and Interfaces," Porto Carras, Greece, August 18–30, 1991.

Conference Organization

1. W. E. King, C. Allen, S. Bradley, T. Nolan, and U. Dahmen, Frontiers of Electron Microscopy in Materials Science, Oakland, CA, April 21–24, 1992.

Energetic Materials

R. L. Simpson, *Thrust Area Leader*

Overview

The overall energetic materials program is directed toward the development, experimental characterization, and theoretical understanding of high–energy-density materials with an emphasis on enhanced safety. Our basic research consists of efforts to synthesize new high-energy materials, to determine molecular structure-reactivity relationships, and to develop the means to molecularly design new compounds. This last activity consists of *ab initio* calculations of crystal structures, heats of formation, thermodynamic stability, and the equation-of-state of detonation products.

Several changes have occurred in the energetic materials thrust area. J. Bauer, who had been doing postdoctoral work with D. Calef accepted a career position with A Division. We will have three new postdoctoral researchers by the end of this fiscal year. L. Fried, a theorist currently doing postdoctoral research with Prof. Mukamel at the University of Rochester, will be working with A. Ruggiero in our femtosecond spectroscopy effort. He will address energy transport between inter- and intramolecular vibrational modes in high explosives, directly modeling Ruggiero's experimental results with molecular dynamic simulations. K. Westerberg will be working with A. Nichols to develop numerical methods for the reactive flow modeling of energetic materials. Currently, Westerberg is doing his doctoral research on fluid mechanics and numerical methods under Dr. Finlayson at the University of Washington. T. Land, from UC Irvine, will be working with both the energetic materials program and W. Siekhaus in the Condensed Matter and Analytical Science Division. Her work will consist of applying atomic force microscopy and other surface-analysis techniques to energetic materials.

The synthetics effort that has traditionally been reported here is currently being funded by LDRD SR. During the last two years, a wide range of nitrogen heterocycles with very high nitrogen content has been synthesized. These materials have been found to be insensitive and of low to moderate energy. One molecule, designated HNX, has been shown to have sensitivity and performance similar to TATB. Another recently synthesized material, PZO, is as thermally stable as TATB, and somewhat more impact sensitive, but has 5 to 20% more energy. In FY 93, we plan to continue this work as part of the WSR energetic materials thrust area.

High-Pressure Reaction Chemistry

M. F. Foltz

High-pressure diamond anvil cell (DAC) work has continued with static measurements addressing the effects of pressure on 1,3,5-triamino-2,4,6-trinitrobenzene (TATB).

It was noted in earlier work that TATB changes from yellow at ambient, to red, then black, and finally black with shiny inclusions in the highest-pressure part of the DAC. Since TATB is known to pack in hydrogen-bonded graphitic sheets at ambient conditions, it had been surmised that these color changes corresponded to sliding of these planes under nonhydrostatic pressing. As the aromatic rings come into alignment, interplanar electron donor-acceptor interaction increases until the rings come into complete alignment. With total alignment established, the material then has free electron transport along the rings, causing shiny regions to appear in the material.

To test this picture, assorted nitroaromatic compounds related to TATB by the addition or subtraction of amino and nitro groups were chosen to observe color changes under pressure. The crystal structures of these compounds were known to contain varying degrees of intermolecular hydrogen bonding, but none as extensive as that optimized in TATB. Most structures were not packed graphitically like TATB, but were, to varying degrees, fit into herringbone lattices with no free slip planes (neighboring rings inclined at steep angles, 50 to 90°). For example, in the series in which amino groups are cumulatively removed from TATB [1,3-diamino-2,4,6-trinitrobenzene (DATB), 2,4,6-trinitroaniline (TNA), and 1,3,5-trinitrobenzene (TNB)], the molecules fall into increasingly angled packing. Intermolecular amino-nitro group hydrogen bonding guides DATB into strongly linked chains, whereas the true herringbone lattice of TNB arises from weak ring hydrogen-nitro group bonding. The color response to pressure for DATB followed the expected path of TATB-like coloration (red → black → black + few shiny inclusions); TNB exhibited only red coloration. Even DATB did not develop the size inclusions that TATB did. It is thought from these observations that the herringbone structure prevents molecular realignment under pressure at ambient temperature. Other materials tested included the graphitic 2,6-diamino-3,5-dinitro-1,4-pyrazine (ANPZ) (exactly the same as TATB) and herringbone-structured 2,3,4,6-tetranitroaniline (TENA), picric acid, trinitrotoluene (TNT), and benzotrifuroxan (BTF). Both TENA and BTF color easily like DATB and have neighboring aromatic rings inclined at modest angles compared to those of picric acid and TNT. DATB undergoes a phase transition at 217°C to a crystal packing like that of TATB. It is possible that there are high-pressure transitions from herringbone to stacked lattices that could account for the relatively easy color change of TENA BTF and DATB.

Some aromatic donor-acceptor complexes were made with the nitroaromatic HEs listed above and melamine or phloroglucinol. Due to the relative insolubility of melamine in most solvents, stronger solvents such as 1-methyl-2-pyrrolidinone were used in those complexation attempts. The results were ambiguous because the nitroaromatic tended to complex as easily with the solvent as with the chosen donor melamine. Even after 48 hr of heating in an Abderhalden to drive off lattice-bound solvent, enough solvent remained trapped to show up in FTIR spectra. As a result, most complexation was done with the easily dissolved phloroglucinol. Except for TATB, which is insoluble in its own right, most of the HEs tried complexed easily in solution and crystallized out readily. The strongest coloration came from TENA, which upon crystallization was a deep purple. Most complexes however, exhibited only a slight to modest red shift in coloration (e.g., from yellow for HE alone to yellow-orange for the complex). One

complex pressed in the DAC was phloroglucinol: DATB, which color-shifted even easier than DATB alone, forming very nice, shiny inclusions. This material was left at 100°C overnight, after which the shiny inclusions were seen to have grown.

Work has been completed on the thermal stability of CL-20. The high-temperature phase transition seen in DSC traces that was attributed in earlier China Lake work to formation of a "delta" phase, is now known to correspond to a beta→gamma phase conversion. This conversion, normally occurring at much lower temperature for dry samples, shifts dramatically to high temperature with the inclusion of water. This is due to the ease of hydration of a third, alpha phase, which occupies a stability region bordering both beta and gamma. The addition of water essentially creates a new polymorph with different phase boundaries than those of the dry phase. As a result, the phase lines intersecting the ambient pressure line shift with the water content of the sample, not only for alpha but also for the neighboring beta phase. In addition, the beta→alpha transition has been seen to occur at low temperature (37°C) where no such polymorph transition had been seen before. Previous transitions showed conversion to gamma phase. The choice of a solvent (poly(caprolactone)triol)—which by -OH substitution is known to favor alpha phase formation—along with addition of water to encourage heavily hydrated (and most stable) polymorph, intercepted the beta→gamma transition in the intermediate alpha phase. This result is important to formulators who must consider the possibility of low-temperature phase transitions to lower density phases in their formulations. Since beta phase is a common (albeit easily cleaned out) contaminant in CL-20, it is useful to know that there exists a *solvent-dependent* transition to lower-density alpha and gamma at temperatures ≤37°C.

Presentations

M. F. Foltz and A. L. Nichols III, "Pressure Dependence of the Reaction Propagation Rate of TATB to 40 GPa," Workshop on the Fundamental Physics and Chemistry of Combustion, Initiation, and Detonation of Energetic Materials, March 3–6, 1992, Los Alamos National Laboratory, Los Alamos, NM.

M. F. Foltz and A. L. Nichols III, "Pressure Dependence of the Reaction Propagation Rate of TATB in the Diamond Anvil Cell," March 1992 Meeting of the American Physical Society, Indianapolis, IN.

M. F. Foltz, C. L. Coon, F. Garcia, and A. L. Nichols III, "The Thermal Stability of Hexanitrohexaazaisowurtzitane Polymorphs," JANNAF Workshop: Review of Advancements with CL-20, 10 April 1992, NASA Kennedy Space Center, FL.

Molecular Modeling

D. Calef

Our efforts at molecular modeling are focused on improved predictive capabilities for densities and heats of formation for new compounds. This will greatly aid the synthetic effort. We have also worked on molecular dynamics models in our effort to understand the transfer of energy from phonon modes to vibrational modes. This process is key to initial reactivity of a molecule in a hot medium.

The modeling effort involves two major computer codes. The densities are calculated using the POLYGRAF software package from Molecular Simulations Inc. The calculations are performed using constant-stress classical molecular dynamics. The molecule is placed in periodic cell whose size and shape can adjust to minimize the energy. Both molecular structure and cell parameters are minimized.

We have our first concrete results on energetic materials. Calculated and measured densities (in g/cm^3) for several explosives are given below. Also given is the result of group additivity estimates.

Explosive	Experiment	MM	Group
HMX	1.905	1.65	1.77
HNB	2.02	2.03	2.01
HNS	1.74	1.73	1.73
PETN	1.78	1.68	1.71
TATB	1.94	1.77(1.93)	1.79
TNGU	2.04	1.90	2.02
TNT	1.65	1.66	1.67
DNB	1.57	1.51	1.60
RDX	1.80	1.72	1.77
BTF	1.901	2.03	2.08
ANPZ	1.84	1.81	1.91
PZO[a]	1.913	1.92	1.92

[a] 2,6-diamino-3,5-dinitro-1,4-pyrazine-N-oxide

The comparison is relatively good and suggests the route for improvement. The number in parentheses by TATB is for a model with the TATB molecule constrained to be planar. This suggests that improvements in the force field will greatly improve accuracy.

We have also investigated the coupling of high-frequency phonon modes to vibrational modes in a simple model diatomic fluid. The results show that the straightforward application of the methods used in our phonon studies of atomic fluids will not work. Anharmonic effects in molecular oscillators cause spuriously broadened frequency distributions. A new approach seems to called for, where high-frequency anharmonic modes are treated as local modes, while phonons are treated as normal modes.

Publication

J. D.Bauer and D. F.Calef, "Harmonic Analysis of Phonon Echoes in Liquids," *Chem. Phys. Lett.* **4**, 187 (1991).

Experimental Studies of Energy-Transfer Dynamics in Energetic Materials

A. J. Ruggiero

The NEPA environmental assessment documents required for operation of the laboratory are still being processed at DOE. Procurement of equipment for construction of the femtosecond laser system, diagnostics, and experimental apparatus is still under way. The custom nature of much of the equipment, resulting in long lead times coupled with the slow release of funds, is resulting in long acquisition delays. Design, assembly, and testing of most of the subsystems for the amplified femtosecond laser system, however, are nearly complete. The mode-locked picosecond master oscillator system has been completed and has been modified for single-pulse cavity dumped operation and injection seeding in order to accommodate a new, high-power, dual-laser-head, regenerative amplifier design. Operation with the new Nd:YAG regenerative amplifier design has resulted in a 20-fold increase in average power over the design used in Ref. 4, whereas changes in the master oscillator used for injection seeding will result in a threefold decrease in pulsewidth. Recent acquisition of the rest of the required injection seeding and acousto-optic driver electronics (May 1992) should permit completion of this part of the system within the next month or so. Computer interfacing of the dual-phase lock-in amplifier, photon-counting detection equipment, system diagnostics, and precision translation stages is complete and has been tested. Programs are currently being developed for the synchronous use of this equipment during experimental data acquisition as well as data storage, manipulation, and analysis. Arrival of the monochromator required for the proposed work is expected in June 1992.

Initial experiments will involve the characterization of vibron and phonon dynamic in single crystals of HMX. These experiments will involve stimulated Raman pumping of vibrations in the 30- to 300-cm^{-1} "doorway" region and subsequent observation of energy relaxation and redistribution via time-resolved incoherent Raman probe scattering. The anticipated start date of these measurements is late summer.

Publications

1. A. J. Ruggiero, "Actively Modelocked Lasers Produce Picosecond Pulses," *Laser Focus World*, Feature Article, 55–66 (February 1992).
2. A. J. Ruggiero, N. F. Scherer, and G. R. Fleming, "Optical Continuum Generation and Pulse Shortening at 100-kHz Repetition Rates," *Opt. Lett.*, submitted for publication.
3. N. F. Scherer, A. J. Ruggiero, H. Guttman, and G. R. Fleming, "Colliding Pulse Modelocking in a Cavity Dumped Anti-Resonant Ring Dye Laser," *Opt. Lett.*, submitted for publication.
4. A. J. Ruggiero, "Active Modelocking and Phase Stabilization of a Cavity Dumped Diode Pumped Nd:YAG Mini-Laser," *CLEO/QELS, 1992* submitted for publication.
5. A. J. Ruggiero, "Unidirectional Single Pass Acousto-Optic Cavity Dumping of Pulsed Lasers," LLNL, Disclosure and Record of Invention, in preparation.

Presentations

1. A. J. Ruggiero, "Time Domain LIDAR," U.S. DOE, Washington DC, April 1992.
2. A. J. Ruggiero, "Femtosecond Spectroscopy of High Explosives," UC Berkeley, May 1992.

Plutonium Research

L. R. Newkirk, *Thrust Area Leader*

Overview

The tasks in the plutonium thrust continue to be centered on supporting the DOE's enhanced nuclear safety effort through improving our scientific understanding of liquid plutonium and uranium corrosion of attractive containment materials. We anticipate that improvements in the scientific basis of this activity will eventually allow successful design of new, more effective containment materials, particularly to contain composite U/Pu alloys. As an added bonus, this understanding will also contribute to the development of metal molds and improved foundry crucibles for the reconfigured plutonium complex (Rocky-II). As discussed in detail in the research proposal, we passed a decision point in October influencing the direction of the technical activities. The Auger spectroscopy results, which disclosed no anomalous differences between vanadium, tantalum, and niobium grain boundaries, have caused us to suspend the grain-boundary modification effort pending completion of the studies of stress-induced embrittlement. In addition, commissioning of the high-purity–atmosphere plutonium exposure furnace has been delayed until FY 93. This decision was driven by requirements of the Director's plutonium inventory-reduction program, which will shortly force relocation of the furnace glove box.

The remaining FY 92 program consists of two experimental efforts, one of which is new, and our theoretical focus on actinide electronic structure. Our experimental efforts continue to focus on developing a basic understanding of liquid actinide corrosion by identifying and characterizing the operating mechanism. Our primary tool is still the study of stress-induced embrittlement with the goal of establishing the existence or absence of temperature-dependent ductility troughs in vanadium and niobium. Our second effort is a new, relatively small activity to understand grain-boundary behavior under stress in the absence of liquid attack. To provide a theoretical basis for future alloy design efforts, we are continuing to pursue development of an *ab initio* electronic-structure capability, which we expect to begin providing a theoretical description of the effects of plutonium incorporation into a refractory-metal surface late this year.

Liquid-Metal Embrittlement

G. F. Gallegos, J.-S. Huang, and M. P. Stratman

We have continued our efforts to understand liquid-metal embrittlement by establishing the existence or absence of a classical ductility trough in niobium exposed to liquid plutonium. Since the effects of embrittlement may not be reversible, establishing the recovery of ductility at temperatures above the minimum is an unusually difficult procedure, requiring major changes in our experimental technique. In this technique, the sample and testing media (liquid plutonium) are to be heated to the test temperature without contacting each other, then brought into contact, followed immediately by

tensile loading. This allows no grain-boundary penetration of liquid plutonium before loading at the test temperature. A test on niobium at 1000°C showed no embrittlement of the niobium upon immediate contact with the plutonium. However, as the test progressed, the specimen fractured with little evidence of significant ductility. It may be possible that the test temperature was not above the ductility trough. Further analysis and tests at lower and higher temperatures (~750 and 1200°C) still need to be done to establish a firm conclusion.

We have continued to study the tensile behavior of V-Ta binary alloys in liquid plutonium. Previously we reported that a V-24%Ta alloy was embrittled by liquid plutonium. Characterization of this alloy showed some segregation of the tantalum, but the alloy was found to be single phase, and the segregation was at random locations and not necessarily at the grain boundaries. During this reporting period, we prepared and tested V-10%Ta and V-2.5%Ta alloys. To avoid the segregation problems encountered earlier, the alloys were arc-melted and then melted twice in an electron-beam furnace. The results showed the V-10%Ta alloy was also embrittled by liquid plutonium. At 1000°C, the V-10%Ta alloy has an ultimate tensile strength of 177 MPa and 12% elongation to failure in vacuum, and 96 MPa and 0.7% in liquid plutonium. This embrittlement was likely due to grain-boundary penetration by liquid plutonium because our previous experiments on V-24%Ta indicated that liquid plutonium penetrated along grain boundaries. We also investigated the grain-boundary structure of V-10%Ta using transmission electron microscopy. The tantalum was uniformly dissolved in vanadium, and there was no presence of second-phase material. Therefore, any modification of the properties of the vanadium grain boundaries due to the addition of tantalum is most likely on an atomistic scale. We are attempting to study the difference in grain-boundary energy in a study described in the next section.

Grain-Boundary Behavior

F. Y. L. Génin

The object of this project is to develop a better understanding of basic transport phenomena at grain boundaries, with the expectation that this will contribute to our understanding of liquid-metal corrosion. We are examining both (1) materials of specific interest to liquid plutonium corrosion (vanadium and V-10%Ta) and (2) ideal materials containing only a single grain boundary (copper bicrystals) in the three tasks described below.

Electromigration in a Copper Bicrystal

The goal of this task is to study the behavior of a grain boundary under a very high current density, the effects of which are analogous to applying a tensile stress. We hope to be able to acquire some fundamental properties of the grain boundary and some basic understanding of the transport phenomena at the grain boundary. As a side benefit, this would also help to model the effects of electromigration at grain boundaries in thin films used in the integrated circuit industry. At present, bicrystals of copper have been prepared, and an argon furnace with a high-current power supply is being assembled for the experiment.

Thermal Grooving Under Stress in Copper Bicrystals

When a metal is annealed, thermal grooves develop at grain boundaries on the surface. If sufficient stress is applied to the metal, the shape of the grooves on the surface can change significantly. A model of thermal grooving at a grain boundary under stress has been developed by Mullins, Wynblatt, and Génin. This project aims at comparing the groove's shape predicted by the model with the experimental profiles of stressed thermal grooves developed in a copper bicrystal. For initial testing, polycrystalline samples of copper shaped for tensile testing with a 0.1-mm-thick window in the center have been prepared by miniature machining. Following installation of an Instron machine and this initial testing, we will proceed with the bicrystal.

Grooving in Vanadium and V-10%Ta Alloy

The goal of this project is to measure the effect of tantalum alloying on grain-boundary energy. Polished polycrystalline samples are being heat-treated for characterization by interference microscopy and STM to determine the profiles of grain-boundary grooves and measure their energy. Preliminary annealing of the vanadium and V-10%Ta samples showed very different grain-growth kinetics, due probably to solute pinning of the grain boundaries. As discussed in the liquid-metal–embrittlement studies above, we know that the addition of 10% tantalum to vanadium dramatically increases the susceptibility to liquid-plutonium embrittlement.

Electronic-Structure Calculations

A. Gonis and P. Sterne

The long-term goal of this task is to develop the *ab initio* capability to predict the influence of clusters or layers of actinide atoms on the properties of a refractory-metal surface. This is a very ambitious goal, and our current effort is focused on developing and validating the required calculational tools.

The Electronic Structure of Monoclinic Plutonium

Our major computational effort during the first half of this fiscal year was to calculate the electronic structure of the most prevalent phase of plutonium—the monoclinic phase containing 16 atoms per unit cell. The monoclinic phase of plutonium can be viewed as a distorted hcp structure. Quite remarkably, plutonium does not stabilize in the hcp structure. One of our aims in this study is to identify the electronic origins of phase stability of pure plutonium and plutonium alloys and to understand their preference for the fcc over the hcp phase.

As in the last report, calculation of the electronic structure of alpha-plutonium presents a number of challenges to first-principles approaches. First, the 16-atom unit cell is larger than the systems customarily treated with such techniques. In addition, the monoclinic structure is much less symmetrical than most systems normally considered. Furthermore, the need to treat relativistic effects, including the spin-orbit coupling of the f-electron bands, increases the size and complexity of the calculation.

In the case of alpha-plutonium, the positions of the atoms in the unit cell have been determined experimentally.[1,2] There is a slight difference between the parameters specified in Refs. 1 and 2, but it is not expected to affect significantly the results of the calculations. In our studies, we chose the parameters given in Ref. 1.

We have used a newly developed computational scheme (described briefly in the last report) to calculate the electronic densities of states (DOSs) for the fcc, hcp, and the monoclinic structures, both in the semirelativistic approximation (i.e., including all relativistic effects except spin-orbit coupling) and within a fully relativistic approach. The fully relativistic calculations for the alpha phase were completed this fiscal year. The large size of the 16-atom unit cell and the increase in the Hamiltonian matrix dimension by a factor of 2 when spin-orbit effects are included make this a very difficult calculation. Figure 1 shows the DOSs of the various phases of plutonium calculated.

In all cases plotted in Fig. 1, the DOSs are based on fully self-consistent calculations for the electronic charge density. The fcc case has a DOS minimum at the Fermi energy (E_F) for both the semirelativistic and fully relativistic results. This minimum is more prominent in the fully relativistic case due to the increased splitting from the spin-orbit term. Spin-orbit coupling also creates splittings in other peaks above and below E_F. A DOS minimum at E_F is frequently associated with a relative increase in phase stability over competing structures, which may have a larger number of states at E_F. The low DOS

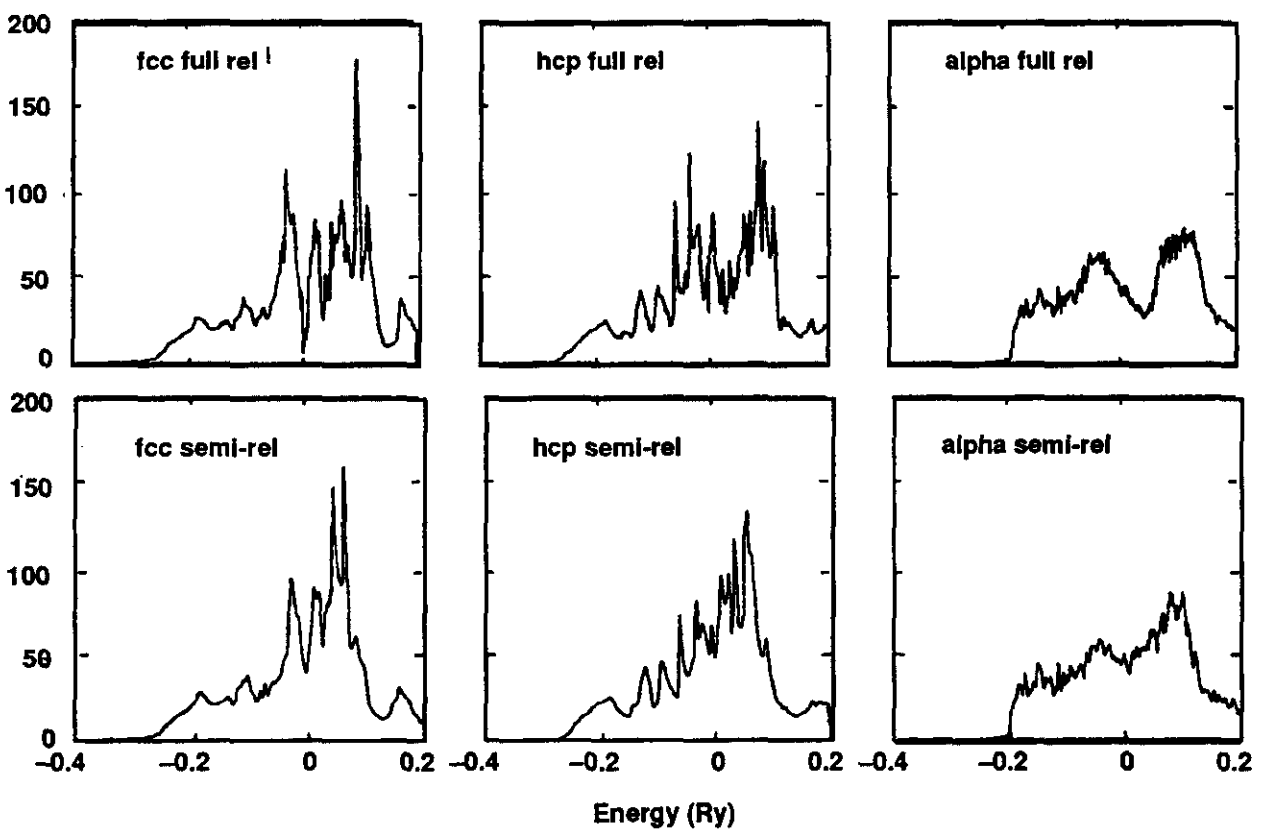

Figure 1. Density of states (per atom-Rydberg) for various plutonium structures as indicated.

at E_F exhibited by the fcc phase is probably an important feature in the stabilization of the fcc (delta) phase of plutonium and its alloys. (At the same time, it should be pointed out that a low DOS at E_F does not *guarantee* the stability of a structure. The *total* energy, which involves an integral over the entire DOS as well as other contributions, provides a more proper indication of phase stability).

In contrast to fcc, hcp structure shows no clear minimum at E_F. As in fcc, however, the DOS shows a considerable amount of structure and spin-orbit coupling, once again leading to split peaks. The alpha phase can be considered as a distorted hcp structure, so the ideal hcp structure provides a useful reference for the electronic properties.

In contrast to fcc and hcp, in which all the atoms are equivalent, the alpha phase contains eight inequivalent sites. Two features are immediately apparent by comparison with the fcc and hcp calculations. First, there is considerably less structure in the DOS of the alpha phase than in either of the other two. The reduction in symmetry leads to significant smearing of the sharp features seen in the other semirelativistic calculations. The valence band extends down to only 0.2 Ry below E_F (at 0), in contrast to the other two cases, which have bandwidths of the order of 0.27 to 0.30 Ry. The fully relativistic results for the monoclinic phase show the increased splitting due to the spin-orbit term, and the narrowing of the bandwidth compared to the hcp and fcc phases.

Our calculations indicate that

- The monoclinic phase shows an increase in f-occupancy and a reduction in spd occupancy compared to the hcp and fcc structures.
- A shift in the DOS from s to d when compared with fcc and hcp.
- A downward shift of f bands with respect to spd bands. The narrowing of the bands mentioned in the last paragraph can be traced to this phenomenon in the alpha phase, compared with the fcc or hcp structures. It arises because the f states have a much more localized character than the spd states.

The Electronic Structure of Plutonium Alloys

In collaboration with Prof. Peter Weinberger, we have started calculating the electronic structure of Pu-Ga alloys, at 5 and 10 at.% gallium content. These calculations are expected to be finished within the next few months.

References

1. W. H. Zachariasen and F. H. Ellinger, *Acta Crystall.* **16**, 777 (1963).
2. C. E. Olson, "The Orientation Relationship Between Delta-Phase Plutonium and Alpha-Phase Plutonium,"*J. Nucl. Mater.* **168**, 326 (1989).

Publications, Reports, and Presentations

F.Y. Génin, W.W. Mullins, and P. Wynblatt, "Thermal Instabilities in Polycrystalline Thin Films," Symposium on Surface Science, La Plagne, France, March 1992.

T. S. E. Summers, P. G. Curtis, R. S. Juntz, and R. L. Krueger, *Metal-Carbide Multilayers for Molten Pu Containment*, LLNL Report UCRL-ID-109383, December 1991.

Synchrotron Radiation-Based Materials Science

J. Wong, *Thrust Area Leader*

Overview

The objective of this thrust is to understand the role of structure (atomic and electronic) in determining the physico-chemical properties of materials and their processing. The tasks defined in this thrust area take advantage of the various unique characteristics of synchrotron radiation such as high intensity, high collimation, high polarization, and broadband tunability from vacuum ultraviolet (VUV) to hard x ray to probe the structure of matter on an element-selective basis at different levels. The research areas involve both expansion of our existing capabilities in material characterization using these powerful photon sources and development of new capabilities (a) to probe dilute species in bulk materials, (b) to determine geometric and electronic structure of surfaces and nano-scaled materials, (c) to unravel chemical dynamics of high-temperature–reaction systems and phase transformation *in situ* in real time down to the millisecond range and (d) to develop new soft x-ray monochromator materials for programmatic needs and the next-generation synchrotron sources.

Progress

Summary of Technical Highlights

[Some synchrotron radiation-based research is reported elsewhere (see reports by Colmenares and Tobin).]

- Determined band dispersion of localized valence states in LiF(100).
- Extended photoemission studies of quantum dots from the VUV to the soft x-ray region.
- Determined the structure and chromium site-specific chemistry in a series of lithium metal hexafluoride solid-state laser materials.
- Upgraded our SGM beamline 8-2 at the Stanford Synchrotron Radiation Laboratory (SSRL) to ultrahigh resolution.
- Successfully tested a new compact diffractometer-IR thermal imaging system to follow the chemical dynamics of a series of high-temperature carbide and boride syntheses with time-resolved diffraction.
- Critically evaluated the state-of-the-art quick-scan EXAFS capability at HASYLAB, Germany.
- Implemented an ADIBAT microcomputer program to calculate adiabatic temperatures for a variety of solid-state combustion reactions.
- Performed the first synchrotron reflectivity and rocking curve measurements of YB_{66} single crystal.

Personnel

After a successful dedicated run of SPEAR with the newly constructed injector last fall, SSRL has now been scheduled for a 7-month operation from mid-February and will be delivering beam time to users on a more regularly and extended basis in the future (projected to be 7–9 months in FY 93). Phil Waide has been assigned on a part time basis to render on-line technician support to PRT users on beamline 10-2. Randy Hill (not presently supported by this Thrust) has been recruited as a mech tech to work with Jim Tobin to keep up beamlines 8-1 and 8-2. On November 16, 1991, Joe Wong returned from HASYLAB, Germany, after completing the first 5 months of his Humboldt Award work on quick-scanning EXAFS and YB_{66} study.

Band Dispersion of Localized Valence States in LiF(100)

F. J. Himpsel,* L. J. Terminello, D. Lapiano-Smith,* E. Eklund,* and J. J. Barton*

The band dispersion of the localized, fluorine 2p-like valence band of LiF was mapped using an imaging technique to obtain $k(E)$. The bandwidth is 3.5 eV (from G_{15} to X'_4). This is 17% wider than predicted by local density theory, implying an expansion of the bandwidth by self-energy effects, in qualitative agreement with quasiparticle calculations. The self-energy effect is opposite to that seen in delocalized systems, such as alkali metals. Figure 1 shows the experimental momentum distribution obtained from an epitaxial overlayer of LiF grown on a clean Ge(100) crystal face.

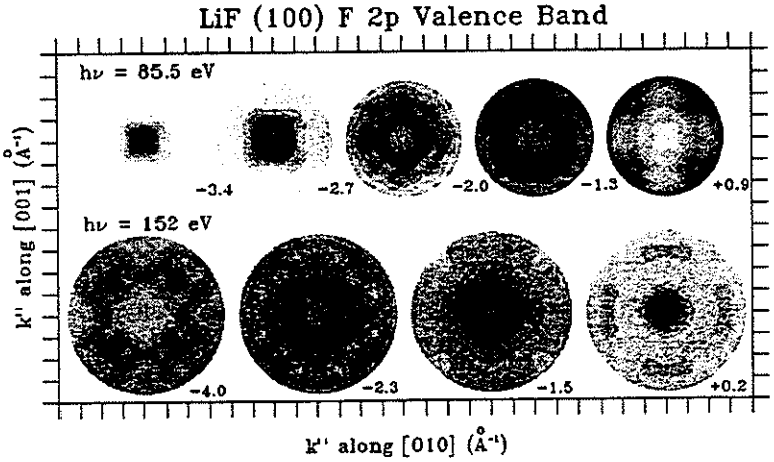

Figure 1. Momentum distributions of photoelectrons from the fluorine 2p valence band of LiF(100) at various electrons energies relative to the valence band maximum. The two photon energies relative to the valence band maximum (G_{15}) and minimum (X'_4) appear in normal emission, respectively. The pictures are centered around the surface normal. Areas of high emission intensity appear dark.

* IBM

From this unique method of measuring the complete momentum distribution of the deep, fluorine 2p-like band in this material, more-accurate bandwidths and dispersions can be obtained in other localized electron systems, such as high-temperature superconductors. In the future, the correlation between experiment and theory can then be used to aid in validating computational methods for calculating the self-energy of quasiparticles and bulk systems.

High-Resolution Photoabsorption on Beamline 8-2 at SSRL

L. J. Terminello, G. D. Waddill, and J. G. Tobin

The nitrogen, carbon, and oxygen 1s photoabsorption of O_2, N_2, and CO gas was measured on the bending magnet beamline at the Stanford Synchrotron Radiation Laboratory (SSRL). The resolving power at the nitrogen 1s edge ranges from 8 to 12.5×10^3 based on the vibrationally-resolved 1s $\rightarrow$ p* transition. This indicates that this spherical grating monochromator is one of the highest-resolution monochromatic soft x-ray (SXR)/VUV photon sources yet reported. The relationship of slit opening vs resolution at 400 eV photon energy is shown in the inset of Fig. 2.

Remaining FY 92 Plan:

- Complete the bond-characterization study of amorphous boron nitride using boron and nitrogen 1s photoabsorption. Currently, the hexagonal and cubic phases have been measured with VUV absorption.
- Perform photoabsorption measurements on rare-earth orthophosphates as model compounds for actinide long-term storage media. By measuring the VUV photoabsorption, we can investigate the utility of these materials as excitonic lasing compounds.

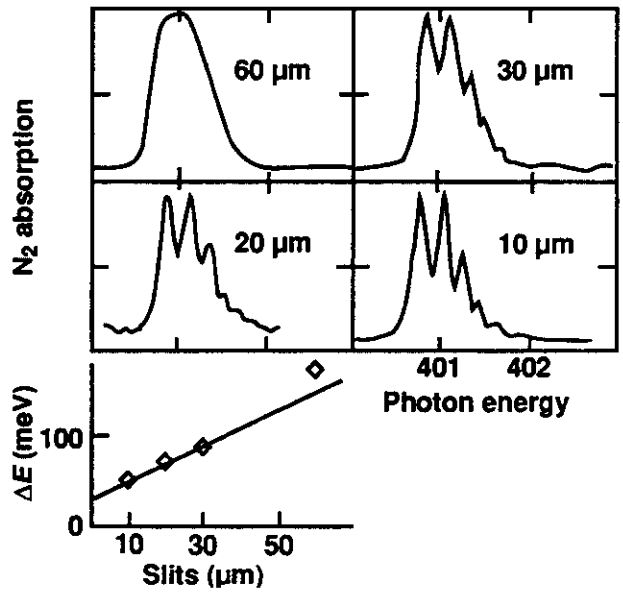

Figure 2. Photon energy resolution at 400 eV as a function of entrance and exit slit aperture. The top four panels are the raw N_2 1s→p* photoabsorption spectra taken with slit openings indicated (entrance aperture equals exit). Photon energy resolution as a function of slit opening is shown in the bottom panel (open diamonds are data, solid line is linear fit).

YB_{66} Reflectivity and Resolution Measurements

J. Wong, F. Schaefers,* B. Muller,* T. Tanaka,† and Y. Kamimura,†

Reflectivity and resolution data have been obtained in the energy region between 1 and 2 keV using a double crystal monochromator beamline at the Berlin Synchrotron Laboratory (BESSY). The results are plotted in Fig. 3. A direct comparison with similar measurements on a beryl crystal (open diamonds), however, shows that the resolution is nearly a factor of 2 better than that of beryl (bottom plot). A laboratory measurement using magnesium K_α radiation (open circle at 1254 eV) is in good agreement with the synchrotron data. The result of an energy scan at fixed Bragg angle (open square at 1400 eV) gives an identical result. The reflectivity (upper plot) is structureless, with a broad plateau between 1.3 and 1.7 keV. As mentioned in earlier reports, resolution and reflectivity are a smooth function of energy, while those of beryl have absorption structures near the aluminum and silicon K edges.

Remaining FY 92 Plan:

- Set up a double YB_{66} crystal monochromator and measure EXAFS scans of magnesium, aluminum, silicon, and phosphorous at BESSY.
- Continue collaboration with Tanaka to grow more perfect single crystals of YB_{66}.

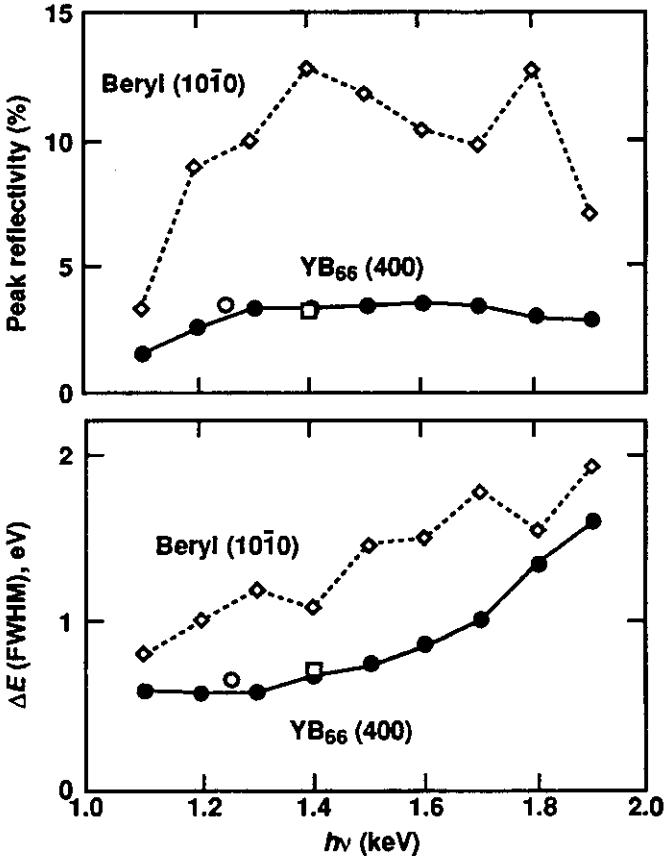

Figure 3. Reflectivity and resolution data for the YB_{66} crystal in comparison with beryl.

* Berlin Synchrotron Laboratory (BESSY)

† Japan

Cr^{3+} Site-Specific Chemistry and Crystal Structure of $LiCaCrF_6$

B. Rupp, W.L. Kway, J. Wong, P. Rogl* and P. Fischer†

The crystal structure of $LiCaCrF_6$, a fully chromium-substituted lithium-metal hexafluoride representative for laser materials of the generic formula $LiM^{II}M^{III}CrF_6$ (M^{II} = Ca, Sr; M^{III} = Al) was determined by x-ray single crystal diffraction and neutron powder profile refinement. $LiCaCrF_6$ was confirmed as a Colquiirite type structure (space group P31c, $z = 2$, $a = 5.1054(08)$ Å, $c = 9.7786(10)$ Å (see Fig. 4). Lithium in 2c, calcium in 2b, chromium in 2d and fluorine in 12i positions with x,y,z of 3652(3), 0183(4), 1402(1). Deviation from centrosymmetry and full occupation appear to be insignificant. We selected $LiCaCrF_6$ as a model compound to determine the site-specific information in 3% chromium-doped $LiCaAlF_6$ laser crystals where chromium occupies a slightly distorted CrF_6 octahedron with a Cr-F distance (1.898 Å) identical to Cr-F in $LiCaCrF_6$ (1.901 Å) and CrF_3(1.899 Å). The pseudo-binary laser materials $LiSrAl_{1-x}Cr_xF_6$ forms a true solid solution over the complete composition range $0 \leq x \leq 1$.

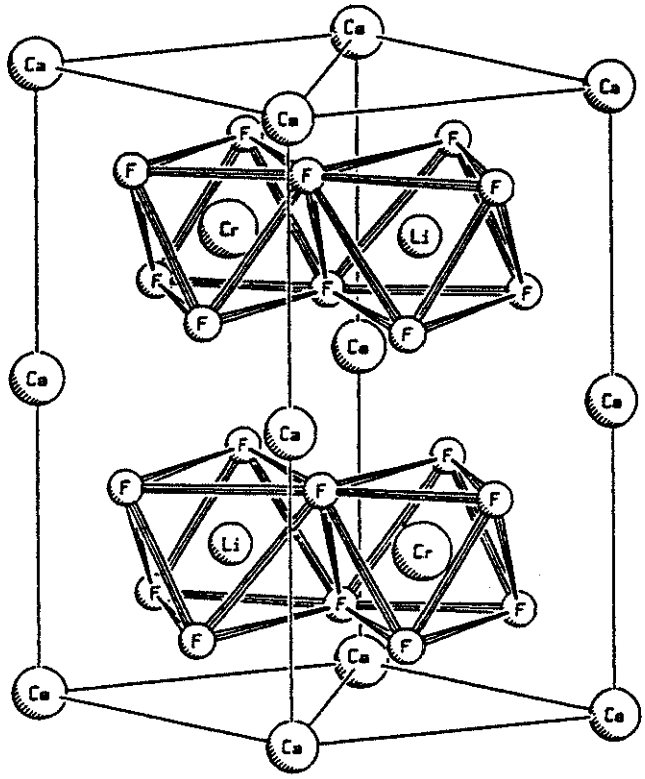

Figure 4 Crystal structure of $LiCaCrF_6$ depicted as a network of MeF_6 octahedra with a varying degree of distortion. The CaF_6 octahedral network is omitted to better emphasize the larger LiF_6 and smaller CrF_6 octahedra.

* Vienna University
† ETH, Switzerland

Compact Diffractometer-Infrared Pyrometer System for *In Situ* Chemical Dynamics Studies of High-Temperature Solid-State Reactions

J. Wong, P. A. Waide, G. Nutt, and E. M. Larson*

This is a second-generation device. The components are shown schematically in Fig. 5. The x-ray detector is mounted on the chamber so as to cover a 30° span of 2θ space centered at 40° in 2θ. With this design, the detector can record most of the high-intensity diffraction lines for a large variety of crystalline substances to facilitate phase identification in the course of chemical reactions. The placement and orientation of the infrared optics path allows the pyrometer to record synchronously the surface temperature at the diffraction region of the sample in a conventional video imaging mode at 30 frames per second, or as an infrared streak camera at 8000 lines per second. In the latter mode, it records intensities as a function of x and time. Only a single video line across the sample is measured, but the measurements are performed at a much higher rate.

Figure 6 shows the time-resolved diffraction data for the Zr + C → ZrC reaction. Each diffraction scan was recorded in 100 ms. At t = 0, the pressed powder sample of zirconium and graphite was ignited by the tungsten coil, and the detector was triggered to record the diffraction patterns of the zirconium metal and graphite reactants at room temperature. At t = 2 s, the combustion front entered the sample area illuminated by the synchrotron beam. Heating of the zirconium metal was detected by a drop in intensity of the major Zr(101) line due to thermal broadening (the Debye-Waller effect). In the next frame at t = 2.1 s, all the reactant lines show a decrease in intensity, and ZrC product lines begin to emerge. At t = 2.2 s, the reactant lines have disappeared and the product lines have grown to full strength. From t = 2.3 s onward, both ZrC lines shifted to higher 2θ values, denoting lower interatomic spacings and hence lattice contraction due to sample cooling.

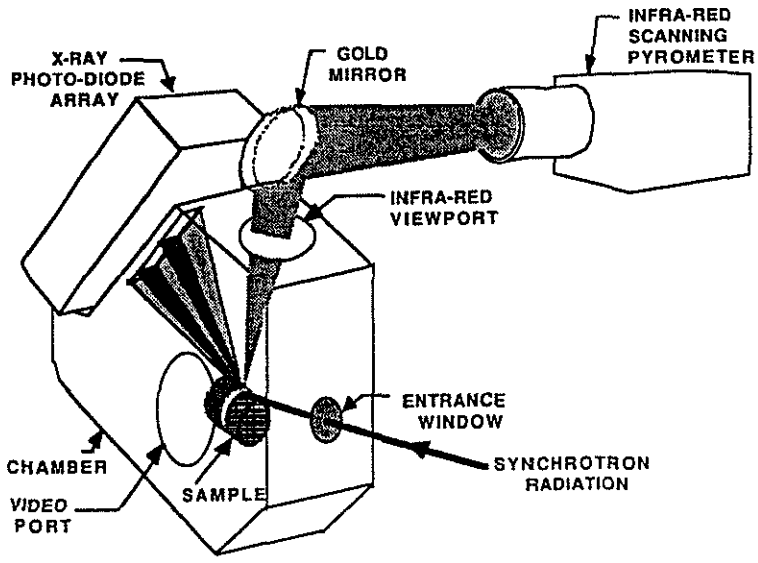

Figure 5. Schematic of the compact TR-diffractometer IR pyrometer system.

* Arizona State University

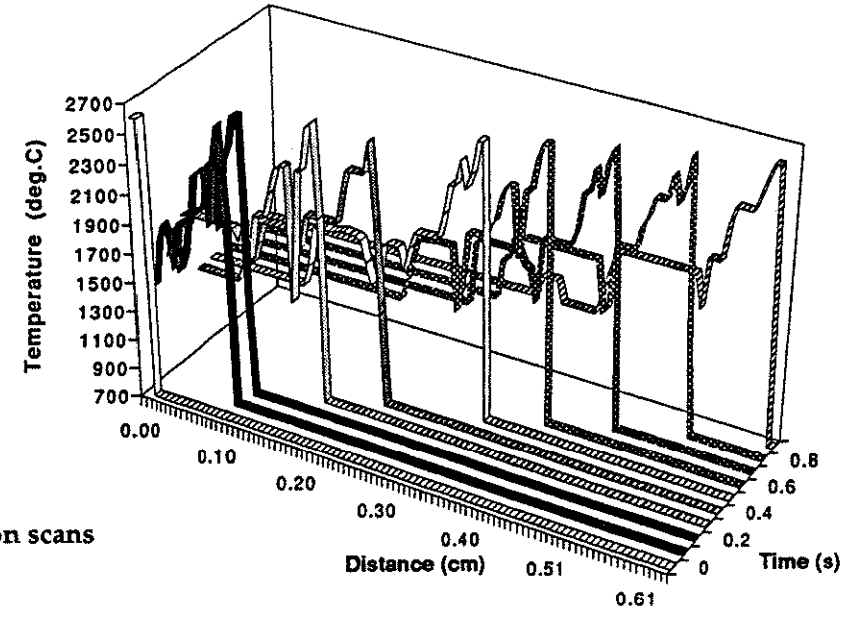

Figure 6. Selected TR-diffraction scans for the Zr + C → ZrC reaction.

Figure 7 shows a series of temperature profiles of the combustion front plotted at 100-ms intervals during its passage through the x-ray diffraction region of a reacting Zr + C sample. These profiles were recorded in the streak mode at 8000 sweeps per second. The combined time-resolved diffraction and thermal data will permit chemical dynamics of the system to be evaluated as a function of their thermal history in real space and time.

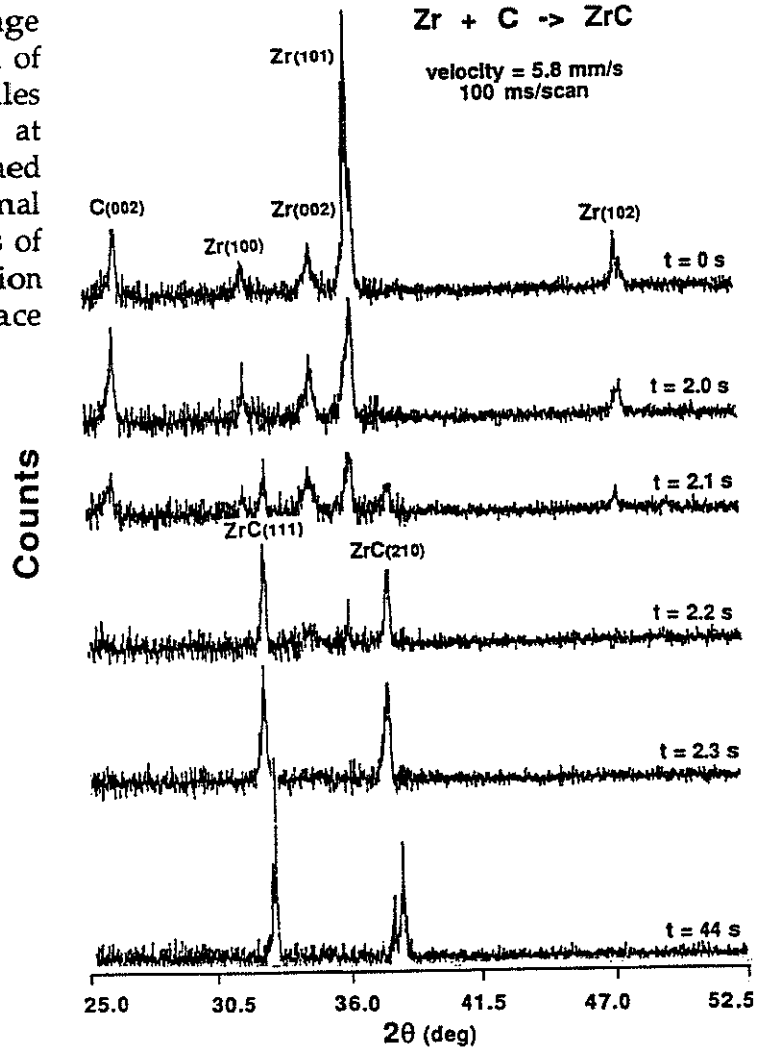

Figure 7. Temporal-spatial temperature profiles in the area illuminated by the synchrotron beam during passage of the combustion front in the Zr + C → ZrC reaction.

Remaining FY 92 Plan:

- Complete analysis of our 12/91 TRXRD data on the M + C → MC and M + 2B → MB_2 reactions, where M = Zr, Nb, Hf and Ta.
- Model the above metal carbide synthesis reactions using the quantitative data from our TRXRD to follow the course of chemical dynamics at the reaction front.

Critical Assessment of the QEXAFS (Quick-Scanning EXAFS) Method

J. Wong, R. Frahm,* and P.A. Waide

The key instrumentation in an QEXAFS setup is the employment of microstepper to provide a high motor step number per Bragg degree. The experimental parameters for this technique are as follows: given a hardware setup of 80,000 steps/Bragg deg, θ_i = Bragg angle of initial energy (deg), θ_f = Bragg angle of final energy (deg), **r** = scan rate, (steps/s), and **c** = counting time per data point (s/point), then t_Q, time of a QEXAFS scan (s) = $(\theta_i - \theta_f) \times 80000/r$ and **N**, the number of data points, t_Q/c. A full EXAFS scan of a titanium foil over 1100 eV can now be recorded in 13 s (using a scan rate of 14,000 steps/s and count time of 0.02 s/point with no spectral distortion, compared with a point-by point scan, which normally takes over 30 min). The advantages of QEXAFS are many. The measurement may be made in the transmission, fluorescence, e-yield, or glancing-angle modes. Samples may be in bulk, dilute, powder, thin film, and surface. Such an QEXAFS setup is a one-time installation and may be turned on and off by software. Applications of QEXAFS include survey scans for optimization, taking "normal" EXAFS spectra and time-resolved studies on the order of seconds.

Remaining FY 92 Plan:

- With Ron Frahm, LLNL visiting guest, we plan to implement the QEXAFS capability on beamline 10-2 at SSRL in our April 1992 run and perform a series of time-resolved EXAFS studies on high-temperature solid reactions.
- From 6/15 to 11/15, 1992, Wong plans to return to HASYLAB to complete part II of his Humboldt award. Specifically, he will evaluate a yet faster QEXAFS mode employing a piezoelectric drive with a view to achieve subsecond time resolution.

Publications and Presentations

Published

1. J. G. Tobin, C. G. Olson, C. Gu, J. Z. Liu, F. R. Solal, M. J. Fluss, R. H. Howell, J. C. O'Brien, H. B. Radousky, and P. A. Sterne, "Valence Bands and Fermi-Surface Topology of Untwinned Single-Crystal $YBa_2Cu_3O_{6.9}$," *Phys. Rev. B* **45**, 5563 (1992).
2. C. G. Olson, J. G. Tobin, F. R. Solal, C. Gu, J. Z. Liu, M. J. Fluss, R. H. Howell, J. C. O'Brien, H. B. Radousky, and P. A. Sterne, "High Resolution Photoemission Studies of Untwinned $YBa_2Cu_3O_{6.9}$," *J. Phys. Chem. Solids* **52**, 1419 (1991).

* HASYLAB

3. J. G. Tobin, C. G. Olson, F. R. Solal, C. Gu, J. Z. Liu, and M. J. Fluss, "The Acute Spectral Structure of Single-Domain $YBa_2Cu_3O_{6.9}$," in "High Temperature Superconductivity: Physical Properties, Microscopic Theory and Mechanisms," J. Ashkenazi, S. E. Barnes, F. Zuo, G. C. Vezzoli, and B. M. Klein, Eds. (Plenum, 1992).
4. L. J. Terminello, D. K. Shuh, F. J. Himpsel, D. A. Lapiano-Smith, J. Stohr, D. S. Bethune, G. Meijer, "Unfilled Orbitals of C_{60} and C_{70} from Carbon K-Shell X-Ray Absorption Fine Structure," *Chem. Phys. Lett.* **182**, 491 (1991).
5. D. A. Lapiano-Smith, E. A. Eklund, F. J. Himpsel, and L. J. Terminello, "Epitaxy of LiF on Ge(001)," *Appl. Phys. Lett.* **59**, 2174 (1991).
6. B. Rupp, B. Smith, and J. Wong, "SEXIE for Calculating Coordination Shells and Geometries," *Comp. Phys. Comm.* **67**, 543 (1992).
7. E. M. Larson, A. J. G. Ellison. F. W. Lytle, A. Navrosky, R. B. Greegor, and J. Wong, "XANES Study of La in the Potassium Silicate Glass System," in *X-Ray Absorption Fine Structure* , S. S. Hasnain, Ed. (Ellis Horwood Publishers, 1991), p. 326.
8. J. Wong, W. E. Nixon, J. W. Mitchell, and S. Laderman, "Solute Pairing in Solution-Hardened fcc Cu-Alloys," *J. Appl. Phys.* **71**, 150 (1992).
9. J. Wong, E. M. Larson, J. B. Holt, P. A. Waide, B. Rupp, R. Frahm, and G. Nutt, "Time-Resolved Diffraction Studies of Fast Solid Combustions at High Temperature," in *Proc. Conf. Synch. Radiation and Dynamic Phenomena*, Grenoble, France (1991).
10. R. Frahm, J. Wong, J. B. Holt, E. M. Larson, B. Rupp, and P. A. Waide, "Solid Combustion Reactions Characterized by Time-Resolved XAS," *Proc. Conf. Synch. Radiation and Dynamic Phenomena*, Grenoble, France (1991).
11. F. Schaefers, B. R. Muller, J. Wong, T. Tanaka, and Y. Kamimura, "YB_{66}: A New Soft X-Ray Monochromator Crystal," *Synch. Radiat. News*, April (1992).
12. J. G. Tobin, V. L. Colvin, and A. P. Alivisatos, "Compound Semiconductor Nanocrystalline Clusters," *Energy and Technology Review*, UCRL-53000-91-7·8 (1991), p. 86.

In Press/Accepted/Submitted

1. L. J. Terminello, G. D. Waddill, and J. G. Tobin, "High Resolution Photoabsorption and Circular Polarization Measurements on the University of California/National Laboratory Spherical Grating Monochromator Beamline," *Nucl. Instrum. Methods*, July/August 1992.
2. A. Santoni, M. Ronay, L. J. Terminello, G. V. Chandrashenk, F. J. Himpsel, and Y. Hidaka, "Charge Transfer Gap D and Fermi Level Position in $La_{2-x}Sr_xCuO_4$ and $Nd_{2-x}Ce_xCuO_4$," *Phys. Rev. B* (accepted).
3. A. Santoni, L. Sorba, D. K. Shuh, L. J. Terminello, A. Franciosi, S. Nonnarone, "Initial Stages of atomic Hydrogen Chemisorption on GaAs (110)," *ECOS Conf. Proc.* (accepted).
4. L. J. Terminello, G. D. Waddill, and J. G. Tobin, "High Resolution Photoabsorption and Circular Polarization Measurements on the University of California/National Laboratory Spherical Grating Monochromator Beamline," *Nucl. Instrum. Methods* (accepted).

5. E. M. Larson, J. B. Holt, J. Wong, P. A. Waide, B. Rupp, and L. J. Terminello, "A Time-Resolved Diffraction Study of the Ta-C Combustion System," *J. Mater. Res.* (accepted).
6. R. Frahm, J. Wong, J. B. Holt, E. M. Larson, B. Rupp, and P. A. Waide, "Real-Time Probe of Reaction Centers in Solid Combustions by QEXAFS on the Subsecond Time Scale," *Phys. Rev. B* (submitted).
7. B. Rupp, J. Wong, J. B. Holt, and P. A.Waide, "The Solid Combustion Synthesis of small $REBa_2Cu_3O_x$ samples (RE = Y, Er)," *J. Mater. Res.* (submitted).
8. B. Rupp and J. B. Holt, "The Calculation and Analysis of the Adiabatic Temperature of Solid Combustion Reactions," *J. Phys. Chem.* (submitted).
9. F. J. Himpsel, L. J. Terminello, D. A. Lapiano-Smith, E. A. Eklund, and J. J. Barton, "Band Dispersion of Localized Valence States in LiF(100)," *Phys. Rev. Lett.* (submitted).

Report

J. Wong, T. Tanaka, Z. Rek, G. Shimkaveg, and M. Eckart, "The YB_{66} Soft X-Ray Monochromator," *Energy and Technology Review*, UCRL-53000-91-10 (Oct. 1991).

Invited Presentations

1. J. G. Tobin, "The Valence Bands and Fermiology of Untwinned Single-Crystal $YBa_2Cu_3O_{6.9}$," The March Meeting of the American Physical Society, Indianapolis, IN, 1992 (*Bull. Am. Phys. Soc.* 37, 574 (1992).
2. J. G. Tobin, "Photoemission Investigation of the Valence Bands and Fermiology of Untwinned, Single-Crystal $YBa_2Cu_3O_{6.9}$," The Gordon Conference on Superconductivity, Oxnard, CA, Jan. 1992.
3. J. G. Tobin, "The Valence Bands and Fermiology of Untwinned Single Crystal of $YBa_2Cu_3O_{6.9}$," Applied Physics Seminar, Stanford, CA, Jan. 1992.
4. J. G. Tobin, et al. "A Photoemission Investigation of Nanocrystalline Quantum Dots," Chemistry Dept. Seminar, UC Davis, Sep. 1991. A second lecture, "Careers in Chemistry," was also presented.
5. L. J. Terminello, "High-Resolution Photoabsorption of O_2, N_2, and CO K-shells on the UC/National Laboratory Spherical Grating Monochromator Beamline." SSRL User's Meeting, Stanford, CA, Nov. 1991.
6. J. Wong. "Chemical Dynamics of High Temperature Solid State Reactions Using SR," Physical Chemistry Colloquium, Bochum University, Bochum, Germany, July, 1991.
7. J. Wong, "YB_{66} as a New Soft X-Ray Monochromator for SR," Materials Physics Seminar, European Synchrotron Radiation Facility (ESRF), Grenoble, France, Sept. 1991.
8. J. Wong, "Time-Resolved Synchrotron Studies of Solid Combustions," Materials Science Seminar, LURE Synchrotron Radiation Facility, Orsay, France, Oct. 1991.
9. J. Wong, "Chemical Dynamics of Solid Combustions by Time-Resolved Diffraction and XAS," Research Colloquium, Mineralogishces Institut, University of Bonn, Bonn, Germany, Oct. 1991.

10. J. Wong, "Synchrotron Studies of Solid Combustions in the Subsecond Time Scale," Materials Physics Seminar, Frascati Synchrotron Radiation Laboratory, Frascati, Italy, Nov. 1991.
11. J. Wong, "Time-Resolved Diffraction and QEXAFS Studies of Solid Combustions," HASYLAB Physics Seminar, Hamburg, Germany, Nov. 1991.
12. J. Wong, "Study of Fast Chemical Reactions Using Synchrotron Radiation," Physical Chemistry Seminar, Hamburg University, Hamburg, Germany, Nov. 1991.

Contributing Presentations

1. J. G. Tobin, C. G. Olson, C. Gu, J. Z. Liu, F. R. Solal, and M. J. Fluss, "The Valence Bands and Fermiology of Untwinned, Single-Crystal $YBa_2Cu_3O_{6.9}$," The March Meeting of the American Physical Society, Indianapolis, IN, 1992 (*Bull. Am. Phys. Soc.* 37, 120, 1992).
2. J. G. Tobin, C. G. Olson, C. Gu, J. Z. Liu, F. R. Solal, and M. J. Fluss, "The Valence Bands and Fermiology of Untwinned Single Crystal $YBa_2Cu_3O_{6.9}$," The Fall Meeting of the Materials Research Society, Boston, Massachusetts, Dec. 1991.
3. J. G. Tobin, C. G. Olson, C. Gu, J. Z. Liu, F. R. Solal, and M. J. Fluss, "The Valence Bands and Fermiology of Untwinned, Single Crystal $YBa_2Cu_3O_{6.9}$," 38th National Symposium of the AVS, Seattle, WA, Nov. 1991.
4. J. G. Tobin, L. J. Terminello, G. D. Waddill, D. P. Pappas, and S. Y. Tong, "Synchrotron Radiation Studies with High Resolution and Helical Polarization using the UC/National Laboratory SGM at SSRL," The 1991 UWSRC Users Group Meeting, Stoughton, WI, Oct. 1991.
5. L. J. Terminello, G. D. Waddill, and J. G. Tobin, "High-Resolution Photoabsorption and Magnetic Circular Dichroism Measurements on the UC/ National Laboratory SGM Beamline, 7th National Conference on Synchrotron Radiation Instrumentation '91, Baton Rouge, LA, Oct. 1991.

RD-100 Competition

P. A. Waide and J. Wong, "Compact TR-Diffractometer-Infrared Pyrometer System," *RD Magazine*, 3/92 (submitted).

Weapons-Supporting Research

Group

Atomistic Approach to the Interaction of Surfaces with the Environment: Actinide Studies

C. A. Colmenares, *Group Leader*

Overview

The interaction of "surfaces" with the "environment" may be studied by measuring the effect that adatoms (clusters to films) have on (1) the atomic and electronic structures of surfaces and (2) their reactivity and by determining how, in turn, a surface may change the adatoms. Actinide elements are particularly well suited to be used as adatoms or substrates because they have 5f electrons at the Fermi-level that may be delocalized (as is the case with uranium) and thus available for reaction, or localized (as with plutonium and neptunium) and not readily accessible. Further, these 5f electrons may be easily probed by XPS, UPS, and synchrotron radiation, and thus electronic changes induced by substrates or adatoms may be conveniently measured.

This fiscal year, we have focused our efforts on three areas that we feel are very important to actinide research:

- **Localization of 5f Electrons.** When uranium is placed in thin clusters and layers, it finds itself in a low coordinated environment, where it may gradually lose its solid-state properties to become more atomic-like, leading to the narrowing of the conduction and valence bands. For the special case of the 5f bands, which are narrow in solid bulk uranium (i.e., heavy fermion systems), an additional narrowing in surface systems could result in the complete breakdown of the 5f itinerancy. For such systems, we would observe localized 5f states, even for reduced chemical species. We are looking for this localization effect in the Pt-U, Pd-U, and Si-U systems.
- **Reactivity of Highly Diluted U on Surfaces.** We are interested in studying the chemical reactivity of highly diluted uranium on surfaces of transition metals because this concept may be used in catalysis. It has been shown[1] that uranium loses its high, early transition-metal–like reactivity when diluted in a transition-metal matrix. In such systems, reduced or partially oxidized uranium atoms may be stable in the presence of C-H-O–containing gas molecules, which is not the observed case for bulk uranium compounds. These atoms may act as promoters, not only electrostatically as with alkali metals, but also covalently using their 5f orbitals, which have been shown to play an important role in homogeneous catalysis.
- **Interfaces in Corrosion and Passivation.** Layers of uranium on transition metals constitute nonburied interfaces, which can be studied by surface spectroscopies. We are especially interested in studying the decomposition of such interfaces in the presence of reactive gases, because this is an effective way of addressing problems in corrosion and passivation of actinide surfaces.

Shortly, we expect to have a theoretician participate in this project. This would be a significant asset for interpretating results and planning future experiments.

Midyear Accomplishments

We used photoemission techniques (XPS and UPS) to study (1) the behavior of uranium thin layers on clean silicon surfaces (localization of 5f electrons) and (2) the absorption of C_2H_4 and O_2 on thin uranium layers deposited on surfaces of freshly cleaved highly oriented pyrolytic graphite (HOPG) (Catalysis).

We are now collaborating with J. Tobin and D. Waddill to carry out experiments at the Stanford Synchrotron Radiation Laboratory in the three areas defined. We have recently used resonant photoemission (RESPES) and highly surface-sensitive core-level spectroscopies to study (1) the formation of surface oxycarbide on thin layers of uranium on graphite by reaction with O_2 and CO (catalysis); (2) the surface decomposition of UFe_2 at room and elevated temperatures (corrosion of bulk intermetallics); and (3) the interaction of uranium with H_2S to form US and possibly U_xS_y (narrow-band properties and localization, quasi-localization, of 5f electrons).

XPS and UPS Studies

T. H. Gouder and C. A. Colmenares

The U-Si System—Study of Thin Layers of Uranium on Silicon

We have studied thin layers of uranium on Si(111) by XPS and UPS. Silicon was chosen because it displays a small signal background in UPS, making it easy to study small quantities of uranium on silicon by UPS. Figure 1 shows the U4f spectra of uranium deposited on silicon and the changes that take place during annealing. Satellites observed at 6 eV above the 4f lines have been interpreted as a precursor of 5f electrons localization.[2] The intensity of the satellite increases when the surface is annealed at high temperature (670 K). On the other hand, we found that annealing results in the diffusion of uranium into the bulk and, consequently, in the decrease of the uranium surface content. The increase in the intensity of the 6-eV satellite corresponds with the dilution of uranium in silicon, which should result in a narrowing of the U5f band, (i.e., approach of localization). However, valence band spectra do not clearly signify U5f localization except, perhaps, by an intensity increase between 1 and 3 eV. The use of synchrotron radiation will be most useful to clarify this point. In addition, we showed that thin layers of uranium built up a Schottky barrier on silicon as shown by a negative shift of the Si2p binding energy.

We assessed the surface reactivity of the U/Si system by studying its interaction with O_2. In contrast to most of the intermetallics we have studied (UNi_2, UNi_5, UFe_2) and to thin layers of uranium on platinum, oxygen is shared between uranium and silicon surface atoms. O_2 adsorption leads to the partial oxidation of silicon and uranium surface atoms.

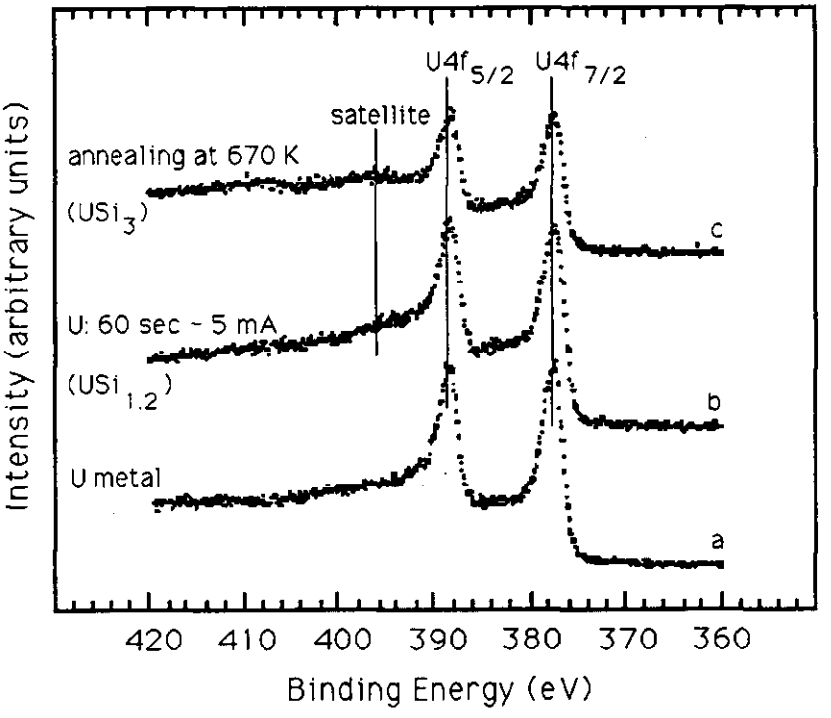

Figure 1. Spectra for U4fs: (a) bulk U metal; (b) U deposited on Si at 300 K ($USi_{1.2}$); and (c) annealing of the U/Si surface at 670 K (USi_3).

C_2H_4 and O_2 Adsorption on the U/Graphite System

UO_2 is the lowest oxidation state of a stable oxide of uranium. However, in the presence of carbon, an even lower oxide—UO—is formed as a solid solution of UO and UC, generally called uranium oxycarbide (UO_xC_{1-x}). This lower oxide is metallic, and its 5f states are delocalized.[3] In this oxide, uranium loses part of its 6d7s electrons, which are highly reactive. Therefore, the oxycarbide could be a very interesting material in catalysis because of its delocalized 5f electrons, which become available for bonding with gas molecules. We therefore wanted to compare the stabilities of the oxycarbide and the dioxide. The question we addressed was whether thin surface layers of UO_2 may be transformed into UO_xC_{1-x} when adsorbing a hydrocarbon, C_2H_4, at a moderate temperature, typically ~300°C. This would test the thermodynamic stability of UO vs UO_2. A thin layer of uranium on graphite was partially oxidized to UO_2 by adsorbing 50 L O_2 (1 Langmuir, L, = 10^{-6} Torr·s) at room temperature. This surface was annealed to 300°C for 10 minutes to find out if heating alone would lower the stoichiometry of the oxide. While this occurs on partially oxidized bulk uranium metal, the thin layer of uranium on graphite did not show this tendency, probably because there was no bulk buffer of uranium metal capable of reacting with the surface oxide layer. Annealing the surface under a hydrocarbon pressure, on the other hand, resulted in the almost complete disappearance of the UO_2 signal, which was replaced by a highly asymmetrical U4f band at and slightly above the metal emission. We attribute this emission to uranium oxycarbide. A more detailed study of the valence band at the synchrotron (see below) confirmed this interpretation. C_2H_4 interaction with the U/UO_2 surface changed the O2p emission from its asymmetrical UO_2 shape to a symmetrical one,[4] also

observed after CO adsorption, and which we attributed to the oxycarbide.[1] Moreover, the intensity at the Fermi-level was restored, agreeing with the transformation of the semiconducting UO_2 into UO-UC, which has metallic properties.

Synchrotron Radiation Studies

T. H. Gouder, C. A. Colmenares, J. G. Tobin, and G. D. Waddill

Study of U-CO and U-O_2 Interaction

In Fig. 2 we compare the U4f core-level spectra of sputtered uranium and of this metal exposed to CO and then O_2 at room temperature. We used 550-eV photons that produced 160-eV U4f photoelectrons that are more surface sensitive than photoelectrons ejected by the conventional XPS-MgKa photons (1253 eV) and that have a kinetic energy of 863 eV. Both CO and O_2 spectra represent the same oxygen coverage, as confirmed by taking the ratio of the O1s/U4f emissions. O_2 adsorption resulted in the appearance of an oxide emission at 3 eV higher binding energy (BE) than the metal line, which is characteristic for UO_2. CO adsorption, on the other hand, broadened the U4f line, and the peak became more asymmetrical, indicating an intensity increase on the high-BE side of the metal emission. The supplementary intensity does not appear as a separate oxide line as in the case of UO_2, but lies closer to the metal line. This points to uranium in a low oxidation state as in the oxycarbide, which is a solid solution of UO and UC.

Resonant photoemission was used to study the character of the O2p band, in particular the U5f contribution in this band. It was found that the O2p peak resonates less for UO_xC_{1-x} than for UO_2, when the photon energy is tuned through the 5d threshold.

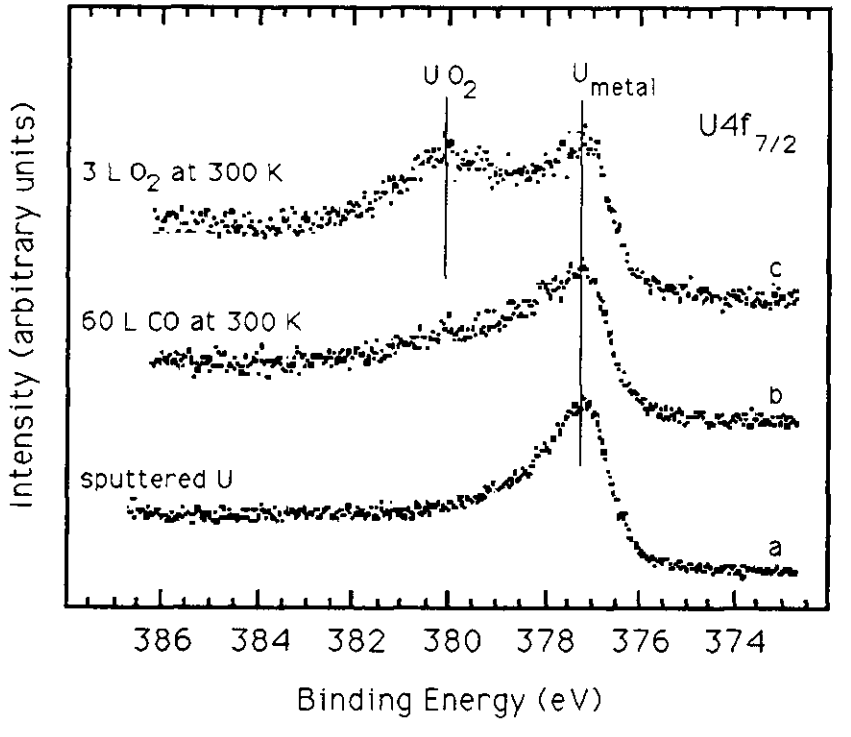

Figure 2. U4f core-level spectra of (a) sputtered U; (b) adsorption of 60 L CO at 300 K; and (c) adsorption of 3 L O_2 on sputtered U at 300 K.

This indicates a lower 5f contribution in the O2p band in the case of UO_xC_{1-x} than in UO_2 and points to the presence of UO. This agrees with our previous finding, that the general shape of the O2p band is different after O_2 and CO exposure than for O_2 alone.

Study of the Surface Decomposition of UFe_2

One question of special importance for uranium intermetallics is the stability of the surface and its reactivity at elevated temperatures under vacuum and in the presence of reactive gases. This type of study gives information on the corrosion mechanism of intermetallic surfaces and allows us to separate the role of thermal effects and adsorbates on surface decomposition.

We studied UFe_2 by resonant photoemission and surface-sensitive core-level spectroscopies. The spectrum of sputtered UFe_2 in resonance shows a broad emission at the Fermi-level, broader than in uranium metal, which is due to the superposition of the Fe3d and U5f valence states. Out of resonance, it becomes even broader because the emission from the 5f states, which are very narrow and located immediately at the Fermi-level, is suppressed while the broader Fe3d emission still remains. Annealing the UFe_2 surface at 300°C results in the narrowing of the valence band in resonance, pointing to a higher contribution of the narrow U5f states to the spectrum. Out of resonance, the emission around E_F is strongly suppressed because there are fewer non-resonating Fe3d states. This finding agrees with the results from core-level spectroscopies showing that annealing alone results in the surface segregation of uranium, which may be attributed to the lower surface energy of uranium than that of iron. O_2 adsorption of 10L O_2 at room temperature produces supplementary surface segregation of uranium. Temperature-induced surface segregation does not take place, the emission at the Fermi-level completely disappears, and the spectrum looks like that of pure UO_2. Core-level spectroscopy, on the other hand, shows that iron is still unoxidized. Therefore, we conclude that the valence-band spectra no longer contain any iron information at all and that this is due to the surface segregation and oxidation of uranium.

Resonant Photoemission Study of H_2S Adsorption on Uranium

We used H_2S to synthesize, *in situ*, uranium sulfide on the surface of a uranium coupon. Figure 3 compares uranium metal before and after H_2S adsorption at room temperature and at 300°C. At this temperature, H_2S adsorption leads to the appearance of three additional peaks at 2.0, 3.5, and 6.0 eV. The feature at 2.0 eV resonates strongly, pointing to its U5f nature, while the two others do not. The emission at 6 eV is probably due to a slight oxygen contamination, which was verified by the presence of an oxygen O1s signal in core level spectroscopy. Oxygen contamination would also account for the 2-eV signal, which is attributed to the localized $U5f^2$. The signal at 3 eV is assigned to the S3p band. At high temperature, the S3p shifts to higher BE by 4 eV, where it is also found in bulk US,[5] suggesting that at room temperature we are forming a surface phase of different stoichiometry than US. The 2-eV emission decreases in intensity. A most interesting feature was observed on a high-resolution scan of the Fermi-level emission (Fig. 4). H_2S adsorption at room temperature led to the appearance of a peak at 0.6 eV BE, observed neither on sputtered uranium nor for the high-temperature adsorption of

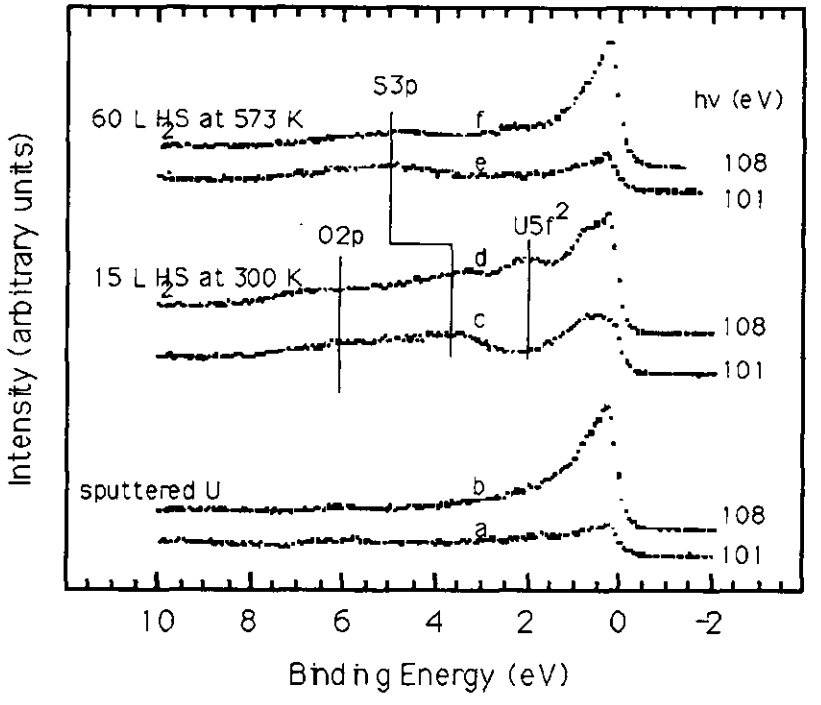

Figure 3. Valence-band spectra of sputtered U: (a) out of resonance; (b) in resonance. Adsorption of 15 L H_2S at 300 K: (c) out of resonance; (d) in resonance. Adsorption of 60 L H_2S at 573 K; (e) out of resonance; and (f) in resonance.

H_2S on uranium. Its strong resonance points to its 5f nature. Because this peak is not observed for UO_2, we do not think it is due to oxygen contamination. One possible explanation would be the quasi-localized $U5f^3$ configuration also observed in USb.[6] This configuration could easily be produced at room temperature by a higher stoichiometric sulfide, such as U_xS_y. Annealing would reduce this sulfide to US. The changes observed for the S3p valence band during heating support such an interpretation. Further work has to be done to further clarify this point.

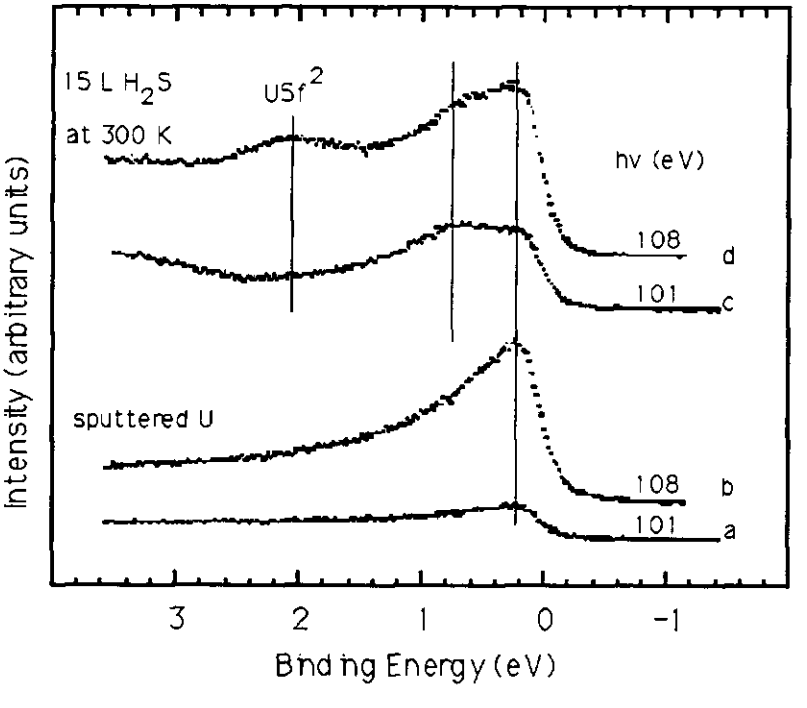

Figure 4. High-resolution valence-band spectra of sputtered U: (a) out of resonance; (b) in resonance. U after 15L H_2S exposure: (c) out of resonance; and (d) in resonance.

References, Publications, and Presentations

References

1. T. Gouder, C. Colmenares, J. R. Naegele, and J. Verbist, *Surf. Sci.*, in press (1992).
2. C. Laubschadt, W. Grentz, and G. Kaindl, *Phys. Rev. B* **37**, 8082 (1988).
3. T. Gouder, C. Colmenares, J. R. Naegele, and J. Verbist, *Surf. Sci.* **235**, 280 (1990).
4. M. S. S. Brooks, B. Johansson, and H. L. Skriver, in *Handbook on the Physics and Chemistry of the Actinides*, A. J. Freeman and G. H. Lander, Eds. (Elsevier Science Publishers, New York, 1984), Vol. 1, p. 153.
5. Y. Baer, *Physica* **102B**, 104 (1980).
6. B. Reihl, N. Martensson, D. E. Eastman, A. J. Arko, and O. Vogt, *Phys. Rev. B* 26, 1842 (1982).

Publications

1. T. Gouder, C. A. Colmenares, J. R. Naegele, J. C. Spirlet, and J. Verbist, "A Surface Spectroscopy Study of the Oxidation Properties of UNi_2 and UNi_5," *Surf. Sci.* **265**, 175 (1992).
2. T. Gouder, C. A. Colmenares, J. R. Naegele, J. C. Spirlet, and J. Verbist, "Study of CO Adsorption on U, UNi_2, and UNi_5," *Surf. Sci.* (in press).
3. T. Gouder and C. A. Colmenares, "Thin Layers of Uranium on Polycrystalline Platinum. A Surface Spectroscopy Study," to be submitted for publication (1992).

Presentations

1. C. Colmenares and T. Gouder, "Formation and Interconversion of Uranium Surface Oxides and Oxycarbides Studied by UPS, XPS, and Synchrotron Radiation." 27th JOWOG-12 and 12th SUBWOG-12B Meeting, LLNL, May 18–22, 1992.
2. C. Colmenares and T. Gouder, "Thin Layers of Uranium on Polycrystalline Platinum. A Surface Spectroscopic Study." 27th JOWOG-12 and 12th SUBWOG-12B Meeting, LLNL, May 18–22, 1992.

Weapons-Supporting Research

Individual Projects

Properties of Carbon Fibers

R. M. Christensen

Overview

Research has continued on the properties of carbon fibers and related topics in materials science. The explicit work on the mechanical properties of carbon fibers as a function of various symmetry forms is now about two-thirds completed. Only one major problem remains to be solved—to complete the characterization. In somewhat related work, motivated by "Bucky Balls," the properties characterization has been found for a monolayer of carbon atoms in a cylindrical configuration. This atomic-scale fiber appears to have very special properties. Work is now progressing on determining the viscous flow properties for fiber suspensions. The results are expected to be useful for application to processing operations involved in manufacturing. Finally, work has been completed on the theoretical determination of maximum compressive strength for highly anisotropic materials. The results will have application to fiber composites. This work is reported in detail in the following description because it was completed during the present reporting period.

Description

It can be quite easy to confuse evidence of material failure with that of structural failure. The term "failure" is interpreted broadly as including the loss of stability, but it is not necessarily being limited to that. Even the term "structure" is misleading. It is often associated with bodies of large characteristic dimensions, when in fact there should be no such restriction. Microsized test specimens are actually structures, with boundary conditions that influence behavior. For example, structural stability can depend on relative dimensions, independent of absolute dimensions, thus laboratory specimens can experience an instability which can be misread as material failure. Certainly, one effect can mask the other.

First, consider compressive failure through instability for fiber composites. This can be viewed as intrinsic material behavior, without regard to specimen shape or size. Nearly all the previous analyses were framed in one-dimensional form as beams on elastic foundations, or at most as a two-dimensional problem. Exceptions to this were some three-dimensional elasticity solutions, but those works were restricted to a single fiber in an elastic medium, whereas interest here is in the concentrated case of closely packed fibers, corresponding to actual usage. Furthermore, with explicit interest in fiber composites, it is necessary to have an analysis compatible with concentrated 3-D conditions because 2-D models are only qualitatively applicable to fiber composites. Accordingly, a new and different approach has been developed to predict the theoretical compressive strength of fiber composites, as controlled by an instability mechanism. This is the so-called material instability or theoretical strength. It is important to understand the theoretical basis, as a source of knowledge, with many uses such as providing a gauge of actual material performance.

It must be acknowledged that these are highly idealized analyses. Conditions of perfect geometry, in the form of alignment and tolerances etc., are assumed. It is well known that theoretical estimates of instability can be very high, as much as by factors of 3 or 4. Accordingly, one cannot expect these results to be used for predicting the absolute values for loads at failure. However, since both the present material instability analysis and commonly used structural instability analysis have comparable degrees of idealization, their use herein in only a relative sense may be quite appropriate for optimization problems. It should be noted that there are many other mechanisms of failure besides the instability types considered here. Some, such as kink-band formation accounting for fiber misalignment, may provide even more limiting conditions than the forms covered here, at least in certain applications. The present instability analyses are of an elastic type, whereas kink-band formation inherently involves irreversible deformation through damage or failure.

The theoretical compressive strength for a highly anisotropic material is derived directly from the equilibrium equations. When specialized to fiber composites, the elastic analysis reveals a bifurcation at a critical stress level different from those derived previously. The explicit result is

$$\sigma_c = -\mu_L \ ,$$

where μ_L is the longitudinal shear modulus for the fiber composite. The result has generality beyond that of fiber composites. It appears to be applicable to all material forms having hexagonal or higher symmetry forms along with a high degree of anisotropy.

The theoretical result is used in application to the problem of an axially loaded thin cylindrical shell of laminated composite material. In effect, the material instability competes with the structural instability of the shell as a whole to determine the limiting load condition. An optimal configuration, which balances the two types of instabilities, is found for the lamina orientations.

The work has been reported in UCRL-JC-109381, *The Competition Between Material Instability and Structure/Specimen Instability*, and it has been submitted for publication.

Publications/Presentations

Publications

1. R. M. Christensen, H. Schantz, and J. Shapiro, "On the Range of Validity of the Mori-Tanaka Method," *J. Mech. Phys. Solids*, **40**, 69 (1992).
2. R. M. Christensen and S. J. DeTeresa, "Elimination/Minimization of Edge-Induced Stress Singularities in Fiber Composite Laminates," *Int. J. Solids Struct.*, **29**, 1221 (1992).

Seminar

"Edge Effects in Fiber Composite Laminates," Materials Science Department, U.C. Berkeley, February 1992.

Buried Layer Formation Using Ion Implantation

R. S. Daley and R. G. Musket

Overview

Through ion implantation, otherwise insoluble elements can be introduced into a host material at concentrations that should support the formation of a buried elemental layer. At least two criteria are required for elemental layer formation[1,2]: (1) the absence of intermediate phases and (2) low mutual solubility. A third criteria, diffusion of the host material along interphase boundaries, may also be required.[3] Under the proper conditions, an elemental layer may be formed through precipitate coalescence. The processes controlling the formation of an internal layer of a pure material that excludes the elements of the host material are poorly understood.

A detailed investigation of the precipitate coalescence process is needed to further expand on the criteria for layer formation and to define the types of material systems that will fulfill these criteria. In addition, the technological applications of the layered materials has yet to be explored. Therefore, we are studying the formation of aluminum layers in silicon [i.e., Si(Al)] and silicon layers in aluminum [i.e., Al(Si)]. The interchange of host and guest material will allow us to assess the importance of diffusion at the interphase boundary and in the layer phase as conditions for layer formation. The primary goals of this research are to (1) show layer formation is possible with this binary system, (2) enhance our understanding of the precipitate coalescence process, and (3) synthesize a new material for possible use in the semiconductor industry.

Previously, 200-keV Al^+ into Si(111) and Si(100) were implanted at a temperature of 375°C. This temperature was chosen to avoid amorphization of the silicon during the high-dose implantations. Doses of 0.5, 1.0, 1.5, and 2.0×10^{18} Al/cm^2 into Si(111) substrates and 0.4, 0.9, and 1.4×10^{18} Al/cm^2 into Si(100) substrates were used to examine the dependence of layer formation on the dose process. Auger electron spectroscopy (AES) results determined peak aluminum concentrations of 42, 66, 81, and 87 at.% for the Si(111) doses, respectively. Post-implant anneals at 500°C for 1 hr were performed to enhance the probability of layer formation. Annealing to 500°C showed no change in peak aluminum concentration.

Results

Only minor scientific progress was made prior to the arrival of R. S. Daley on 3/2/92. All of the progress reported below occurred after that date.

All implanted samples, before and after any annealing, were analyzed using Rutherford backscattering spectroscopy (RBS) and particle-induced x-ray emission (PIXE). RBS provided a fast method for monitoring changes in the aluminum concentration profile

as a function of experimental conditions. Post-implant anneals just below the Al-Si eutectic (577°C) and above the melting point of pure aluminum (660°C) were also performed to observe the effects of high-temperature anneals on layer formation. The one sample that showed the possibility of having a 100-at.% aluminum layer was analyzed with the technique of nuclear reaction analysis (NRA) to extract an accurate aluminum concentration profile as a function of sample depth.

The RBS spectra from the as-implanted samples contained features that were indicative of a buried aluminum-rich layer in silicon. Because of the similarities in mass between aluminum and silicon, the RBS spectra could not be analyzed with enough detail to extract an accurate aluminum concentration profile. However, the spectra showed a dependence on dose that correlated with the AES results. After the samples were annealed to 500°C for 1 hr, the RBS showed that the aluminum profile within the silicon remained essentially unchanged, consistent with the AES results. Higher-temperature anneals, 550°C for 8 hr and 680°C for 1 hr, were then undertaken to possibly enhance layer formation. RBS from these samples were essentially featureless, indicating that significant diffusion of aluminum occurred throughout the near-surface region of the silicon with the migration of aluminum toward the silicon surface. Annealing to these high temperatures completely destroyed the buried aluminum profile, dispersing the aluminum throughout the silicon. This effect was not expected for the subeutectic anneal because the entire Si(Al) system should have remained in the solid state; perhaps the temperature exceeded 550°C for part of the anneal time.

A more detailed computer analysis of the RBS spectra for the highest dose (2.0×10^{18} Al/cm^2) of aluminum in Si(111) (500°C anneal) indicated that formation of a 100-at.% aluminum layer may have occurred. To verify this, a depth profile of the aluminum concentration using NRA was performed. The depth profile obtained is shown in Fig. 1. The relative aluminum concentration is essentially zero until a depth of ~800 Å. This is followed by an increase until a depth of ~2800 Å, where a plateau region is reached. This plateau is maintained for a thickness of ~1000 Å before a continual decrease in aluminum concentration with increasing depth is observed. To determine the aluminum concentration in the plateau region with a statistical accuracy of ±3%, the experiment was repeated using longer counting times. The result is a peak aluminum concentration within the plateau region of 80 at.%.

Summary

The results to date show that the formation of a 100-at.% aluminum layer in silicon is a complex phenomenon, dependent on several experimental parameters. The highest aluminum dose shows the formation of a 1000-Å-thick, 80-at.% aluminum layer, 2800 Å below the silicon surface. These results are encouraging in that the Be(Al) system yielded similar results for elevated temperature implants. We are therefore proceeding to implant the aluminum into room-temperature silicon substrates; this procedure was successful in yielding thick 100-at.% layers of aluminum in beryllium after annealing.

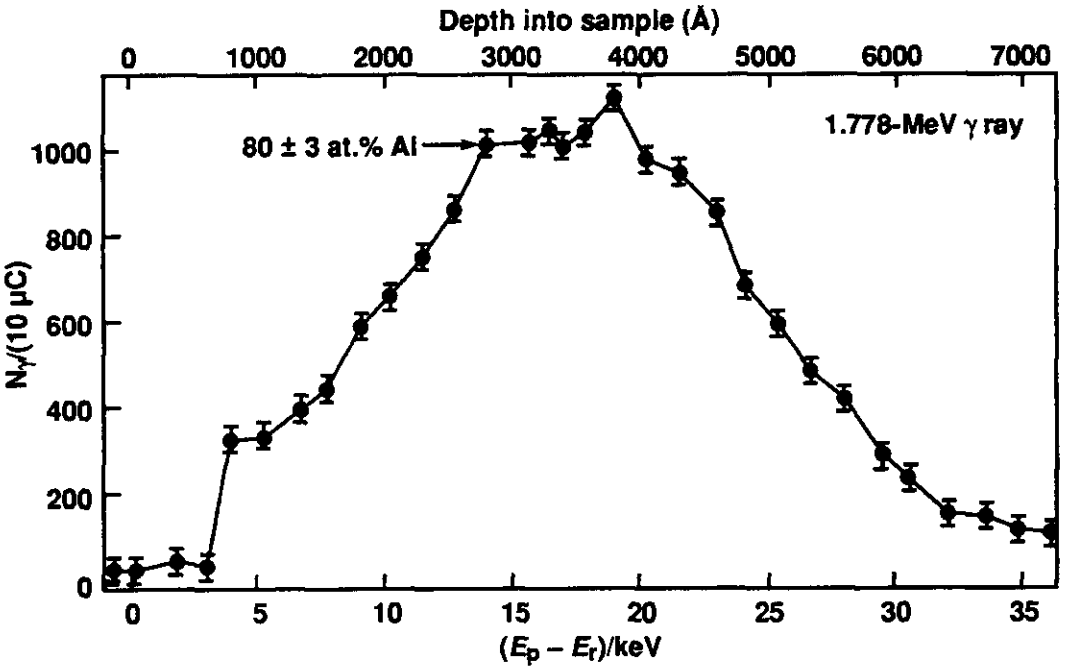

Figure 1. Nuclear reaction analysis concentration profile of aluminum buried into Si(111). Dose of 2×10^{18} Al/cm^2 with a post-implant anneal of 500°C for 1 hr. The $^{27}Al(p,\gamma)^{28}$silicon nuclear reaction at 992 keV proton energy was used. The aluminum concentration is proportional to the emitted γ-ray intensity (ordinate). The incident proton beam energy above the resonance energy (bottom abscissa) can be converted directly into a sample depth (top abscissa) to extract a concentration-vs-depth profile. The concentration in the plateau region was measured to be 80±3 at.% aluminum by comparison with γ-ray yields from pure aluminum standards.

References

1. D. W. Brown, R. G. Musket, and Z. A. Munir, "Formation of a Nearly Pure Aluminum Layer in Beryllium using Ion Implantation," *Appl. Phys. Lett.* **54**, 326 (1989).
2. D. W. Brown, R. G. Musket, and Z. A. Munir, "Buried Monocrystalline Aluminum Layers in Beryllium using Ion Implantation," *Appl. Phys. Lett.* **57**, 2651 (1990).
3. D. W. Brown, Z. A. Munir, and R. G. Musket, "A Precipitate Coarsening Mechanism for Buried Layer Formation," *Nucl. Instrum. Methods* **B59/60**, 627 (1991).

Publications and Presentations

1. R. G. Musket, R. A. Hawley-Fedder and W. L. Bell, "Proton Irradiation of Thin Films of C_{60} Molecules," *Radiat. Effects Defects Solids*, **118**, 225 (1991).
2. R.G. Musket, R.A. Hawley-Fedder, and W. L. Bell, "Interactions of Protons with Thin Films of C_{60} Molecules," oral presentation at the Materials Research Society Meeting, Boston, MA, December 1991.

Active Coherent Control of Chemical Reaction Dynamics

W. E. Conaway and S. W. Allendorf

Overview

Selective bond-breaking in molecular systems involves careful control of the reaction dynamics through carefully tailored optical excitation schemes. *Passive control* relies on the peculiarities of the potential energy surfaces and the dynamics of the particular molecule of interest. Our previous work in optically pumping localized vibrational overtones coupled with threshold photodissociation is one such example. A more general excitation technique has been suggested for the *active control* of a chemical reaction. This does not rely on the vagaries of the molecule, but on the externally controllable specifics of the excitation process itself. We have proposed to demonstrate this technique in system with multiple product channels. We have chosen as a candidate system the coherent photodissociation of water vapor.

It is possible to create two distinct excitation pathways connecting the same final photodissociative state and initial state. Coherent excitation of the molecule simultaneously along both pathways creates a final state that is a superposition state for the two pathways. This state correlates asymptotically along the dissociation coordinate to a linear combination of the possible reaction product states. By varying the relative phase and amplitude of the excitation fields, it is possible vary the quantum mechanical interference between the two excitation pathways and to alter the mix of terms in the superposition state and thus the distribution of final product states.

The two excitation pathways ideally must have the same energy and obey the same selection rules. This can most nearly be achieved when three photons of a particular wavelength are used in one excitation pathway and a single photon that is the third harmonic of the first wavelength is used for the other. This is referred to as a $1\omega,3\omega$ excitation scheme. The relative phase of the two laser fields can be controlled by passing the two beams through a pressure cell containing a gas with differing indices of refraction at the two wavelengths and by varying the pressure of the medium.

Progress

The injection-seeded Nd:YAG that was ordered with Chemistry Department capital equipment money which became available in March is due to be delivered and installed on site in mid-May 1992. The narrow bandwidth of the seeded Nd:YAG laser will be used to generate the $1\omega,3\omega$ photodissociation fields. The long coherence length will enable us to accurately control the relative phase between the two photodissociation fields.

Sarah Allendorf became available full time, as planned, starting April 1, 1992. She is concentrating on bringing the lasers, vacuum equipment, and the detection-and-control electronics that have been idle for nearly two years back into operation. The first effort will be to measure the photoacoustic absorption spectrum of $4\nu_{OH}$ HOD in the 700- to 750-nm wavelength region to identify favorable wavelengths for optically pumping the ground-state HOD. We have also begun an effort to optimize the Stokes shifting in N_2 of the 532-nm output from the present broadband Nd:YAG laser and tripling the output in the nonlinear crystal BBO to generate the desired $1\omega,3\omega$ photodissociation fields. We are working to design, build, and demonstrate the gas cell, which will allow us to manipulate the relative phase between the $1\omega,3\omega$ laser fields. With the reaction cell operating, we will optimize our detection system using NO_2 fluorescence. We will then introduce HOD or H_2O into the cell, overtone pump the molecules to a single rovibrational level of the $4\nu_{OH}$ overtone state, photodissociate from the vibrationally excited state using 266-nm photons , and state-selectively detect the resulting OH or OD fragments using laser-induced fluorescence. The final step will be to switch to the $1\omega,3\omega$ photodissociation laser fields produced by the injection-seeded and Raman-shifted Nd:YAG laser, vary the relative phase and amplitude of the fields, and observe the effect on the distributions of the OH and OD fragment product states.

We are collaborating on this project with Jeff Krause in the Physics Department, who has started performing time-dependent calculations on the H_2O/HOD photodissociation system. This involves using established accurate ground- and excited-state potentials and generating and propagating wavepackets on these surfaces. These calculations can then be used to predict the effect of coherent excitation on product state distributions.

We have written and submitted a Labwide LDRD proposal for potential FY 93 funding. We are also planning to submit a proposal to the Office of Naval Research in midsummer for possible external funding in FY 93. We have also identified a postdoctoral candidate for potential involvement in this project in the event that external funding becomes available.

Growth and Transport of Crystalline Defects

J. J. De Yoreo and C. A. Ebbers

Overview

The goal of this work is to determine the controls of crystal chemistry and structure on the nucleation, growth, and transport of defects in certain classes of optical crystals. The result of this work will be to reduce or eliminate performance-limiting defects in these crystals. In addition, we believe that our approach will serve as a model for similar efforts in other areas of crystal synthesis. The imperfections being studied include point defects, submicrometer inclusions, dislocations, and associated strain fields. Our strategy is to develop a microscopic picture of defect formation and growth and to integrate that with an understanding of the connection between defects and crystal chemistry.

Our current work is focused on three areas, determining the source of internal strain in mixed crystals of $K(D_xH_{1-x})_2PO_4$, determining the mechanism of diffusion in lithium-bearing fluorides and oxides, and understanding the thermodynamic controls on phase separation in lithium-bearing fluorides.

Technical Activities

Source of Strain in the Mixed Crystalline System $K(D_xH_{1-x})_2PO_4$

We have now profiled the strain-induced birefringence of about 20 mixed crystals of lithium (KD*P) using an optical technique.[1] Employing our theoretical analysis, which quantitatively relates the components of the strain tensor to optical distortions,[1] we have analyzed the data to give the distribution of shear strain in the crystals. Our results thus far demonstrate the following:

- Maximum strains in the crystals range from 10 to 60 ppm.
- The level of strain can vary by orders of magnitude across a single crystal.
- Crystals from near the seed cap exhibit the largest strains, while those from the end of the boule are the least strained.
- Crystals cut from different locations along the length of a boule often display similar strain profiles, indicating that the source of the strain persisted throughout a significant portion of the growth history of the boule. An example of two such crystals is presented in Fig. 1, which shows the strain profiles of two 16- × 16-cm KD*P crystals cut from a single boule in which $x = 0.94$.

We have also begun a collaboration with Zophia Rek at the Stanford Synchrotron Radiation Laboratory (SSRL) to profile KD*P crystals using x-ray topography. Our goal is to determine the microstructural source of the strain responsible for the optical distortions. The results of our first run show that we can obtain high-quality topographs using white beam topography in reflection. The topographs collected thus far are rich in structure and reveal ubiquitous lattice deformities. Our next scheduled beam time is in June 1992, at which time we will finish the white-beam topography and begin mono-

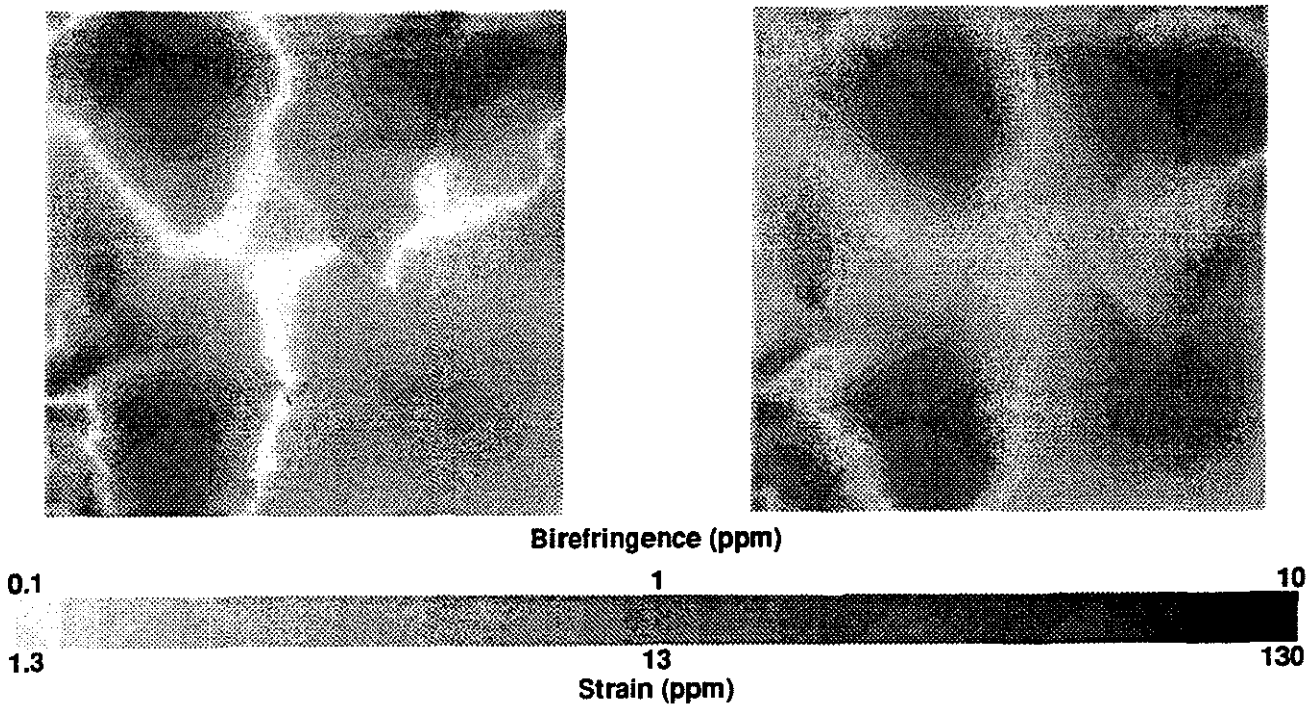

Figure 1. Profile of the measured birefringence and the calculated strain in two 16- × 16-cm plates of $K(D_xH_{1-x})PO_4$ cut perpendicular to the *c* axis from different locations along the length of a single boule. The similarity of the two profiles demonstrates that the source of the strain persists throughout a significant portion of the growth history of the boule.

chromatic x-ray topography. The latter technique will enable us to directly determine variations in lattice constants and is sensitive to strains of as little as 10^{-7}.

We have identified three potential sources of strain in KD*P: dislocations, impurities, and inhomogeneities in hydrogen level. Because x-ray topography both images dislocations and measures lattice strains directly, it should enable us to distinguish between these sources. Finally, we have analyzed existing thermodynamic data and found that the sensitivity of the hydrogen segregation coefficient to variations in growth parameters should increase with increasing deuterium content and lead to inhomogeneities in hydrogen content.[1] Structural considerations show that inhomogeneities in hydrogen content of 300 to 3000 ppm over macroscopic distances (>1 mm) would be required to generate the observed strain profiles through this mechanism.

Diffusion in Lithium-Bearing Fluorides and Oxides

During this reporting period, we have begun a novel TEM effort to observe defect, migration, precipitation, and dissolution in $LiCaAlF_6$ (LiCAF) and YLiF (YLF) using the environmental stage on the high-voltage electron microscope (HVEM) at Lawrence Berkeley Laboratory. This work is being performed by A. Meike of the Earth Sciences Department. Our previous work on these crystals has shown that they contain lithium-rich precipitates,[2] and our work on LiCAF has demonstrated that during precipitation and dissolution of these precipitates, lithium diffusion in this system is extremely rapid ($D > 10^{-7}$ cm^2·s^{-1} at 800°C).[3] By using the environmental stage, we are able to reproduce

the experimental conditions used in the previous experiments. We hope to observe, *in situ*, the formation and dissolution of the precipitates.

Thus far, we have succeeded in developing a microtoming technique for preparing samples with an exceptionally large area that is transparent to electrons. We have also performed our first set of cyclic heating runs in argon. While the preliminary results are not adequate to address microstructural issues, the diffraction patterns indicate that diffusion does occur and is measurable on the experimental time scale. Our next scheduled time on the HVEM is at the end of May 1992.

Finally, our annealing furnace is now operational, and we have received a batch of isotopically pure ^{7}LiF. We can now begin lithium diffusion experiments to determine the anisotropy of the diffusivity tensor.

Phase Separation in Lithium-Bearing Fluorides

Originally, we had planned to measure the heats of mixing in LiCAF and its strontium and gallium analogs in order to explore the role of enthalpy stabilization in controlling phase separation. However, this approach requires a broad range of solid solution.[4] Our electron microprobe measurements on LiCAF have shown that, regardless of starting composition, the resulting LiCAF phase has the same composition to within experimental error. Consequently, the range is too narrow to make this approach feasible. We have now synthesized several crystals of $LiSrAlF_6$ (LiSAF) from different starting compositions. In contrast to what is seen in LiCAF, initial observations show that the morphology and density of the second-phase precipitates vary from sample to sample and may indicate that the solid-solution range is broadened. If this turns out to be true, we may be able to use our calorimetric approach on this system.

References

1. J. J. De Yoreo and B. W. Woods, "A Study of Stress and the Stress-Optic Effect in Mixed Crystals of $K(D_xH_{1-x})_2PO_4$," *J. App. Phys.* (submitted).
2. J. J. De Yoreo, L. J. Atherton, D. H. Roberts, R. W. Martin, and R. Morris, "A Study of the Formation, Growth, and Elimination of Defects in Cr:$LiCaAlF_6$," *J. Appl. Phys.* (in preparation).
3. J. J. De Yoreo, L. J. Atherton, and D. H. Roberts, "Elimination of Scattering Centers from Cr:$LiCaAlF_6$," *J. Cryst. Growth*, **113**, 691 (1991).
4. J. J. De Yoreo, A. Navrotsky, and D. B. Dingwell, "Energetics of the Charge-Coupled Substitution $Si^{4+} \rightarrow Na^{1+} + T^{3+}$ in the glasses $NaTO_2$ - SiO_2 (T = Al, Fe, Ga, B)," *J. Am. Ceram. Soc.* **73**, 2068 (1990).

Presentations

1. J. J. De Yoreo, "The formation, Growth and Elimination of Defects in Cr:$LiCaAlF_6$," Cornell University, Ithaca, NY, November 1991.
2. J. J. De Yoreo, "Understanding Strain in KD*P: a First Attempt," Laser Materials Seminar, LLNL, December 1991.

Laboratory Directed Research and Development

Individual Projects

Inorganic and Organic Aerogels

L. W. Hrubesh, T. M. Tillotson, and R. W. Pekala

Overview

Aerogels are cluster-assembled porous materials in which both the cluster size and the cell/pore size are on the order of 10 to 20 nm. In most cases, the clusters are formed in dilute solution from the crosslinking of multifunctional organic or inorganic monomers. As expected, polymerization conditions and monomer type determine the microporosity and size of the individual clusters, ultimately affecting the properties of the resultant aerogel. In an alternative scheme, clusters of predetermined sizes and geometries (i.e., molecular building blocks) can be crosslinked to form aerogels. This research program investigates new types of monomers and/or molecular building blocks that lead to aerogels with unique compositions, improved properties, and tailored nanostructures. Recent accomplishments include the following:

- Synthesized and characterized silica aerogels derived from cube-shaped silsesquioxanes and alkyl-substituted trimethoxysilanes.
- Synthesized pure metal-oxide aerogels from titania, zirconia, and germania.
- Developed a synthetic approach for rare-earth–oxide aerogels using the corresponding metal chlorides.
- Established a procedure for making mixed silica/metal-oxide aerogels from alkoxide precursors without precipitate formation.
- Determined the thermal conductivity of resorcinol-formaldehyde aerogels.
- Synthesized new organic aerogels from the polycondensation of formaldehyde with resorcinol-phenol mixtures, catechol, pyrogallol, and 1,6 napthalenediol.
- Determined the gas permeability of carbon aerogels and developed a model for their structure.
- Measureed skeletal densities and pore size distribution for a series of carbon aerogels with densities ranging from 0.1 to 0.8 g/cm^3.

Technical Activities and Results

Organic Aerogels

The low thermal conductivities of aerogels are attributable to (1) their high porosity and thus their low solid conductivities, (2) their extremely small cell/pore sizes (1 to 50 nm) that cause a partial suppression of gaseous conductivity, and (3) their high specific extinction of thermal radiation. Because nonporous organic materials have smaller thermal conductivities than nonporous inorganic materials, we surmised that organic aerogels would have even lower thermal conductivities than silica aerogels. To verify this assumption, we performed caloric measurements on resorcinol-formaldehyde (RF)

aerogels using a hot-wire technique. Figure 1 shows the total thermal conductivity (λ_t) of RF aerogels as a function of density (ρ). The curve has a minimum of ~1.2 W/cm·K at $\rho = 0.16$ g/cm^3. The various conductivity components λ_r, λ_g, and λ_s also varied as a function of density; λ_s increased from about 0.2 to 1.4 W/cm·K, whereas λ_g decreased from about 1.0 to 0.3 W/cm·K as ρ increased from 0.08 to 0.30 g/cm^3. The data show that monolithic RF aerogels are the world's best insulators under ambient conditions, having even lower thermal conductivities than opacified (carbon black) silica aerogels. If the gaseous conductivity is suppressed by partial evacuation of the RF aerogel monolith, thermal conductivities of 0.6 W/cm·K can be achieved at $\rho = 0.08$ g/cm^3.[1]

The pyrolysis of resorcinol-formaldehyde aerogels results in vitreous carbon aerogels that are finding applications as catalyst supports, supercapacitors, battery electrodes, and gas filters. In each of these potential applications, knowledge of aerogel permeability is required. The most important properties that determine the permeability of a material are its porosity and microstructure. Small-angle x-ray scattering, transmission electron microscopy, and BET gas adsorption techniques show that carbon aerogels have porosity at two different length scales: (1) mesopores (2 to 50 nm) that span the distance between the interconnected colloidal-like particles and (2) micropores (<2 nm) that reside within the individual particles. In our test, the permeant follows the path of least resistance and provides us with a measure of the mesopore size. We chose to measure the flow resistance of nitrogen in thin aerogel specimens and deduced the permeability from Darcy's law based on the assumption that we have laminar viscous flow in a capillary model.

Figure 2 shows a log-log plot of permeability vs density for carbon aerogels synthesized at $R/C = 200$. The data show a power-law relationship in which

$$K = 8.86 \pm 0.61 \times 10^{-13}\rho^{-1.48 \pm 0.04} \quad (1)$$

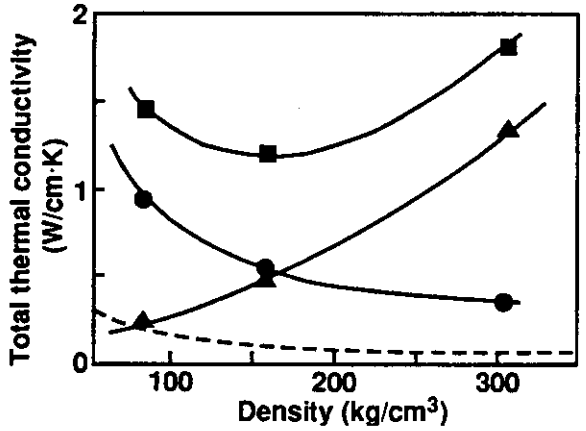

Figure 1. Total thermal conductivity λ_t (squares), calculated radiative conductivity λ_r, (dashed), gaseous conductivity λ_g (circles), and solid conductivity λ_s (triangles) of RF aerogels as a function of density under ambient conditions.

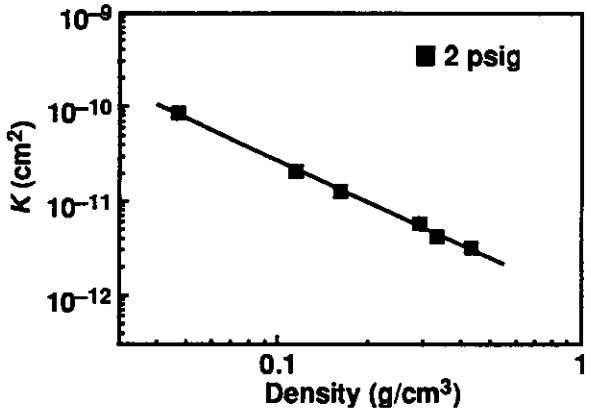

Figure 2. Effect of density on the permeability of carbon aerogels.

where K is the permeability in cm^2 and ρ is the aerogel density in g/cm^3. Comparing our data with the permeability of silica aerogels reported by others, we find that Eq. (1) appears to provide a universal model for the permeability of both organic and inorganic aerogels. For example, Schmitt reported a 0.132 g/cm^3 silica aerogel (acid catalysed) to have a permeability of 0.104 $cm^3/bar \cdot cm \cdot s$ in nitrogen.[2] Multiplying this value by the gas viscosity at test temperature and performing unit conversion, this permeability is equivalent to 1.78×10^{-11} cm^2. If the density of this silica aerogel is inserted into Eq. (1), we obtain a permeability of 1.77×10^{-11} cm^2, which is almost identical to the measured value. Fricke et al. revealed that a 0.280 g/cm^3 silica aerogel (base catalysed) had a diffusion coefficient, D_e, of ~4.4×10^{-6} cm^2/s at 1 bar in nitrogen.[3] Employing Fick's second law of diffusion and Darcy's law for viscous flow, we converted D_e into K and obtained 6.5×10^{-12} cm^2. On the other hand, if we use Eq. (1), K is calculated to be 5.83×10^{-12} cm^2, which is only 10% lower than the measured value.

Inorganic Aerogels

We synthesized new silica aerogels using a cube-shaped silsesquioxane and compared their properties with conventional aerogels. The cube-silica building block, $[Si_8O_{12}](OCH_3)_8$, was prepared for us by collaborators at the University of Illinois. We synthesized aerogels having densities in the range from 0.045 to 0.23 g/cm^3 and measured several of their properties as a function of density. We found that the cube-silica precursor results in stiffer aerogels than those made from either base-catalysed alkoxysilanes or condensed silica, and they have moduli comparable to the acid catalysed aerogels, as shown in Fig. 3. All other measured properties of these aerogels (e.g., surface area, pore and particle morphology, noncrystallinity) were indistinguishable from the other aerogels. We believe that the similarities of physical properties result from the random nature of the formation of clusters from these precursors so that any order of the microstructure is eliminated after a few linkages. Future work will be with molecular building blocks that already have some developed order in at least one dimension (e.g., tube alkoxysilanes).

We have synthesized new pure erbia and praseodymia aerogels, starting with the metal chloride as the reactive monomer. The metal chloride is dissolved in alcohol and reacted with water. Propylene oxide is added to scavenge the liberated hydrochloric acid and helps to induce gelation. These reactions are intentionally slowed by mixing at temperatures slightly above 0°C. The resulting gels were supercritically dried using both the high- and low-temperature methods. The high-temperature extracted aerogels were monolithic, transluscent, hydrophobic, and very weak. The low-temperature extracted aerogels were transparent and hydrophilic, but not monolithic.

Mixed aerogels were made by adding the rare-earth chloride-alcohol solution directly to prehydrolyzed tetramethoxysilane (condensed silica) in a two-step gelation process. The resulting solution is also partially condensed and serves as a precursor to make gels and aerogels. When these gels are supercritically extracted at high temperature, they result in transparent monoliths that are quite stable in atmospheric moisture.

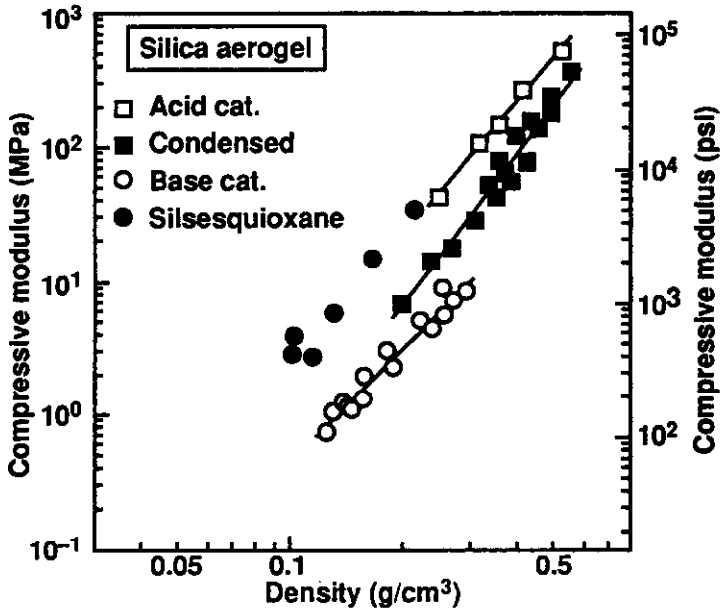

Figure 3. Compressive modulus vs density for silica aerogels. All aerogels were prepared from tetramethoxysilane except for the samples, which were synthesized from octamethoxy silsesquioxane.

References

1. X. Lu, M. C. Arduini-Schuster, J. Kuhn, O. Nilsson, J. Fricke, and R. W. Pekala, "Thermal Conductivity of Monolithic Organic Aerogels," *Science* **255**, 971 (1992).
2. W. J. Schmitt, *The Preparation and Properties of Acid-Catalysed Silica Aerogel*, M. S. thesis, University of Wisconsin (1982).
3. C. Stumpf, K. V. Gassler, G. Reichenauer, and J. Fricke, *Dynamic Gas Flow Measurements on Aerogels*, Physikalisches Institut der Universität Wurzburg, Report E21-0991-4 (1991).

Publications

1. J. Gross, J. Fricke, and L. W. Hrubesh, "Sound Propagation in SiO_2 aerogels," *J. Acoust. Soc. Am.* **91**(4), Pt. 1, 2004 (1992).
2. J. Gross, J. Fricke, R. W. Pekala, and L. W. Hrubesh, "Elastic Nonlinearity of Aerogels," *Phys. Rev. B*, in press.

Presentations

1. R. W. Pekala, "Carbon Aerogels and Xerogels," Novel Forms of Carbon Symposium, Materials Research Society Meeting, San Francisco, CA, April 27, 1992.
2. F. M. Kong, "Determination of the Permeability of Carbon Aerogels by Gas Flow Measurements," Novel Forms of Carbon Symposium, Materials Research Society Meeting, San Francisco, CA, April 27, 1992.
3. S. S. Hulsey, "The Effect of Pyrolysis Temperature and Formulation on Pore Size Distribution and Surface Area of Carbon Aerogels," Novel Forms of Carbon Symposium, Materials Research Society Meeting, San Francisco, CA, April 28, 1992.

Synthesis and Characterization of Melamine-Formaldehyde Aerogels

R. W. Pekala and C. T. Alviso

Overview

Aerogels with new compositions are helping us to understand (1) growth pathways during sol-gel polymerizations and (2) the structure-property relationships of this family of porous materials. In 1985, the first organic-based aerogels were synthesized from the aqueous polycondensation of resorcinol (1,3 dihydroxybenzene) with formaldehyde (RF). These low-density materials were found to be the organic analogs of silica aerogels, but with the advantage of having a lower average atomic number. The major disadvantage of resorcinol-formaldehyde aerogels was their dark red color, which results from oxidation products formed during the sol-gel polymerization. This project examines the formation of colorless, organic aerogels based on the polycondensation of melamine (2,4,6-triaminos-triazine) with formaldehyde.

Technical Activities and Results

Melamine-formaldehyde (MF) aerogels can be synthesized using either a *monomer* or an *oligomer* approach. The latter approach is preferred because it enables us to prepare aerogels over a wider pH range and it simplifies the synthetic procedure. A low molecular weight MF polymer (Resimene 714; Monsanto Chemical Co.) is utilized in the oligomer approach. Resimene 714 results from the condensation of melamine with formaldehyde followed by partial methoxylation. This oligomer is supplied as an 80% solution in water. MF gels are formed by diluting Resimene 714 with an appropriate amount of water and adjusting the pH with HCl. Transparent gels and aerogels are obtained between a pH of 2.0-3.0.

We have synthesized MF aerogels with densities ranging from 0.1–0.8 g/cm^3; however, the slow reaction kinetics prevent us from forming gels at low concentrations (<5%) within reasonable times. The inability to achieve low densities is a serious limitation of the MF process. In many cases, the most interesting properties of aerogels (e.g., ultralow sound velocities) occur at these low densities. Future work is being directed at finding new solvent systems or catalysts to accelerate gelation at low concentrations.

MF aerogels have extremely high surface areas (880 to 1020 m^2/g) with a maximum value being obtained at pH = 2.7. Figure 1 shows the dependence of specific surface area on solution pH for aerogels synthesized from a 15 w/v (%) solution. If the pH is fixed but the reactant concentration is varied, we find the surface area of the dried aerogels to be relatively constant (±10%) over a wide density range. This same result is observed for resorcinol-formaldehyde and silica aerogels, and it suggests that the size

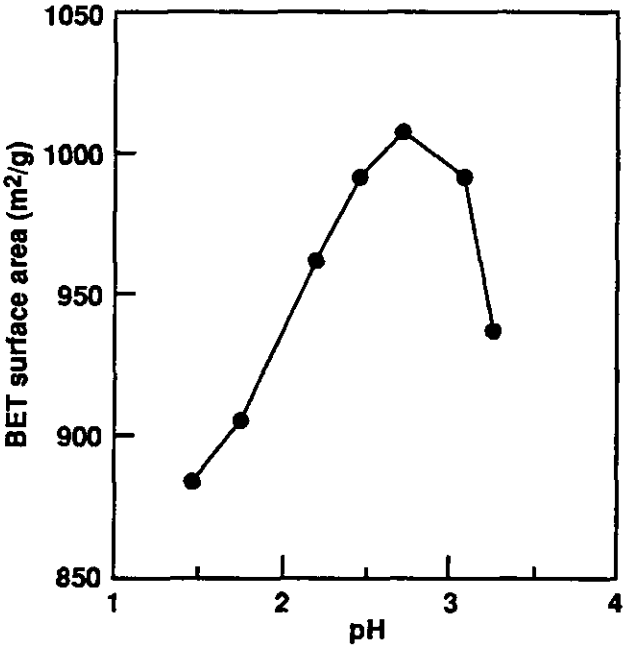

Figure 1. BET surface areas (nitrogen adsorption) for MF aerogels prepared at different pH values using the oligomer approach.

and porosity of clusters formed during the sol-gel polymerization dictate the final surface area.

Sound propagation (0.01 to 5 MHz) within MF aerogels and aerogels shows a power-law dependence on bulk density. The scaling exponent is 0.97 ± 0.10 over a density range of 0.15 to 1.5 g/cm^3. At 0.15 g/cm^3, MF aerogels display a longitudinal sound velocity of 235 m/s. One of the most striking features of MF aerogels is the decrease of sound velocity upon uniaxial compression (1 to 3% strain). This same phenomenon has been observed in silica and RF aerogels, and it has been explained by a "knee model" for the internal structure.[1] This model recognizes that aerogels are composed of chain-like structures. Due to the statistical growth process of the gel, these chains are normally not straight but are bent like "knees." When stressed, the knee angles are decreased and the chain thus becomes weaker, even if the material it is made from is linear elastic. The longer the chains are, the easier they can be bent, which causes the observed density dependence of the elastic nonlinearity.

The ultrafine cell/pore size and low density of aerogels are responsible for their low thermal conductivities as compared to their full-density analogs. In general, organic-based materials have lower thermal conductivities than ceramics, glasses, or metals. As such, organic aerogels were expected to have lower thermal conductivities than silica aerogels at equivalent densities. Table 1 shows the total thermal conductivity and the relative radiative, solid, and gaseous components for two different MF aerogels. These values are similar to RF aerogels, which are known to be the world's best thermal insulators.[2] One major advantage of the MF aerogels is that they are both colorless and transparent, as opposed to the RF aerogels, which are dark red. Additional MF aerogels are being synthesized so that a complete thermal conductivity-vs-density curve can be obtained.

Table 1. Thermal conductivity of MF aerogels.

Density (g/cm^3)	Thermal conductivity (W/m-K)	Radiative conductivity	Solid conductivity	Gaseous conductivity
0.266	0.0163	0.0011	0.0102	0.0050
0.403	0.0265	0.0006	0.0334	0.0025

In summary, MF aerogels display thermal, acoustic, and optical properties that are similar to silica aerogels. Solution pH is the major variable that controls the structure and properties of MF aerogels.

References

1. J. Gross, J. Fricke, R. W. Pekala, and L. W. Hrubesh, "Elastic Nonlinearity of Aerogels," *Phys. Rev. B*, in press.
2. X. Lu, M. C. Arduini-Schuster, J. Kuhn, O. Nilsson, J. Fricke, and R. W. Pekala, "Thermal Conductivity of Monolithic Organic Aerogels," *Science* **255**, 971(1992).

Publications

R. W. Pekala, F.-M. Kong, S. S. Hulsey, and C. T. Alviso, "Aerogels Derived from Multifunctional Organic Monomers," *J. Non-Cryst. Solids*, in press.

Presentations

R. W. Pekala, "The Synthesis and Characterization of Organic Aerogels," Corporate Seminar Series, Raychem Corporation, Menlo Park, CA, March 18, 1992.

Structural Transformation and Precursor Phenomena in Advanced Materials

P. E. A. Turchi, S. C. Moss,* and L. T. Reinhard

Overview

The study of the formation and the stability of complex crystalline structures, occurring either in bulk materials or in low-dimensional systems, is of crucial importance for both the technological and theoretical fields of condensed-matter physics. This motivation derives from the unique properties of complex phases, in particular those based on tetrahedrally close packed (tcp) structures. For example, the sigma phase is known to occur as a nuisance precipitate with deleterious mechanical effects in various high-temperature materials (e.g., the embrittlement of Fe-Cr–based stainless steels, of particular concern in nuclear reactors). To modify, optimize and control the formation of these phases, there is a need to combine experimental and theoretical tools to probe the nucleation and growth processes at very early stages. This requires atomistic monitoring of precursor phenomena, namely local chemical order and static atomic-displacement field, and transient structures that may act as seeds for the structural transformation. These properties are studied both theoretically with modern electronic structure theory of phase stability and experimentally with x-ray and neutron scattering techniques for bcc-based Fe-Cr alloys that exhibit a transformation to a complex σ phase upon cooling. Based on preliminary findings, a new experimental strategy was defined to thoroughly investigate the possibility of an early stage of nucleation of the complex phase confined to the vicinity of the free surface of the bcc phase.

Progress to Date

In direct support of the experimental effort, tendencies toward order or phase separation in Fe-Cr and Fe-V bcc-based alloys were examined with one of our recently developed *ab initio* tools to study alloy phase stability.[1–3] Around equiatomic composition, it was found that FeCr tends toward phase separation whereas FeV tends toward order with a CsCl-type of order.[4] Additional analysis has shown that although FeCr ultimately phase-separates, a metastable phase is identified at low temperature.[5] This phase comprises two planes of iron and two planes of chromium repeated periodically perpendicular to the (110) of the bcc lattice (see Fig. 1). The critical order-disorder temperature is of the order of 340 K, as deduced from Monte Carlo simulations performed with the theoretically determined energetic parameters. Therefore, FeCr becomes a prototypical case in which a competition between alloying effect (in favor of phase separation) and local chemical order may compete.

This work was extended to a series of equiatomic bcc-based alloys, including FeTi, TiCr, TiV, TiMn, and VCr. The conclusions are as follows:

---

* Physics Department, the University of Houston, Houston, TX

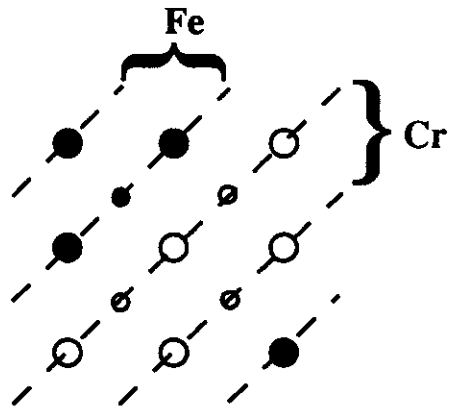

Figure 1. Bcc-based FeCr ordered configuration predicted from first-principles KKR-CPA-GPM electronic-structure calculations.

- The strength of the chemical affinity of the alloy species is essentially controlled by the average number of valence electrons and the difference in the numbers of valence electrons of the alloy components.
- A possible transformation to a complex phase may be associated with weak tendencies toward order or phase separation.

We definitely show that strong chemical order, as in FeTi, prevents the formation of complex phases. Hence, this study demonstrates, at an atomic level, the possible role played by ternary additions in stabilizing complex phases or ordered superstructures that are not observed in the binary combinations.

On the experimental side, FeCr, a basis of many commercially interesting alloys, has been selected for the study of precursor phenomena. This alloy exhibits a bcc-solid solution above 1094 K near equiatomic composition and transforms into a σ phase upon cooling. Due to a favorably slow kinetics of transformation, single crystals with the high-temperature crystalline structure (around 47 at.% Cr) were successfully obtained.

Neutron-scattering experiments on a $Fe_{0.53}Cr_{0.47}$ single crystal have been performed in collaboration with J. L. Robertson (NIST). Inelastic phonon scattering as well as diffuse elastic scattering close to the Bragg reflections (Huang scattering) have been investigated. The results of the phonon dispersion measurements have been fully analyzed,[6] whereas the diffuse scattering data are still being evaluated. Together with our x-ray scattering measurements on the same sample,[7] these results will lead to a better understanding of the intricate atomic displacement effects in the Fe-Cr high-temperature bcc-based solid solution, which may explain the structural transformation.

In collaboration with L. Tanner and M. Wall (LLNL), we are conducting a TEM investigation of the orientation relationships between the σ precipitates and the bcc matrix in FeCr. The results will provide a link with our surface studies on the σ-phase formation in this system. In the area of surface physics, we have established a collaboration with J. E. Houston (SNL, Albuquerque). We will perform a LEED investigation of the possible surface-induced bcc-to-σ transformation in FeCr single crytals oriented along (110) and (111). This experiment is scheduled for April 1992. Final sample preparations are under way. This study will preclude a more quantitative investigation

based on x-ray grazing-incidence diffraction, which is planned at the National Synchrotron Light Source at Brookhaven in collaboration with K. S. Liang (Exxon).

The pair-interaction energy parameters obtained from our diffuse x-ray scattering experiments[7] have been employed to compute the Fe-Cr phase diagram and to analyze the kinetics of decomposition with the Monte Carlo simulation technique. The miscibility gap thus obtained is in excellent agreement with the assessed one,[8] as shown in Fig. 2. These results lead to interesting comparisons with first-principles electronic-structure studies in this system.[5]

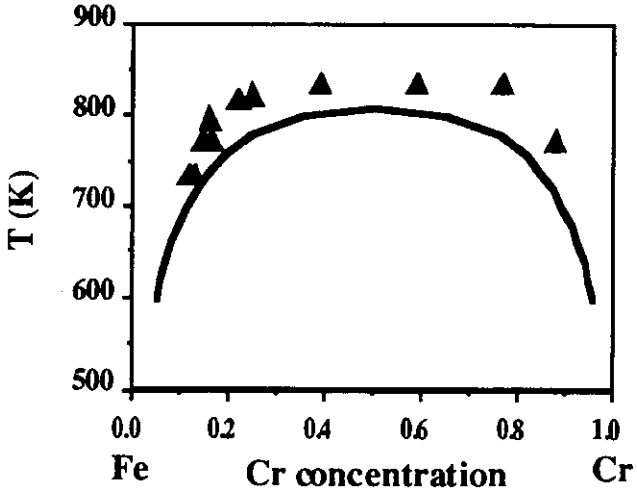

Figure 2. Bcc-based FeCr phase diagram obtained by Monte Carlo simulations from our deduced interaction energy parameters.[7] The triangles delineate the experimental metastable miscibility gap.

Future Work

On the theory side, work is being done (1) to provide a deeper insight into the role played by atomic orbital directionality in the stability of complex phases by analyzing the moments of the DOS in the tight binding framework and (2) to study the effect of ternary addition on the occurrence and the stability of complex phases. Codes have been developed to study, at an atomic level, structural transformations with a proper combination of electronic-structure calculations and molecular-dynamics simulations.

On the experimental side, fundamental questions are being addressed on (1) surface reconstruction and segregation in the bcc phase prior to the bcc-to-σ transformation, (2) orientation relationships between bcc and σ near the surface, and (3) fundamental understanding of the kinetics of transformation near the surface. Pertinent probes include Auger spectroscopy, low-energy electron diffraction (in collaboration with J. E. Houston at SNL, Albuquerque), grazing-incidence x-ray diffraction (on the Exxon beamline X10a at NSLS, in collaboration with K. S. Liang of Exxon). Additional diffuse scattering experiments near the Bragg peaks will be done to confirm (or not) detailed theoretical predictions on the short-range order in this alloy (in collaboration with J. L. Robertson from NIST and S. C. Moss).

References

1. P. E. A. Turchi, M. Sluiter, F. J. Pinski, D. D. Johnson, D. M. Nicholson, G. M. Stocks, and J. B. Staunton, "First Principles Study of Phase Stability in Cu-Zn Substitutional Alloys," *Phys. Rev. Lett.* **67**, 1779 (1991); Erratum, *Phys. Rev. Lett.* **68**, 418 (1992).
2. P. E. A. Turchi and M. Sluiter, "Real Space Multiple Scattering Description of Phase Stability in Alloys," *Mater. Res. Soc. Symp. Proc.* **253**, W. H. Butler, P. H. Dederichs, A. Gonis, and R. Weaver, Eds. (MRS, Pittsburgh, PA, 1992), p. 227.
3. P. E. A. Turchi, M. Sluiter, G. M. Stocks, "First-Principles Prediction of Alloy Phase Stability," *J. Phase Equilibria* (see LLNL Preprint UCRL-JC-109140), in press.
4. P. E. A. Turchi, M. Sluiter, and G. M. Stocks, "A Comparative Study of Short Range Order in Fe-Cr and Fe-V Alloys Around Equiatomic Composition," *Mater. Res. Soc. Symp. Proc.* **213** (MRS, Pittsburgh, PA, 1991), p. 75.
5. P. E. A. Turchi, L. Reinhard, M. Sluiter, and G.M. Stocks, "First Principles Study of Local Order in bcc-Based FeV and FeCr Alloys," to be published in *Phys. Rev. B.*
6. J. L. Robertson, D. A. Neumann, S. C. Moss, and L. Reinhard, "Inelastic Neutron Scattering Study of Phonon Dispersion in FeCr Near the σ-Phase Transformation," to be published in *Acta Metall.* (1992).
7. L. Reinhard, J. L. Robertson, S. C. Moss, G. E. Ice, P. Zschack, and C. J. Sparks, "Anomalous X-Ray Scattering Study of Local Order in bcc $Fe_{0.53}Cr_{0.47}$," *Phys. Rev. B* **45**, 2662 (1992).
8. L. Reinhard, J. L. Robertson, S. C. Moss, G. E. Ice, P. Zschack, and C. J. Sparks, "Anomalous X-Ray Scattering Study of Local Order in bcc $Fe_{0.53}$ $Cr_{0.47}$," to be published in the *Proc. TMS Symp. on Ordering Transformations in Metals* (1992) (see LLNL Preprint URCL-JC-109905).

Presentations

1. P. E. A. Turchi and M. Sluiter, "Real Space Multiple Scattering Description of Phase Stability in Alloys," MRS Fall Meeting in the Symposium on Application of Multiple Scattering Theory to Materials Science, Boston, MA, December 2–6, 1991.
2. P. E. A. Turchi, M. Sluiter, G. M. Stocks, "First-Principles Prediction of Alloy Phase Stability," ASM Conference on Phase Diagram Computation, TMS Fall Meeting, Cincinnati, OH, October 21–24, 1991.
3. G. M. Stocks, D. M. Nicholson, W. A. Shelton, F. J. Pinski, D. D. Johnson, J. B. Staunton, A. Barbieri, B. L. Gyorffy, B. Ginatempo, P. E. A. Turchi, and M. Sluiter, "Ordering Mechanisms in Metallic Alloys," ASM Conference on Computation Simulation Applied to Phase Transformation, TMS Fall Meeting, Cincinnati, OH, October 21–24, 1991.
4. L. Reinhard, J. L. Robertson, S. C. Moss, G. E. Ice, P. Zschack, and C. J. Sparks, "Anomalous X-Ray Scattering Study of Local Order in bcc $Fe_{0.53}$ $Cr_{0.47}$," Symposium on Ordering Transformations in Metals, held at the TMS Annual Meeting, San Diego, CA, March 2–5, 1992.
5. J. L. Robertson, D. A. Neumann, S. C. Moss and L. Reinhard, "Inelastic Neutron Scattering Study of Phonon Dispersion in FeCr near the σ-Phase Transformation," 1992 March meeting of the APS, Indianapolis, IN, March 16–20, 1992.
6. L. Reinhard and P. E. A. Turchi, "Monte Carlo Simulations and Cluster Variation Method Studies of Phase Decomposition in FeCr," 1992 March meeting of the APS, Indianapolis, IN, March 16–20, 1992.

Magnetic Ultrathin Films, Surfaces, and Overlayers

J. G. Tobin

Overview

We have used circularly polarized x rays to perform magnetic circular dichroism experiments on ultrathin films of Fe/Cu(001) and US/polycrystalline uranium. Our x-ray absorption and core-level photoemission investigation of Fe/Cu(001) is the first such study of ultrathin magnetic films. In fact, we have observed a giant effect in the x-ray absorption, with asymmetries of 20 to 40%. We have also studied US ultrathin films, and a preliminary investigation suggests that there may be a magnetic circular dichroism (MCD) effect. This would be the first direct, elementally specific evidence of 5f magnetism. C. Colmenares and T. Gouder collaborated in this work. D. P. Pappas of IBM was a collaborator in our early studies of Fe/Cu(001). We are also continuing our collaboration with Professor S. Y. Tong of UW-Milwaukee, using photoelectron diffraction to probe the local geometry of the Fe/Cu surface. Mehdi Balooch is working on applying STM to these surfaces.

Magnetic Circular Dichroism in X-Ray Absorption and Core-Level Photoemission of Fe/Cu(001)

We report the first observation of MCD in both x-ray absorption and core-level photoemission of ultrathin magnetic films using circularly polarized x rays. Iron films (1 to 4 ML) grown on a Cu(001) substrate at 150 K and magnetized perpendicular to the surface show *dramatic* changes in the $L_{2,3}$ branching ratio for different x-ray polarizations. For linearly polarized x rays perpendicular to the magnetic axis of the sample, the branching ratio was 0.75. For films $\geq$ 2 ML, this ratio varied from 0.64 to 0.85 for photon spin parallel and antiparallel, respectively, to the magnetic axis. This corresponds to MCD asymmetries on the order of 20 to 40%, which is an order of magnitude larger than that observed previously (see Fig. 1). These effects were observed either by changing the x-ray helicity for a fixed magnetic axis, or by reversing the magnetic axis for a fixed x-ray helicity. Furthermore, warming the films to ~300 K eliminated this effect, indicating a loss of magnetization in the film over a temperature range of ~30 K. Finally, reversing the relative orientation of the photon spin and the magnetic axis from parallel to antiparallel allowed measurement of the exchange splitting of the Fe 2p core level, which was found to be ~0.2 eV. These results are consistent with earlier studies, but the use of off-plane circularly polarized x rays from a bending magnet monochromator offers ~2 orders of magnitude greater intensity than typical spin-polarization measurements.

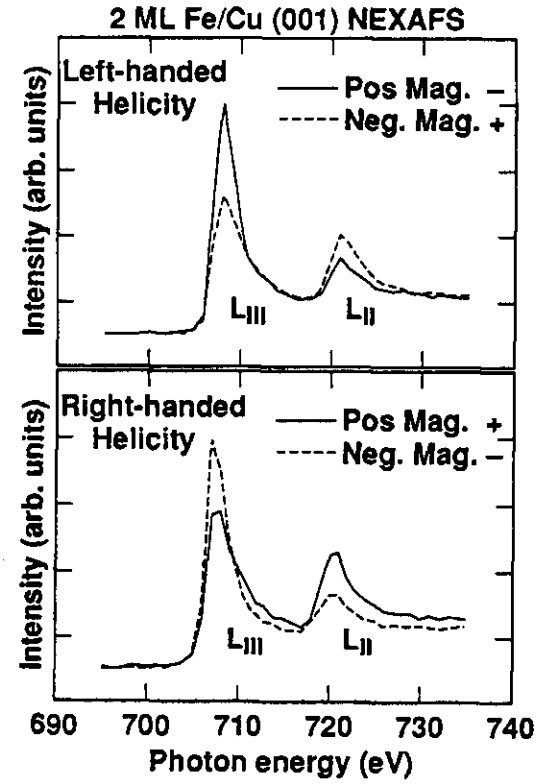

Figure 1. The near-edge x-ray absorption fine structure (NEXAFS) dichroism of 2 ML of Fe/Cu(001). These are plots of absorption vs photon energy. The upper panel shows the effect of reversing the magnetization while maintaining the left-handed helicity of x rays; similarly for the lower panel and right-handed helicity x rays. Samples are perpendicularly magnetized either into (pos. mag.) or out of (neg. mag.) the surface. The symbols + and – mean that the helicity and magnetization are parallel (+) or antiparallel (–). The $2p_{3/2}$ peak is at the LIII edge, and the $2p_{1/2}$ peak is at the LII edge. The spectra were normalized to each other by equating the pre-edge intensity at energies below about 700 eV.

Beamline Modification–Helicity Selection

In collaboration with J. Stöhr et al. of IBM Almaden Research and Mike Rowen of SSRL, we have installed helicity detectors and a helicity selector in beamline 8–3. The helicity detectors are magnetized CoPd multilayers that can be used to test for success in helicity selection. Originally, helicity or circular polarization selection was done by moving the first mirror vertically. Now, we insert a small slit to perform the helicity selection. Our SGM is only one of two beamlines in the USA that can do this.

Publications

1. J. G. Tobin, G. D. Waddill, and D. P. Pappas, "Giant X-Ray Absorption Circular Dichroism in Magnetic Ultrathin Films of Fe/Cu(001)," submitted to *Phys. Rev. Lett.*, November 1991.
2. G. D. Waddill, J. G. Tobin, and D. P. Pappas, "Magnetic Dichroism in Core Level Photoemission from F.C.C. Fe/Cu(001) Films," submitted to *Phys. Rev. B—Rapid Commun.*, February 1992.
3. J. G. Tobin, M. K. Wagner, X.-Q. Guo, and S. Y. Tong, "Photoelectron Diffraction of Magnetic Ultrathin Films," *Mater. Res. Soc. Symp. Proc.* **208**, 283 (1991).
4. J. C. Hansen, M. K. Wagner, and J. G. Tobin, "Concentration Dependent Surface-State Shifts," *Mater. Res. Soc. Symp. Proc.* **229**, 9 (1991).

5. L. J. Terminello, G. D. Waddill, and J. G. Tobin, "High Resolution Photoabsorption and Circular Polarization Measurements on the University of California/National Laboratory Spherical Grating Monochromator Beamline," *Nucl. Instrum. Methods*, July/August 1992.

Invited Talk

J. G. Tobin, "Synchrotron Radiation Based Investigation of Magnetic Ultrathin Films: Fe/Cu(001)," SSRL Users Meeting, Stanford, CA, November 1991.

Contributed Talks

1. J. G. Tobin, G. D. Waddill, D. P. Pappas, S. Y. Tong, X.-Q. Guo, and M. K. Wagner, "Synchrotron Radiation Studies of Magnetic Ultrathin Films Using Photoelectron Diffraction and X-Ray Magnetic Circular Dichroism," 17th DOE Surface Studies Conference, Pleasanton, CA, October 1991.
2. G. D. Waddill, J. G. Tobin, and D. P. Pappas, "Magnetic Circular Dichroism in X-Ray Absorption and Core Level Photoemission of Fe/Cu(001)," *Bull. Am. Phys. Soc.* **37**, 144 (1992).

Report

J. G. Tobin, G. D. Waddill, D. P. Pappas, S. Y. Tong, X.-Q. Guo, and P. A. Sterne, *The Structures and Properties of Ultrathin Magnetic Films*, SSRL Annual Activity Report, January 1992.

Ductile-Phase Toughening of Refractory-Metal Intermetallics

G. A. Henshall and M. J. Strum

Overview

Refractory-metal intermetallic compounds could satisfy needs for high-strength and creep resistance at extremely high temperatures if they can be toughened by the dispersion of a ductile second phase. In this investigation, *in situ* methods are being explored as a means of synthesizing V-V_3Si composites, in which the ductile vanadium is dispersed within the brittle V_3Si matrix by phase separation during solidification. A variety of experiments and finite-element modeling (FEM) analyses are being performed to assess the capability of ductile-phase toughening to improve the low-temperature toughness of V_3Si while maintaining superior high-temperature creep properties.

Detailed Description

The continuing need for improved lightweight structural materials for high-temperature service has led to the investigation of high–melting-point intermetallic compounds.[1] Service temperatures of up to 1400°C are foreseeable for refractory-metal intermetallics, which is well above the projected 1000°C useful limit of nickel-based superalloys and well-studied aluminides. However, due to their complex crystal structures, refractory-metal intermetallics lack the ambient-temperature toughness required for damage tolerance. One approach to solving this problem is through *ductile-phase toughening*, in which a ductile phase (which itself must have a high melting point) is dispersed in the intermetallic matrix. The ductile phase may increase toughness by "bridging" the crack faces, thereby inhibiting crack opening, or by blunting the crack tip.

Vanadium-silicon was chosen as a system that has potential significance technologically. With this system, the intermetallic phase is V_3Si (A15 structure), and the ductile phase is a solid solution of silicon in vanadium, V(Si), which may precipitate out small particles of V_3Si upon heat treatment. Both phases have densities significantly lower than nickel-based superalloys, an important consideration in aerospace structures, and vanadium has excellent low-temperature ductility, perhaps making it a good toughening agent. Methods for synthesizing the V-Si alloys are currently under development, with the initial goal of producing homogeneous materials with impurity content as low as possible. To date, vacuum arc-casting methods have been used to produce four *in situ* composites. The compositions were chosen to provide a wide range of ductile phase fractions: 30, 50, 70, and 100 vol%. The latter composition will be used to determine the properties of the ductile phase for use in the modeling efforts.

Following synthesis, the first step was to confirm whether the V(Si) phase is ductile, since the ductility of vanadium is sensitive to interstitial impurities and alloying additions such as silicon.[2] Preliminary indications are that this phase has sufficient ductility to provide effective toughening. As shown in Fig. 1(a), microhardness indentations within the brittle V_3Si intermetallic produce cracks. These cracks abruptly end, however, when they reach the V(Si) phase. Furthermore, Fig. 1(b) shows that macrohardness indentations produced cracks that "jump" from one V_3Si particle to the next, while the interspersed areas of fine eutectic remain uncracked. This behavior indicates that the V(Si) phase bridges the crack, as desired. Finally, based on the length of cracks emanating from microhardness indentations,[3] preliminary toughness calculations indicate that the eutectic structure is significantly tougher than the intermetallic. Bulk fracture toughness tests are under way to further quantify the toughness of these materials.

In an effort to better understand the mechanisms of ductile-phase toughening and their relationship to microstructure, a finite-element study has begun. The increase in the work of fracture, ΔG, caused by crack-tip bridging of the ductile phase is expected to be[4]

$$\Delta G = f\int_0^{u^*}\sigma(u)\,du \quad - \quad fG_m \ , \tag{1}$$

where f is the area fraction of ductile phase, G_m is the matrix fracture energy, and σ is the nominal stress across the ductile ligament at a displacement of u (σ falling to

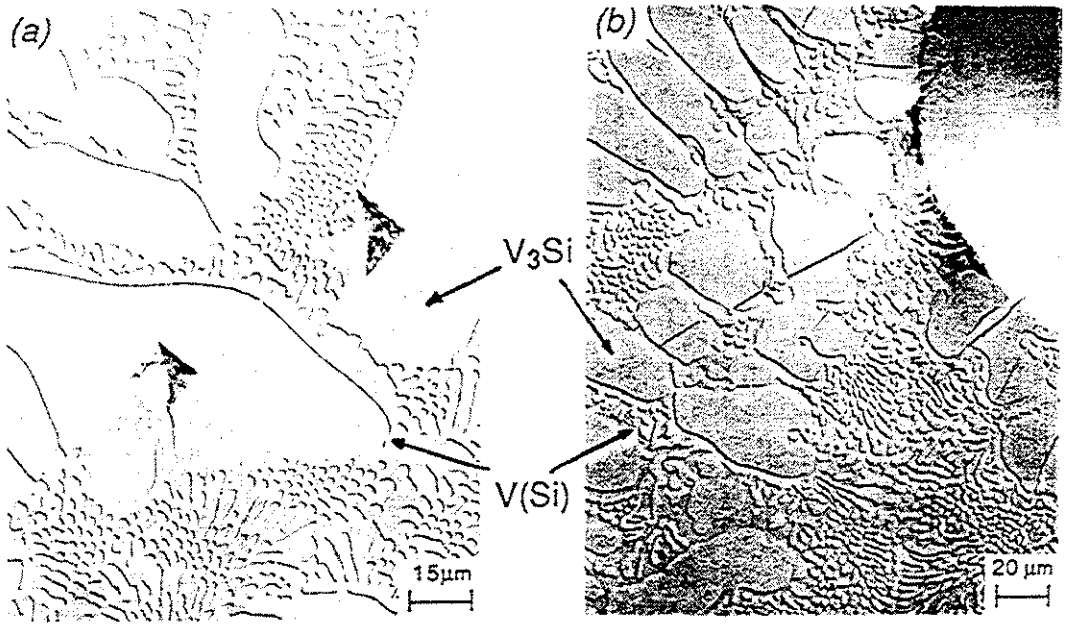

Figure 1. Optical micrographs of hardness indentations in a V-Si composite provide evidence for (a) crack-tip blunting, and (b) crack-tip bridging.

zero at $u = u^*$). Thus, the first step in calculating ΔG is to establish the $\sigma - u$ relationship of the ductile particle under the constraint imposed by the cracked matrix when a far-field stress is applied. Figure 2(a) shows the two-dimensional representation of a cylindrical brittle matrix with an embedded spherical ductile particle for which NIKE2D calculations were made. A blunt crack of initial length a_0 and crack tip radius r_0 has penetrated the matrix and intercepted the particle. Under the influence of a far-field applied axial stress, the nominal stress (normalized by the particle yield stress, σ_0) vs axial displacement of the crack tip (normalized by a_0) behavior is shown in Fig. 2(b). The results for small u/a_0 are reasonably consistent with those reported by Mataga.[4] In addition, NIKE2D predicts the subsequent decrease in σ/σ_0 with increasing u/a_0 as the matrix constraint decreases, which has been observed experimentally.[5] These efforts will continue in an attempt to assess the influences of ductile phase properties, size, and shape of the ductile reinforcement, the effects of interface sliding, and thermal residual stresses on the work required to open the crack.

To understand the creep behavior of composites, one must understand the microscopic creep mechanisms for each phase, as well as the way in which the stress is distributed between the phases as a function of time. The latter is a continuum mechanics problem and does not depend on the details of the dislocation creep mechanisms. Therefore, to study the stress distribution in composites, experiments can be performed using a low-temperature model system to reduce their complexity and cost.[6] The major requirements of the model system are that the two phases

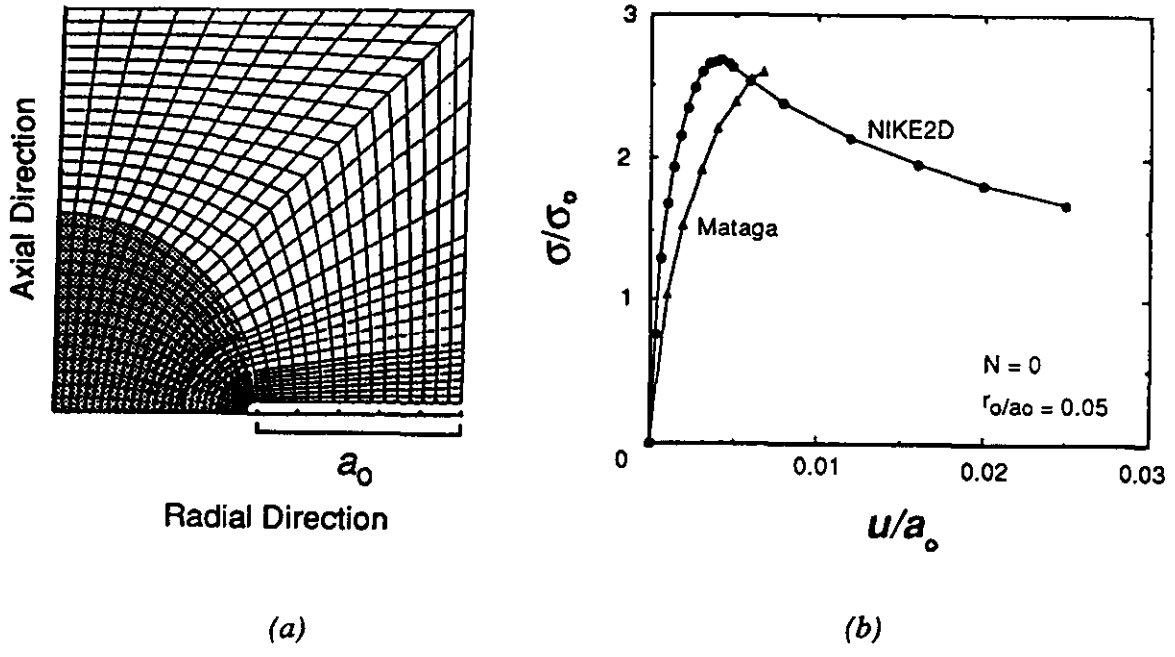

Figure 2. (a) The mesh used for NIKE2D calculations of crack opening in a ductile-phase toughened composite. The ductile particle is shaded. (b) The results of NIKE2D calculations of the $\sigma - u$ relationship are compared with calculations of Mataga.[4]

have widely different creep rates at low temperatures and that the microstructure is similar to that of the actual high-temperature system—in this case, a eutectic structure. The Al-Sn system exhibits these characteristics and was selected for study. One composite (50% ductile phase) has been vacuum-arc cast. Unfortunately, macrosegregation of the elements occurred, so improved casting methods now are being explored. In addition, FEM analyses of the creep behavior of ductile-phase toughened composites has begun. Preliminary results indicate that the composite creep rate deviates from the rule-of-mixtures prediction due to the presence of nonuniform stresses, which redistribute during creep. Geometrical effects also appear to be contributing to the deviation.

References

1. D. M. Dimiduk and D. B. Miracle, *Mater. Res. Soc. Symp.*, **133**, pp. 349–359 (1989).
2. R. E. Gold et al., *Technical Assessment of Vanadium-Base Alloys for Fusion Reactor Applications*, Westinghouse report COO-4540-1, Vol. 2 (1978).
3. A. G. Evans, "Fracture Toughness: The Role of Indentation Techniques," *Fracture Mechanics Applied to Brittle Materials, ASTM STP 678*, S. W. Freiman, Ed. (American Society for Testing and Materials, 1979), pp. 112–135.
4. P. A. Mataga, *Acta Metall.* **37**, 3349–3359 (1989).
5. M. F. Ashby, F. J. Blunt, and M. Bannister, *Acta Metall.* **37**, 1847–1857 (1989).
6. T. L. Dragone, J. J. Schlautmann, and W. D. Nix, *Metall Trans. A*, **22**, 1029–1036 (1991).

Particle-Solid Interactions

T. Diaz de la Rubia and M. W. Guinan

Overview

The focus of this research is on intermetallic compounds and new materials. Current activities focus on two topics:

- Molecular dynamics (MD) simulation studies of disordering, atomic mixing, and defect production in intermetallic compounds. Although experimental information regarding disordering rates and defect production under irradiation is readily available, little is understood about the mechanisms controlling these processes. Moreover, diffusion mechanisms in intermetallics are not well understood, and our MD studies are aimed at helping to elucidate such phenomena.
- An active collaboration with Rutgers University has been initiated to evaluate the response to particle irradiation of bulk nanocrystalline materials, a new class of solids with novel structure-property relations.

Technical Activities

MD Studies of Intermetallic $L1_2$ Alloys

Current models of radiation-induced disordering of intermetallics predict a relation for the Bragg-Williams long-range order parmeter of the form $S = S_0 \exp(-\alpha \cdot \phi)$, where α is a disordering constant independent of S but dependent on irradiation type, and ϕ is the irradiation dose. However, experiments performed at the RTNS-II facility at LLNL in 1988 have shown this not to be the case. A larger disordering rate has been found for low initial values of S_0 and for high T_0, indicating that lattice effects might be important in controlling the rate of disordering under irradiation.

We are completing a study of the dependence of the change in the Bragg-Williams long-range order parameter, S, of Cu_3Au on recoil energy. We have found a strong correlation between cascade lifetime, τ, and decrease in the order parameter, ΔS, for copper recoils in the range of 0.5 to 5 keV, and an initial value of $S_0 = 1$. This strong correlation between τ and ΔS indicates that intracascade atomic diffusion governs the disordering process during irradiation. At early times (0.5 ps), the average temperature in the inner 15-Å region of a 2.5-keV cascade exceeds 3000 K, and the cooling rate is on the order of 1×10^{15} K/s. At later times (7 ps), the temperature of the cascade region has fallen below the order-disorder transition temperature ($T_{O\text{-}D} = 663$ K).

Analysis of the time evolution of S indicates that kinetic constraints keep it from reaching a value consistent with the extremely high temperatures. The very fast quenching of the cascade core prevents the system from completely disordering. Moreover, the low

ordering energy of this alloy prevents the cascade region from reordering during the cooling stage.

Within the next five months, we will have completed simulation studies of cascades in Cu_3Au with $S_0 < 1$. Additionally, by the end of FY 92, we expect to have completed MD simulations at elevated temperatures as well as comparative studies in Ni_3Al, which, contrary to Cu_3Au, does not show an order-disorder transition below the melting point.

Radiation Effects in Bulk Nanocrystalline Solids

We have initiated a collaboration with Prof. H. Hahn of the Department of Materials Science and Engineering at Rutgers University to characterize the response of novel bulk nanocrystalline solids to irradiation with energetic particles. This work has an experimental component carried out primarily at Rutgers University as well as a theoretical MD component that will be performed at LLNL.

Bulk nanocrystalline solids are new materials with novel structure-property relations that have been shown to possess a structure in which as many as 50% of the atoms are located at internal interfaces. This comes about as a result of the extremely small grain size of the as-prepared material. Because of this small grain size, the radiation-damage properties of these materials might be of great interest and technological importance. Grain boundaries are known to act as very efficient sinks for point defects. Since displacement cascade sizes are comparable to the size of the grains, increased defect annihilation at the grain boundaries is expected. This phenomenon might lead to new materials with improved performance in radiation fields and novel surface-to-bulk property relations.

By the end of FY 92, we will have performed some preliminary irradiation experiments of nanocrystalline lead and silver to characterize in detail the evolution of the grain-size distribution during irradiation. This step is needed to understand how to control the ion-beam–induced grain growth and should continue during FY 93. During the remainder of FY 92, we will start preliminary MD studies of defect–grain-boundary interactions that will provide information on the sink strength of the interfaces for different types of defects and will therefore aid in designing future experiments. These studies will also be continued through FY 93.

Presentations and Publications

Two abstracts on disordering of intermetallic compounds under irradiation have been submitted to the Eighth International Conference on Ion Beam Modification of Materials, to be held in Heidelberg, Germany, September 7–11, 1992. Papers will be published in the conference proceedings as an issue of *Nuclear Intruments and Methods B.*

Electronic Structure Evolution of Metal Clusters

M. J. Fluss, V. V. Kresin, R. H. Howell, and W. D. Knight*

Overview

The present project is designed to study the electronic properties of small metal clusters. These objects have attracted significant interdisciplinary interest in the past few years, due both to their intrinsic scientific value and to the range of potential applications (e.g., new materials, catalysis, atmospheric sciences, and optical and magnetic recording).

The project is devoted to the properties of free metal clusters (unperturbed by strong interactions with a substrate). We are interested in the size evolution of cluster spectra and make full use of the current technological possibilities to study mass-selected clusters (i.e., mass-spectrometric tools).

The project has several directions: design of a novel positron-spectroscopy setup at the LLNL LINAC in order to study positron-cluster collision processes, a related study of charge-exchange processes in cluster collisions at the U.C. Berkeley cluster laboratory, and theoretical work on understanding various cluster properties. In the following, we summarize progress along these lines.

Positron Experiment

At present, the following has been accomplished. The design of vacuum chambers for the cluster beam has been finished; the chambers are being manufactured by MDC Vacuum Products. Similarly, the design of a translation stage for the cluster source has been finished, and the stage is being built by Huntington Vacuum Products. The rest of cluster source design is in progress.

Mass spectrometer design is also in progress, accompanied by consultations with the prospective manufacturer, Comstock Inc., and by numeric ion- and positron-trajectory analysis with the aid of the SIMION software package.

Installation of the positron transfer line is under way and will be finished in the near future.

Collision Studies

Over the past few months, a detailed experiment has been completed in Berkeley devoted to a mass-sensitive study of collisions between neutral alkali clusters and a variety of gas targets. Data analysis is in progress. This experiment is the first investigation of collision processes for such a range of cluster masses; it provides information

of stabilities, interactions, electron-transfer processes, and primordial chemisorption of clusters. In view of the sensitivity to collision and electron-transfer channels, this experiment is closely related to the positron-impact project described above and provides much background information.

Theoretical Work

We have written a series of papers (see below) concerning electronic and scattering processes in metal and carbon clusters. This research is closely related to the current experimental activities and provides analytic theoretical results in close agreement with the experimental data, as well as guidance for future research.

Presentations

April/May 1992: Talk, Materials Research Society Symposium, San Francisco, CA.

February 1992: Invited Seminar, Department of Physics, University of California, Los Angeles, VA.

January 1992: Seminar, Physics Department, Lawrence Livermore National Laboratory.

November 1991: Seminar on Nuclear Physics Concepts in Atomic Cluster Physics, Bad Honnef, Germany (Invited talk).

Publications

1. V. Kresin, "Collective Resonances and Photoabsorption in Metal Clusters," *Phys. Reports* (in press).
2. V. Kresin, "Analysis of Collective Resonances in Clusters: Metals and Carbon," submitted to *MRS Symp. Proc.*, April 1992.
3. V. Kresin and E. Kipparini, "Photodisintegration Sum Rule and Electron Distribution in Metal Clusters," submitted to *Phys. Rev. B* (March 1992).
4. V. Kresin, "Electron Distribution and Collective Resonances in Nonspherical Metal Clusters," *Phys. Rev. B* (in press).
5. V. Kresin, "Electron Scattering and Electromagnetic Response Properties of Metal Clusters," *Proc. Seminar on Nuclear Physics Concepts in Atomic Cluster Physics*, Bad Honnef, Germany, November 1991 (Springer Lectures in Physics, to be published).

Nanoscale Lithography Induced Chemically or Physically by Modified Scanned Probe Microscopy

M. Balooch and W. J. Siekhaus

Overview

This research investigates the chemical reactivity induced by phenomena occurring between the tip and the substrate in a scanning tunneling microscope and physical modification of the substrate by the tip of an atomic-force microscope. The ultimate goal is to generate nanoscale patterns, such as narrow trenches and ultrathin oxide masks to be used in the electronics industry. The STM is an attractive instrument for nanoscale lithography because its low-voltage, high-, and localized electric-field characteristics can result in minimal damage to nearby structures and to the substrate. Moreover, it is a compact and flexible processing tool, capable of operating over a wide range of environmental conditions. In this project, a variety of electronic substrates such as silicon, SiO_2, and SiC will be examined.

Progress

To study the etching and deposition processes occurring between the tip and the substrate in a proper environment, we have designed and constructed a reaction chamber capable of handling various gases of interest to accommodate our existing STM and AFM and have used it to study the STM-induced oxidation of silicon substrates.

We use an elaborate technique to remove the native oxide and to terminate the silicon surface atoms with hydrogen atoms. The procedure starts with a 15-min inert-gas anneal at about 1050°C. After a 7:1 buffered HF acid removal of the thermal oxide, the silicon samples are reoxidized using a 5:1:1 solution of H_2O:HCl: H_2O_2 at 80°C for 10 min. The samples are then placed into 10% HF and 40% NH_4F solutions for 4 to 6 min for oxide removal and H-atom passivation of the silicon dangling bonds. This method prevents oxidation of a silicon surface in air for at least 1 hr.

Patterns of thin oxide with nanoscale dimensions have been grown on silicon as prepared above by an STM-enhanced oxidation process. Figure 1 shows the sequence of oxide-writing "LLL" 1.5 nm high and 0.2 μm wide on a Si(100) surface. Recently, the technique has been improved to generate patterns 20 nm wide.

To study details of STM-induced reactivity, we use a technique in which voltage pulses varied in duration and frequency are applied between the tip and the substrate. Figure 2 shows the apparent height change of the surface right below the center of the tip as a function of applied pulse duration. At short pulse durations, depression is observed, presumably due to removal of hydrogen from the surface. At higher duration, however,

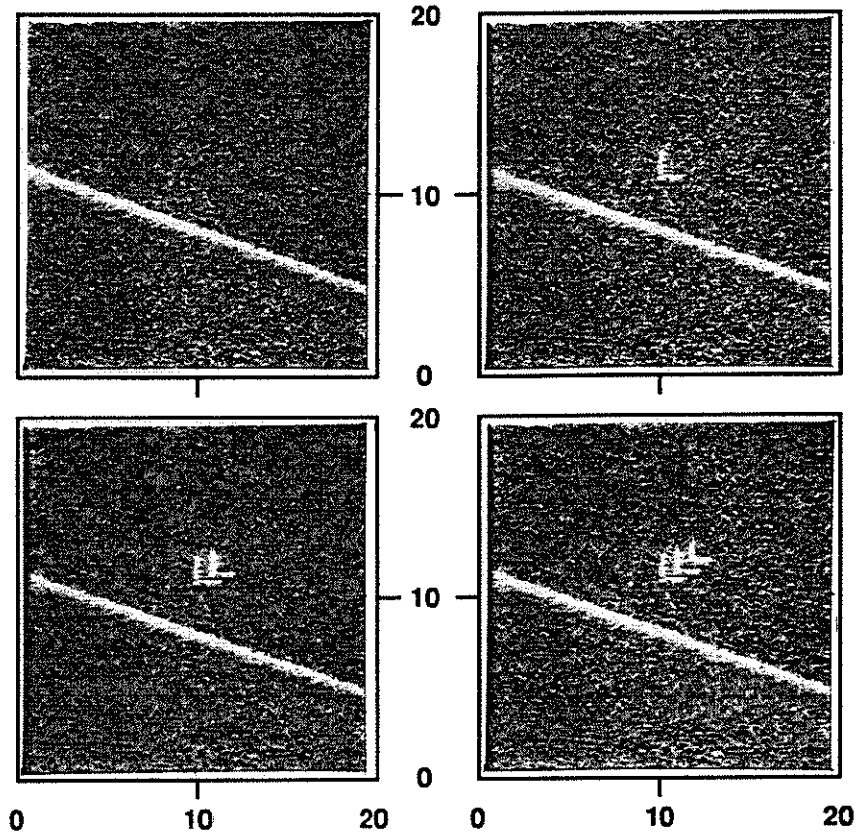

Figure 1. Oxide pattern formation on clean silicon using STM-induced reaction.

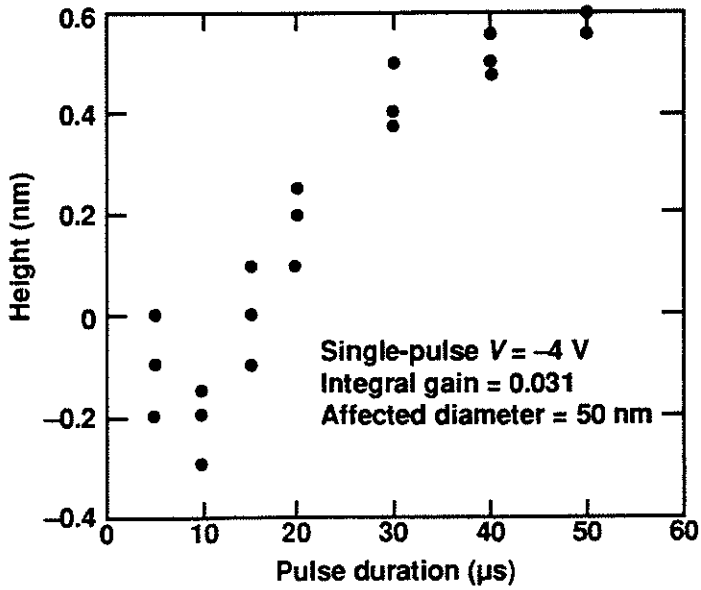

Figure 2. Oxide growth on clean silicon as a function of pulse duration applied to STM tip in an oxygen atmosphere.

growth of oxide is apparent. The effects of field strength and polarity and oxygen partial pressure on oxide growth have also been investigated in detail.

We are now seeking a kinetic model based on experimental observations to explain the STM-enhanced oxidation of silicon. The results will be submitted for publication.

Milestones—STM

Si-XeF_2

- The reaction chamber will be modified for silicon etching by XeF_2. A cryopump will be added to the system, and a doser will be installed for XeF_2 gas delivery to the silicon surface under the STM tip (by June 1992).
- Nanoscale etching of silicon by the STM tip in XeF_2 reactant gas will be demonstrated (by August 1992).
- The detailed kinetics of STM-induced etching will be studied by applying voltage pulses to the tip. The effect of polarity and intensity of the field between tip and substrate, and the effect of the tunneling current density will be investigated to find optimum conditions for enhanced etching (by September 1992).
- A model for STM-induced etching will be proposed (by November 1992).

SiC

- A suitable method of surface cleaning will be adopted (December 1992).
- A reactant gas will be used to gasify both carbon and silicon at comparable rates. In contrast to silicon etching, XeF_2 may not be a proper reactant for SiC since fluorine does not gasify carbon appreciably. However, a compound such as F_2O_2 appears to have a better chance of gasifying both carbon and silicon (March 1993).
- The detailed kinetics of STM-induced etching by XeF_2 or F_2O_2 using the voltage-pulse technique will be studied (April 1993).

Milestones—AFM

- An extra conductive tip will be grown on the side of a conventional dielectric AFM tip, but with shorter length so that it does not contact the surface. The conductive tip will be used for surface modification of thin, nonconductive films using the voltage-pulsing method described above. The conventional tip will then be used for imaging. The instrument will be used to etch through the oxide film on silicon surfaces (by September 1993).
- The dynamics of field-induced modification of dielectric films on conductors and semiconductors will be investigated (by September 1993).